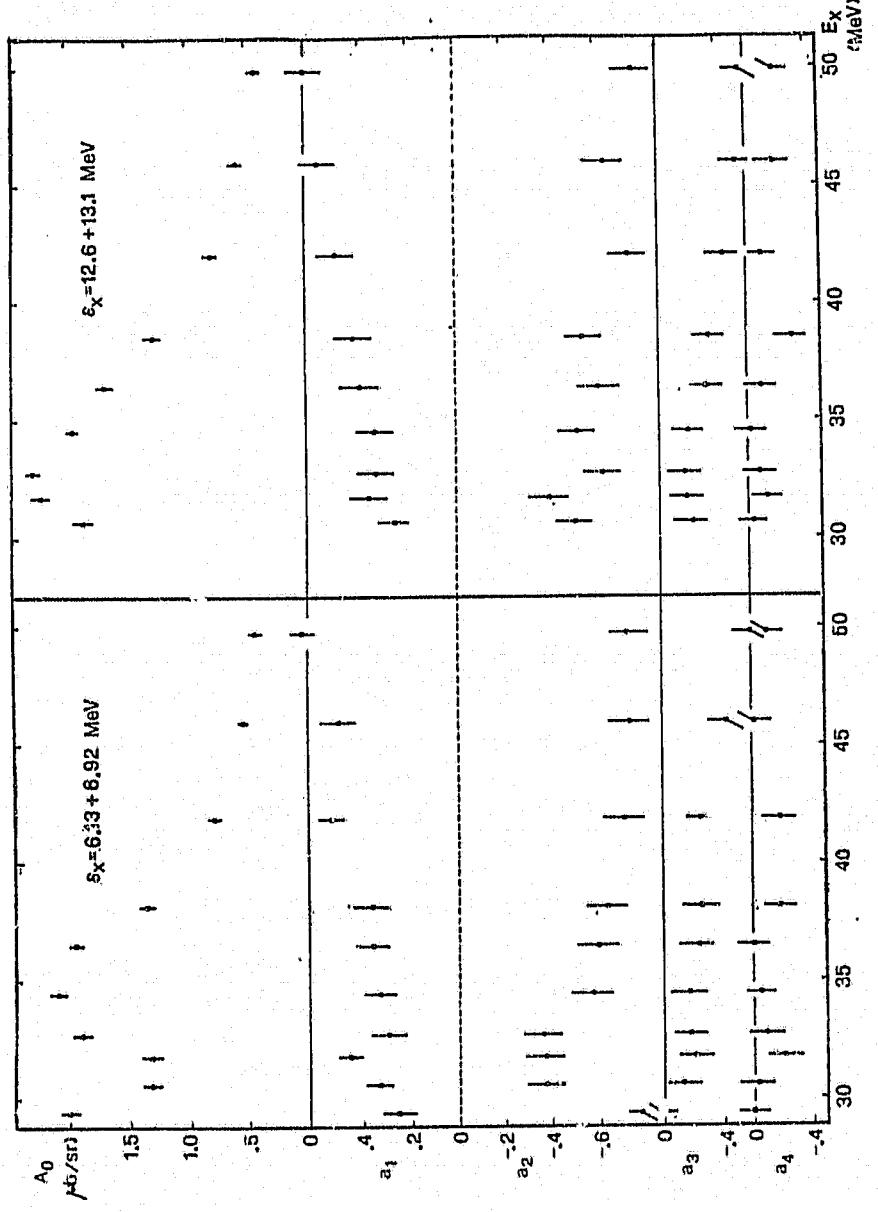

FIGURE 22 Angular distribution coefficients for proton radiative capture transitions to ^{16}O final states at $E_x = 6.13 + 6.92$ MeV and $E_x = 12.6 + 13.1$ MeV.

of the a_k coefficients. Differently from what is observed in ^{12}C and ^{13}N, the resonances centroid energies are all in the 32 – 35 MeV region, but only small variations can be expected by the inclusion of missing low energy points in the [1-46] integral. Thus one has to reconsider for oxygen the simple weak coupling assumption concerning 1p-1h dipole excitations and the final nucleus excited states. No theoretical calculation is presently available.

1-13 Radiative capture to heavier nuclei and excited levels spectroscopy

Radiative proton capture to odd-odd nuclei and to nuclei heavier than oxygen has been limited by the relatively low Q values that required high energy beams to explore the region on and above the GDR, and the relatively high level density that prevented, in the absence of very good resolution gamma spectrometers, the disentangling of the many radiative transitions involved in a complete photon spectrum. A comparison of the g.s. GDR's [142] as obtained from (p,γ) experiments shows large differences in the character of such resonances going from the smooth curves of ^{4}He and ^{8}Be to the many strong structures observed in ^{28}Si and ^{32}P to again a simple behaviour for ^{40}Ca. If individual structures superimposed to the main GDR wide peak, have been recognised for light nuclei as isolated structures or as many particle-many hole excitations interfering with the basic dipole oscillation, ^{24}Mg, ^{28}Si and ^{32}S present a complex situation which cannot be clarified by shell model calculations. As an example of such a complexity we can take the results obtained by Singh et al. [143] in ^{28}Si in the range $4\,MeV < E_p < 12.5\,MeV$ for transitions to the g.s., the 1.77 MeV 2^+ first excited state and to the unresolved doublet $4.61(4^+) - 4.97(0^+)$ MeV seen via the $^{27}Al(p,\gamma_x)^{28}Si$. The 90 deg yield curve was measured with an energy definition of 15 keV and a large set of five point angular distributions was obtained for the two main transitions. The γ_0 yield exhibits an average resonant shape centered at $E_x \approx 19.6\,MeV$ with a width of about 4.5 MeV, with superimposed a large number of secondary maxima better defined in comparison to previous work [31], because of the small energy steps adopted. The integrated (p,γ_0) cross section result is 200 eV b. A similar trend is shown by the γ_1 yield curve which is also $\approx 5\,MeV$ wide but centered at $E_x = 20.8\,MeV$, a value approximately corresponding

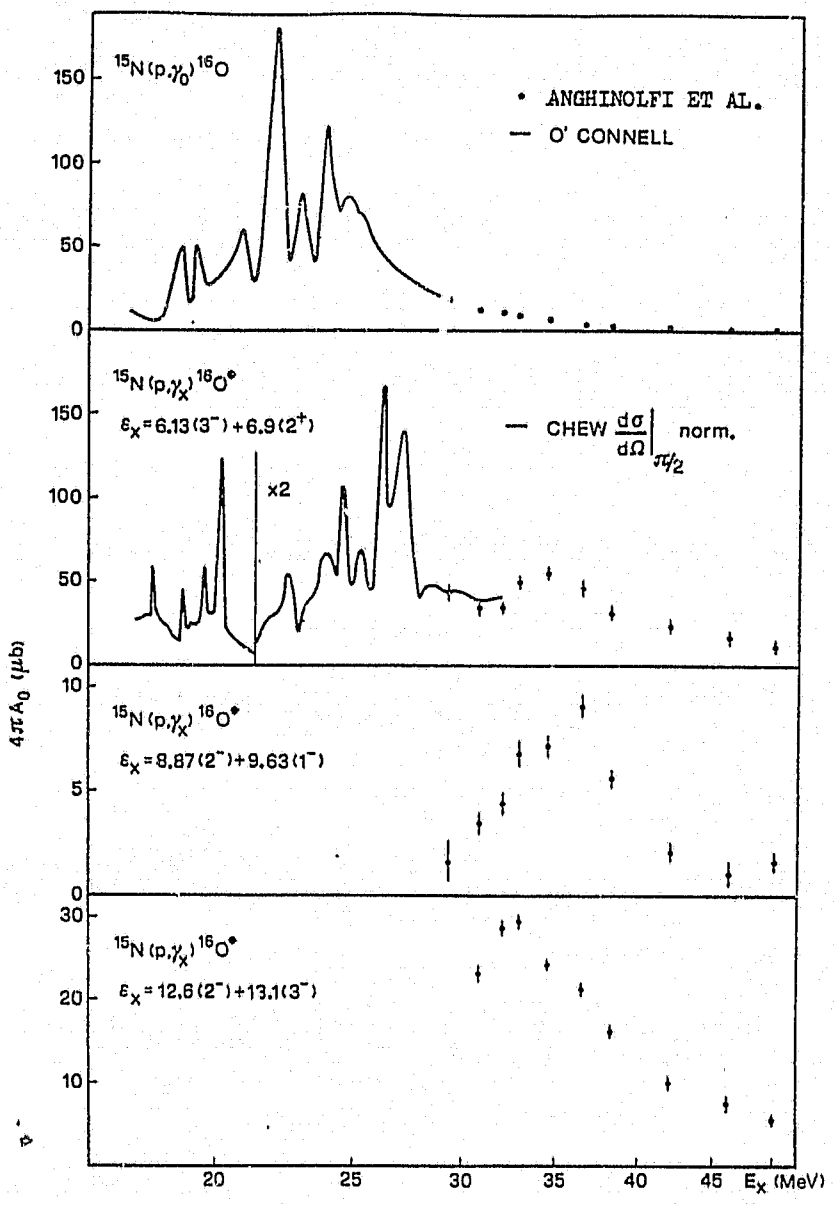

FIGURE 23 Total cross section for different final states in ^{16}O as a function of excitation energy. Resonances are seen in every reaction channel.

to $(E_x(\text{g.s.}) + 1.77)$MeV, as if the two excitations were weakly coupled. The integrated (p,γ_1) cross section is 410 eVb. Gross structures in the γ_{2+3} yield curve are not seen due to the limited energy range, but a steady increase is observed up to $E_p = 12.5$ MeV which indicates, as subsequently confirmed [144],the build up of a GDR based upon these states too. The angular distributions give conclusive information about the nature of the observed resonances. The γ_0 distributions are usually isotropic within 20% with the 90 deg point changing from being the maximum at the lowest energies to being the minimum at the highest E_p. The γ_1 distributions are usually peaked nearly at 90 deg and their anisotropy increases with energy. The usual [1-4] expansion limited to $n = 4$ has been applied to these data. In the γ_0 channel a_3 and a_4 are basically consistent with zero and a_2 averages at about +0.10 on the left side of the GDR to decrease to about -0.20 above it, but showing only small fluctuations absolutely not correlated to the large fluctuations observed in the A_0 coefficient. The a_1 averages at $\approx +0.07$ in all of the energy regions investigated. Since a_2 is the only sizeable coefficient one is led to conclude that we are in the presence of a dominant E1 transition mode responsible for the large structures observed, with superimposed a set of secondary peaks generated by the interference with more complex configurations of the compound nucleus, but not so strong as to influence the behaviour of the angular distributions. For the γ_1 transition again a_4 is basically zero, but a_3 averages at ≈ -0.10 and a_2 averages at -0.5 all over with oscillations larger than those observed for the γ_0 case but again not correlated with the structures observed in A_0. The a_1 is positive and averages at $\approx +0.10$. From this picture it is speculated that E1 dominates the γ_1 transition, that more complex configurations are responsible for the secondary maxima through their interference with E1 and that some E2 strength is present in this channel as indicated by a sizeable a_3 coefficient. The γ_{2+3} angular distributions are almost isotropic. The near constancy of the angular distributions suggests a well defined state for the GDR. Considering only E1 transitions these can occur to the ground state of ^{28}Si only from 1^- compound states, while E1 transitions to the 2^+ 1.77 MeV first excited state can occur from 1^-, 2^-, 3^- compound nucleus resonances. These can be formed by protons in the entrance channel configuration $f_{\frac{7}{2}}$, $f_{\frac{5}{2}}$ or $p_{\frac{3}{2}}$ which in pure $j-j$ coupling will combine with the $J^\pi = \frac{5}{2}^+$ of the ^{27}Al g.s. to form a 1^- compound state, or by protons

in the entrance channel configuration $f_{\frac{7}{2}}$, $f_{\frac{5}{2}}$, $p_{\frac{3}{2}}$ or $p_{\frac{1}{2}}$ to form a 2^-, 3^- compound state. Realistically a mixture of all possible configurations is to be expected. For γ_0 transitions $f_{\frac{5}{2}} \rightarrow d_{\frac{5}{2}}$(E1) can be assumed small since it would involve spin flip. No distinction between a dominant $p_{\frac{3}{2}}$ or $f_{\frac{7}{2}}$ proton configuration can be made on the grounds of the a_2 values only. In any case the observed a_2 coefficient (average value ≈ -0.10) is very similar to that expected for a pure $p_{\frac{3}{2}}$ configuration and quite different from that expected for a pure $f_{\frac{7}{2}}$ configuration (-0.36). For the γ_1 transition the only J^π assignment compatible with the observed a_2 average value of -0.50 is that of a 2^- for which a_2 is in the range $-0.50 < a_2 < +0.375$. But no further discrimination can be made on the entrance channel configuration for this 2^- state, since both a

$$0.42p_{\frac{1}{2}} - 0.79p_{\frac{3}{2}} - 0.17f_{\frac{5}{2}} + 0.41f_{\frac{7}{2}} \qquad (a_2 = -0.5) \qquad [1-84]$$

and a

$$0.48p_{\frac{1}{2}} + 0.26p_{\frac{3}{2}} - 0.78f_{\frac{5}{2}} - 0.32f_{\frac{7}{2}} \qquad (a_2 = -0.46) \qquad [1-85]$$

or even a linear combination of the two, fits the data.

The advent of large, good resolution NaI spectrometers has finally allowed reliable investigation of the γ transitions to highly excited states in heavy nuclei, with the results already obtained for light nuclei, on the GDR built upon excited states and the single particle character of proton radiative capture, confirmed despite the complexity of level structure. A large set of data on the $^{27}Al(p,\gamma)^{28}Si$, $^{39}K(p,\gamma)^{40}Ca$ and $^{40}Ca(p,\gamma)^{41}Sc$ has been reported by Dowell [144]. As many as 14 transitions to final states of ^{28}Si have been identified and their 90 deg cross section measured. The same has been done for 15 channels in ^{40}Ca and 9 channels in ^{41}Sc. The general trend of proton capture to produce resonances built on basically any state of the final nucleus having a large superposition with the entrance channel configuration, already presented as evidence by Anghinolfi et al. [79] for light nuclei is now strongly confirmed. All 14 ^{27}Al transitions show resonances peaking at an energy just ≈ 19 MeV above the excited state energy, and a few MeV wide. The same is found, with no exception, in all ^{40}Ca and ^{41}Sc transitions, indicating a weak coupling between the dipole excitation and the single excited states. Angular distributions

are not measured but, extrapolating what has systematically been observed in all other nuclei, we can expect a basic E1 behaviour for these transitions with E2 strength becoming more and more relevant as the energy increases. A remarkable new insight provided by Dowell et al. [144] [145] is the observed correlation between integrated capture cross sections and the spectroscopic factors deduced from pick-up reactions. Integrated cross sections are in most instances proportional to the spectroscopic strengths and this fact finds a attractive interpretation in a simple model envisaged by Snover [146]. Referring to direct photonuclear reactions one can think first of a dipole photon absorbed by a nucleus A excited into a very simple configuration consisting of an inert $A-1$ core $|\chi_0>$ coupled to a proton in a $|n,\ell>$ single particle orbit, followed by emission of the proton in a continuum state $|\alpha>$. The transition amplitude can be written

$$S_{\alpha,n\ell} = \left[1 + \frac{\Delta E}{E_\gamma - E_{GDR} + i\Gamma/2}\right] < \chi_0;\alpha|D|\chi_0;n\ell > \qquad [1-86]$$

D being the dipole operator, the term in square brackets being as usually the direct plus semidirect factor, E_γ being the photon energy, E_{GDR} being the energy of the resonance of width Γ. ΔE is the energy difference between the unperturbed particle-hole state as described by a shell model calculation and the actual resonance energy which we know is pushed up with respect to the unperturbed value by the residual interaction. For $E_\gamma \approx E_{GDR}$ we may write the cross section as

$$\sigma^{n\ell}_{exp}(\gamma,p) = \left[\frac{\Delta E}{(E_\gamma - E_{GDR})^2 + \Gamma^2/4}\right]\sigma^{n\ell}(\gamma,p) \qquad [1-87]$$

When dealing with a physical excited state $|\psi>$, this may be represented as the superposition of a set of single particle-single hole states of the kind just mentioned, through the spectroscopic factors $S_{n\ell}$ described as the probability that the actual nuclear level looks like an A-1 core plus a nucleon in the orbital $|n\ell>$, i.e.

$$S_{n\ell} = |<\psi|\chi_0;n\ell>|^2 \qquad [1-88]$$

Taking into account the Clebsch Gordan coefficient for the coupling of proton and target nucleus isospins, the experimental cross section for the emission of a proton from a

nuclear level $|\psi>$ at a GDR resonance energy E_{GDR} is

$$\sigma_{exp}(\gamma,p) = \frac{\Delta E^2}{(E_\gamma - E_{GDR})^2 + \Gamma^2/4} \sum_{n\ell} C^2S(n\ell)\sigma^{n\ell}(\gamma,p) \qquad [1-89]$$

Integrating over energy gives

$$\int \sigma_{exp} dE_\gamma = \sum_{n\ell} C^2S(n\ell) \int \frac{\Delta E^2}{(E_\gamma - E_{GDR})^2 + \Gamma^2/4} \sigma^{n\ell}(\gamma,p) dE_\gamma = \sum_{n\ell} C^2S(n\ell) K_{n\ell} \qquad [1-90]$$

where $K_{n\ell}$ is the energy integral of the giant resonance excited upon the state $|n\ell>$. $K_{n\ell}$ can be calculated in a schematic way [146] by summing up all E1 transitions between the 1p-1h excited state $|n\ell>$ and the states j_2 which make up the GDR and integrating over the resonance.

$$K_{n\ell} = \int_{GDR} \sum_{j_2} |<j_2|D|n\ell>|^2 \qquad [1-91]$$

with $j_1 - 1 \leq j_2 \leq j_1 + 1$ and $j_1 = \ell \pm \frac{1}{2}$. For a single dipole transition $<2|D|1>$ at energy E_{12} the integrated cross section is given [147] by:

$$\int_{line} \sigma(E) dE = \frac{4\pi^2 E_{12}}{\hbar c} D_{12}^2 \qquad [1-92]$$

and for the transitions involved in the GDR built upon $|n\ell>$

$$\int_{GDR} \sigma(E) dE = \frac{4\pi^2}{\hbar c} \sum_{j_2} E_{12} D_{j_2}^2 = \frac{4\pi^2}{\hbar c} \sum_{j_2} E_{12} |<j_2|D|j_1>|^2 \qquad [1-93]$$

Introducing an explicit form for D one has

$$\int_{GDR} \sigma(E) dE = \frac{4\pi^2}{\hbar c} \sum_{j_2} E_{12}\, q^2 \left| \int \psi_2^*(j_2) z \psi_1(j_1) \right|^2 \qquad [1-94]$$

which becomes, writing $z = \sqrt{4\pi/3}\, r Y_{10}$, introducing the effective charge $q = e\frac{N}{A}$ and averaging over the initial m_1 values and summing over the final m_2 values (since neither m_1 nor m_2 is measured)

$$= \frac{4\pi^2}{\hbar c}\frac{4}{3}\pi e^2(N/A)^2 \sum_{j_2} E_{12}\frac{1}{2j_1+1}\sum_{m_1 m_2} |< j_2 m_2|Y_{10}|j_1 m_1 >|^2 \left|\int dr r^3 R_1 R_2\right|^2$$

$$= \frac{(4\pi)^2}{3}\pi(N/A)^2\frac{e^2}{\hbar c}\sum_{j_2} E_{12}\frac{|< r >^2}{2j_1+1}\sum_{m_1 m_2}(j_1 m_1 10|j_2 m2)|< j_2||Y_{10}||j_1 >|^2$$

$$= \frac{(4\pi)^2}{3}\pi(N/A)^2\frac{e^2}{\hbar c}\sum_{j_2} E_{12}\frac{< r >^2}{2j_1+1}(2j_1+1)|< j_2||Y_{10}||j_1 >|^2$$

$$= \frac{(4\pi)^2}{3}\pi(N/A)^2\frac{e^2}{\hbar c}\sum_{j_2} E_{12} < r >^2 (2j_1+1)(j_1\tfrac{1}{2}10|j_2\tfrac{1}{2})^2\frac{3}{4\pi}$$

$$= \frac{4\pi^2}{3}(N/A)^2\frac{e^2}{\hbar c}\sum_{j_2} < r >^2 (2j_1+1)(j_1\tfrac{1}{2}10|j_2\tfrac{1}{2})^2 \qquad [1-95]$$

where we have made use of the identity [148]

$$|< j_2||Y_{10}||j_1 >|^2 = (2j_1+1)(j_1\tfrac{1}{2}10|j_2\tfrac{1}{2})^2\frac{3}{4\pi} \qquad [1-96]$$

In our case the shell $|n\ell >$ is not full, but only contains $n = 1$ nucleon, so expression [1-95] must be weighted by the ratio of n to the maximum possible number of nucleons in that shell $2j_1 + 1$. The total integral becomes

$$\int_{GDR}\sigma(E)dE = \frac{4\pi^2}{3}(N/A)^2\frac{e^2}{\hbar c}\sum_{j_2} E_{12} < r >^2 (j_1\tfrac{1}{2}10|j_2\tfrac{1}{2})^2 \qquad [1-97]$$

The quantity $< r >^2$ can be computed from the simple harmonic oscillator radial wave functions and according to which transition is involved, takes the form [147] $\frac{\hbar}{M\omega}\times\beta$ where β is a transition dependent numerical coefficient, M is the nucleon mass and $\hbar\omega$ is the transition energy. From the harmonic oscillator calculations one has

$$\sum_{j_2} < r >^2 (j_1\tfrac{1}{2}10|j_2\tfrac{1}{2})^2 = \frac{\hbar}{M\omega}(n+\frac{\ell}{2}+\frac{1}{2}) \qquad [1-98]$$

and consequently putting $E_{12} = \hbar\omega$ for any of the transitions involved one has finally a simple expression linking the integrated GDR cross section to an excited state to the spectroscopic factors for that state

$$= \frac{4\pi^2}{\hbar c}\frac{4}{3}\pi e^2 (N/A)^2 \sum_{j_2} E_{12}\frac{1}{2j_1+1}\sum_{m_1 m_2} |< j_2 m_2|Y_{10}|j_1 m_1 >|^2 \Big| \int dr r^3 R_1 R_2\Big|^2$$

$$= \frac{(4\pi)^2}{3}\pi (N/A)^2 \frac{e^2}{\hbar c}\sum_{j_2} E_{12}\frac{< r >^2}{2j_1+1}\sum_{m_1 m_2}(j_1 m_1 10|j_2 m2)|< j_2||Y_{10}||j_1 >|^2$$

$$= \frac{(4\pi)^2}{3}\pi (N/A)^2 \frac{e^2}{\hbar c}\sum_{j_2} E_{12}\frac{< r >^2}{2j_1+1}(2j_1+1)|< j_2||Y_{10}||j_1 >|^2$$

$$= \frac{(4\pi)^2}{3}\pi (N/A)^2 \frac{e^2}{\hbar c}\sum_{j_2} E_{12} < r >^2 (2j_1+1)(j_1\frac{1}{2}10|j_2\frac{1}{2})^2\frac{3}{4\pi}$$

$$= \frac{4\pi^2}{3}(N/A)^2 \frac{e^2}{\hbar c}\sum_{j_2} < r >^2 (2j_1+1)(j_1\frac{1}{2}10|j_2\frac{1}{2})^2 \qquad [1-95]$$

where we have made use of the identity [148]

$$|< j_2||Y_{10}||j_1 >|^2 = (2j_1+1)(j_1\frac{1}{2}10|j_2\frac{1}{2})^2\frac{3}{4\pi} \qquad [1-96]$$

In our case the shell $|n\ell >$ is not full, but only contains $n = 1$ nucleon, so expression [1-95] must be weighted by the ratio of n to the maximum possible number of nucleons in that shell $2j_1 + 1$. The total integral becomes

$$\int_{GDR}\sigma(E)dE = \frac{4\pi^2}{3}(N/A)^2\frac{e^2}{\hbar c}\sum_{j_2} E_{12} < r >^2 (j_1\frac{1}{2}10|j_2\frac{1}{2})^2 \qquad [1-97]$$

The quantity $< r >^2$ can be computed from the simple harmonic oscillator radial wave functions and according to which transition is involved, takes the form [147] $\frac{\hbar}{M\omega}\times\beta$ where β is a transition dependent numerical coefficient, M is the nucleon mass and $\hbar\omega$ is the transition energy. From the harmonic oscillator calculations one has

$$\sum_{j_2} < r >^2 (j_1\frac{1}{2}10|j_2\frac{1}{2})^2 = \frac{\hbar}{M\omega}(n+\frac{\ell}{2}+\frac{1}{2}) \qquad [1-98]$$

and consequently putting $E_{12} = \hbar\omega$ for any of the transitions involved one has finally a simple expression linking the integrated GDR cross section to an excited state to the spectroscopic factors for that state

$$\int_{GDR} \sigma_{exp}(\gamma,p)dE_\gamma = \frac{4\pi^2}{3}\frac{e^2\hbar}{Mc}(N/A)^2C^2\sum_{n\ell} S(n\ell)(n+\frac{\ell}{2}+\frac{1}{2}) \qquad [1-99]$$
$$= \sum_{n\ell} C^2S(n\ell)K_{n\ell}$$

with

$$K_{n\ell} = 9.87(n+\frac{\ell}{2}+\frac{1}{2})\,\text{MeV mb} \qquad [1-100]$$

Now the cross sections of two reactions the exact inverse of one another are related through detailed balance ($\sigma_1 g_1 p_1^2 = \sigma_2 g_2 p_2^2$) which is valid for unpolarized beams and targets, where σ_1 and σ_2 are the cross sections, g_1 and g_2 are the statistical weights associated with the two interacting particles (in the specific case of (γ,p) and (p,γ) $2J+1$ for the nucleus and 2 for the possible photon polarizations) and p_1 and p_2 are the momenta of relative motion. In other words

$$(2J+1)\frac{d\sigma}{d\Omega}(\gamma,p) = (2I_{A+1}+1)[A/A+1]^2 2Mc^2\frac{E_p}{E_\gamma^2}\frac{d\sigma}{d\Omega}(p,\gamma) \qquad [1-101]$$

where J is the spin of the final state in the $A+1$ nucleus and M the nucleon mass. Dowell assumes $W(\vartheta) = (1+a_2P_2)$ which gives a total cross section

$$\sigma(p,\gamma) = 4\pi/(1-\frac{a_2}{2})\frac{d\sigma}{d\Omega}(p,\gamma)\big|_{\vartheta=90} \qquad [1-102]$$

and therefore a strong correlation between the integrated experimental data and the available experimental spectroscopic factors, namely

$$\frac{4\pi}{(1-a_2/2)}(2J+1)\int \frac{d\sigma}{d\Omega}\big|_{90}(\gamma,p)dE_\gamma = \sum_{n\ell}(2J+1)K_{n\ell}C^2S(n\ell) \qquad [1-103]$$

The comparison between the two quantities in equation [1-103] using the $K_{n\ell}$ of the schematic model, always gives very close results in all nuclei investigated and clearly shows the preference for (p,γ) reactions to populate single particle states as already remarked [78] for light nuclei. The accuracy with which $K_{n\ell}$ values can be computed even from simple models, offers the prospect of using radiative capture reactions as a valuable spectroscopic tool even for states at high excitation energy to complement the information obtained in pick-up reactions, at least for those cases where the sum over $n\ell$ is largely dominated by a single $n\ell$ couple.

REFERENCES FOR CHAPTER 1

1) M.M.Giannini and G.Ricco
Riv. Nuovo Cim. 4(1985)1

2) J.L.Mattews, T.Kruse, M.Williams, R.O.Owens and W.Savin
Nucl. Phys. A223(1974)221

3) R.A.Brandenburg, Y.E.Kim and A.Tubis
*Phys. Lett.*B49(1974)205

4) M.R.Stranger and P.V.Sauer
Nucl. Phys. A231(1974)1

5) S.Aufleger and D.Drechsel
Nucl. Phys. A364(1981)81

6) M.Verde
Handbuch der Phys. Bd39(1957)

7) V.N.Fetisov, A.N.Gorbunov and T.Vartolomev
Nucl. Phys. 712(1965)305

8) G.M.Griffith, E.A.Larson and L.P.Robertson
Can. J. Phys. 40(1962)402

9) W.Wolfli, R.Bosch, J.Lang, R.Muller and P.Marmier
*Phys. Lett.*22(1966)75

10) D.B.Belt, C.R.Bingham, M.L.Halbert and A.Van der Woude
Phys. Rev. Lett. 24(1970)1120

11) J.P.Didelez, H.Langevin-Joliot, Z.Maric and V.Radojevic
Nucl. Phys. A143(1970)602

12) B.F.Gibson and J.S.O'Connell
Bull. Am. Phys. Soc. 15(1970)480

13) S.E.King, N.R.Roberson, H.R.Weller and D.R.Tilley
Phys. Rev. C30(1984)21

14) S.King, N.R.Roberson, H.R.Weller, D.R.Tilley, H.P.Engelbert, H.Berg, E.Huttel and G.Clausnitzer
Phys. Rev. C30(1984)1335

15) B.F.Gibson and D.R.Lehman
Bull. Am. Phys. Soc. 27(1982)569

16) P.Guss
Duke University (unpublished)

17) M.Anghinolfi, P.Corvisiero, M.Guarnone, G.Ricco and A.Zucchiatti
Nucl. Phys. A410(1983)173

18) I.N.Barbour and J.A.Hendry
*Phys. Lett.*38B(1972)151

19) S.E.King, N.R.Roberson, H.R.Weller and D.R.Tilley
Phys. Rev. Lett. 51(1983)877

20) D.M.Skopik, J.Asai, D.H.Beck, T.P.Dielschneider, R.E.Pywell and G.A.Retzlaff
Phys. Rev. C28(1983)52

21) J.M.Cameron, P.Kitching, W.J.McDonald, J.Pasos, J.Soukup, J.Tekkumthala, H.S.Wilson, R.Abegg, D.A.Hutcheon, C.A.Miller, A.W.Stetz and I.J.VanHeerden
Nucl. Phys. A424(1984)549

22) J.L.Faure
Nucl. Phys. A358(1981)321

23) F.Prats
*Phys. Lett.*88B(1979)23

24) H.W.Fearing
*Proc. of the IX Int. Conf. on High En. Phys. (Versailles*1981)

25) J.M.Laget
Nucl. Phys. A312(1978)265

26) J.E.Perry and S.J.Bame jr.
Phys. Rev. 99(1955)1368

27) J.C.Gunn and J.Irving
Phil. Mag. 42(1951)1353

28) C.C.Gardner and J.D.Anderson
Phys. Rev. 125(1961)626

29) D.S.Gemmel and G.A.Jones

Nucl. Phys. 33(1962)102

30) W.E.Meyerhoff, M.Suffert and W.Feldman
Nucl. Phys. A148(1970)211

31) P.Mundhenke, R.Kosiek and G.Kraft
Z. Phys. 216(1968)232

32) P.P.Szydlik
Phys. Rev. C1(1970)146

33) L.Crone and C.Werntz
Nucl. Phys. A134(1969)161

34) J.P.Didelez, H.Langevin-Joliot, N.Bejedic and Z.Maric
Il Nuovo Cim.

35) J.Calarco, S.S.Hanna, C.C.Cheng, E.M.Diener, E.Kuhlmann, and G.A.Fisher
Phys. Rev. C28(1983)483

36) G.King
Stanford Univ. unpublished

37) R.C.McBroom, H.R.Weller, S.Manglos, N.R.Roberson, S.A.Wender, D.R.Tilley, D.M.Skopik, L.G.Arnold and R.G.Seyler
Phys. Rev. Lett. 45(1980)243

38) H.R.Weller and N.R.Roberson
Rev. Mod. Phys. 52(1980)699

39) D.Halderson and R.J.Philpott
Phys. Rev. Lett. 42(1979)36

40) R.W.Zurmhule, W.E.Stephens and H.H.Staub
Phys. Rev. 132(1963)751

41) W.E.Meyerhoff and W.Feldman
Nucl. Phys. A131(1969)489

42) J.M.Poutissou and W.Del Bianco
Nucl. Phys. A199(1973)517

43) H.R.Weller, P.Colby, J.Langenbrunner, Z.D.Huany, D.R.Tilley, F.D.Santos, A.Arriaga and A.M.Eiro

Phys. Rev. 132(1963)751

44) H.R.Weller, P.Colby, N.R.Roberson and D.R.Tilley
Phys. Rev. Lett. 53(1984)1325

45) S.Mellema, T.R.Wang and W.Haeberli
*Phys. Lett.*136B(1986)282

46) H.R.Weller
Proc. of the Workshop on "Few Body Systems" (Rome 1986)

47) R.Schiavilla, V.R.Pandharipande and R.B.Wiringa
Nucl. Phys. A449(1986)219

48) D.S.Gemmel, A.H.Morton and E.W.Titterton
Nucl. Phys. 10(1959)33

49) J.K.Bair, J.D.Kington and H.B.Willard
Phys. Rev. 83(1951)370

50) R.R.Perry, B.Mainsbridge and J.Rickards
Nucl. Phys. 45(1963)586

51) I.V.Mitchell and R.B.Taylor
Nucl. Phys. 44(1963)664

52) N.W.Reay, N.M.Hintz and L.L.Lee
Nucl. Phys. 44(1963)338

53) G.A.Fisher, P.Paul, F.Riess and S.S.Hanna
Phys. Rev. C14(1976)28

54) H.R.Weller and N.R.Roberson
IEEE Trans. Nucl. Sci. NS28(1981)1268

55) D.H.Dowell
AIP Conf. Proc. 125(1985)597

56) J.K.Bair, J.D.Kington and H.B.Willard
Phys. Rev. 100(1955)21

57) D.A.Katz
see quotation in ref. 61

58) J.P.Blaser, F.Boehm, P.Marmier and P.Scherrer

Helv. Phys. Acta 24(1951)465

59) W.C.Bethe
Washington Photonuclear Conference 1958

60) H.E.Gove, A.E.Litherland and R.Batchelor
Phys. Rev. Lett. 3(1959)177

61) H.E.Gove, A.E.Litherland and R.Batchelor
Nucl. Phys. 26(1961)480

62) S.Penner and J.E.Leiss
Phys. Rev. 114(1959)1101

63) E.D.Courant
Phys. Rev. 82(1951)703

64) G.E.Brown and M.Bolsterli
Phys. Rev. Lett. 3(1959)472

65) J.A.Becker and J.D.Fox
Nucl. Phys. 42(1963)669

66) N.Vinh-Mau and G.E.Brown
Nucl. Phys. 29(1962)89

67) N.W.Reay, N.M.Hintz and L.L.Lee
Nucl. Phys. 44(1963)338

68) V.Gillet and and N.Vinh-Mau
*Phys. Lett.*1(1962)25

69) R.G.Allas, S.S.Hanna, L.Meyer-Schutzmeister and R.E.Segel
Nucl. Phys. 58(1964)122

70) V.Gillet
CENS Thesis 1962 (unpublished)

71) C.Brassard, H.D.Shay, J.P.Coffin, W.Scholtz and D.A.Bromley
Phys. Rev. C6(1972)53

72) V.Gillet and N.Vinh-Mau
Nucl. Phys. 54(1964)321

73) M.Kanimura, K.Ikeda and A.Arima

Nucl. Phys. A95(1967)129

74) K.A.Snover, P.Paul and H.M.Kuan
Nucl. Phys. A285(1977)189

75) N.Tagikawa and A.Arima
Nucl. Phys. A168(1971)593

76) A.Goswami and R.D.Graves
*Phys. Lett.*39B(1972)499

77) A.Goswami and R.D.Graves
*Phys. Lett.*44B(1973)335

78) M.Anghinolfi, P.Corvisiero, G.Ricco, M.Taiuti and A.Zucchiatti
Nucl. Phys. A399(1983)66

79) G.Ricco
Lect. Notes in Phys. 61(1977)223

80) M.Anghinolfi, P.Corvisiero, E.Durante, M.Guarnone, M.Taiuti and A.Zucchiatti
Il Nuovo Cim. 77A(1983)277

81) M.Cavinato, M.Marangoni, P.Ottaviani and A.M.Saruis
Nucl. Phys. A373(1982)445

82) M.Gari and H.Hebach
Phys. Rep. 72(1981)1

83) S.Boffi, C.Giusti and F.D.Pacati
Nucl. Phys. A359(1981)91

84) M.M.Giannini and G.Ricco
Ann. of Phys. 1102(1976)458

85) L.L.Elton and A.Swift
Nucl. Phys. A94(1967)52

86) M.A.Kovash, S.L.Blatt, R.N.Boyd, T.R.Donoghue, H.J.Hausman and A.D.Bacher
Phys. Rev. Lett. 42(1979)700

87) T.W.Donnelly, J.D.Walecka, G.E.Walkerand and I.Sick
*Phys. Lett.*32B(1970)545

88) H.R.Weller, H.Hasan, S.Manglos, G.Mitev, N.R.Roberson, S.L.Blatt, H.J.Hausman,

R.G.Seyler, R.N.Boyd, T.R.Donoghue, M.A.Kovash, A.D.Bacher and C.C.Foster
Phys. Rev. C25(1982)2921

89) M.Lafferty and S.R.Cotanch
Nucl. Phys. A377(1982)363

90) O.Korban, J.Lowe, P.D.Greaves and W.Hnizdo
Nucl. Phys. A133(1969)255

91) R.L.Bramblett, S.C.Fultz, B.L.Berman, M.A.Kelly, J.T.Caldwell and D.C.Sutton
Report UCRL 70582(1967)

92) J.T.Londergan and L.D.Ludeking
Phys. Rev. C25(1982)1722

93) S.L.Blatt,H.J.Hausman, L.G.Arnold, R.G.Seyler, R.N.Boyd, T.R.Donoghue, P.Koncz, M.A.Kovash, A.D.Bacher and C.C.Foster
Phys. Rev. C30(1984)423

94) S.-F. Tsai and J.T.Londergan
see quotation in ref. [92]

95) T.W.Donnelly and G.E.Walker
Ann. of Phys. 60(1970)209

96) S.S.Hanna, W.Feldman, M.Suffert and A.Kurath
Phys. Rev. C25(1982)1179

97) E.G.Adelberger, R.E.Marrs, K.A. Hover and J.G.Bussoletti
Phys. Rev. C15(1977)484

98) R.J.Peterson and J.J.Hamill
Phys. Rev. C22(1980)2282

99) S.L.Blatt
AIP Conf. Proc. 125(1985)570

100) H.F.Glavish, S.S.Hanna, R.Avida, R.N.Boyd, C.C.Chang and E.Diener
Phys. Rev. Lett. 28(1972)766

101) D.Berghofer, M.D.Hasinoff, R.Helmer, S.T.Lim and D.F.Measday
Nucl. Phys. A263(1976)109

102) P.S.Fisher, D.F.Measday, F.A.Nikolaev, A.Kalmykov and A.B. Clegg

Nucl. Phys. 45(1963)113

103) M.Anghinolfi, P.Corvisiero, M.Guarnone, G.Ricco, M.Sanzone,
M.Taiuti and A.Zucchiatti
"*Perspect. in Nucl. Phys. at Interm. Ener.*" World Scient. Press 1983 pg 160

104) M.J.LeVine and P.D.Parker
Phys. Rev. 186(1969)1021

105) K.Wienhard, G.Clausnitzer and G.Ratmann
Z. Phys. 256(1972)457

106) H.O.Meyer and G.R.Plattner
Nucl. Phys. A199(1973)413

107) S.Ferroni, G.Ricco, G.A.Rottigni, M.Sanzone and G.Lo Bianco
Il Nuovo Cim. 35A(1976)15

108) M.Marangoni, P.L.Ottaviani and A.M.Saruis
*Phys. Lett.*49B(1974)253

109) S.G.Cohen, P.S.Fisher and E.K.Warburton
Phys. Rev. 125(1961)858

110) L.Cohen, A.K.Mann, B.J.Patton, K.Reibel, W.E.Stephens
and E.J.Winhold
Phys. Rev. 104(1956)108

111) N.W.Tanner, G.C.Thomas and E.D.Earle
Nucl. Phys. 52(1964)45

112) S.A.E.Johansson and B.Forkmann
Ark. Phys. 12(1957)359

113) K.N.Geller and E.G.Muirhead
Phys. Rev. Lett. 11(1963)371

114) N.A.Burgov, G.V.Danilyan, B.S.Dolbilkin, L.E.Lazareva and F.A.Nikolaev
JETP 16(1963)50

115) J.P.Elliot and B.H.Flowers
Proc. Roy. Soc. A242(1957)57

116) G.E.Brown, L.Castillejo and J.A.Evans

Nucl. Phys. 22(1961)1

117) E.D.Earle and N.W.Tanner
Nucl. Phys. A95(1967)241

118) B.Buck and A.D.Hill
Nucl. Phys. A95(1967)271

119) A.R.Barnett and N.W.Tanner
Nucl. Phys. A120(1968)342

120) A.R.Barnett
Nucl. Phys. A120(1968)342

121) A.R.Barnett and J.Lowe
Phys. Rev. Lett. 26(1971)266

122) J.L.Black, W.J.O'Connel, S.S.Hanna and G.L.Latshaw
*Phys. Lett.*25B(1967)405

123) S.S.Hanna, H.F.Glavish, E.M.Diener, J.R.Calarco, E.C.Chang and R.N.Boyd
*Phys. Lett.*40B(1972)631

124) S.S.Hanna, H.F.Glavish, R.Avida, J.R.Calarco, E.Kuhlman, and R.La Canna
Phys. Rev. Lett. 32(1974)114

125) M.B.Lewis and F.E.Bertrand
Nucl. Phys. A196(1972)337

126) S.H.Chew, J.Lowe, J.M.Nelson and A.R.Barnett
Nucl. Phys. A229(1974)241

127) E.M.Diener, J.Lowe, E.Ventura, J.R.Calarco, S.H.Chew, G.A.Fisher and S.S.Hanna
Stanford Univ. Progr. Rep. 49(1973)

128) S.H.Chew, J.Lowe, J.M.Nelson and A.R.Barnett
Nucl. Phys. A286(1974)451

129) A.Goldmann and M.Stroetzel
*Phys. Lett.*31B(1970)287

130) W.J.O'Connel and S.S.Hanna
Phys. Rev. C17(1978)892

131) R.J.Stewart, R.C.Morrison and D.E.Frederick

Phys. Kev. Lett. 23(1969)323

132) J.W.Jury, J.S.Hewill and K.G.Mc Neill
Can. J. Phys. 48(1970)1635

133) H.Feshbach, A.K.Kerman and R.H.Lemmer
Ann. Rev. of Phys. 41(1967)230

134) W.L.Wang and C.M.Shakin
Phys. Rev. C9(1974)2144

135) D.G.Mavis
Ph.D. Thesis Stanford Univ.(unpublished)

136) S.S.Hanna
Lect. Notes in Phys. 108(1979)288

137) M.Anghinolfi, P.Corvisiero, G.Ricco, M.Sanzone, M.Taiuti and A.Zucchiatti
Phys. Rev. C28(1983)1005

138) P.Corvisiero, M.Taiuti, A.Zucchiatti and M.Anghinolfi
Nucl. Instr. and Meth. 185(1981)291

139) D.J.Findlay and R.O.Owens
Nucl. Phys. A279(1977)385

140) D.L.Berman, R.Bergere and P.Carlos
Phys. Rev. C26(1982)304

141) A.M.Sandorfi, M.T.Collins, D.J.Millener,A.M.Nathan and S.F.Le Brun
Phys. Rev. Lett. 16(1981)884

142) N.W.Tanner, G.C.Thomas and E.D.Earle
Nucl. Phys. 52(1964)29

143) P.P.Singh, R.E.Segel, L.Meyer Schützmeister, S.S.Hanna and R.G.Allas
Nucl. Phys. 65(1965)577

144) D.H.Dowell
AIP Conf. Proc. 125(1985)597

145) D.H.Dowell, G.Feldman, K.A.Snover, A.M.Sandorfi and M.T.Collins
Phys. Rev. Lett. 50(1983)1191

146) K.A.Snover

Proc. Int. Symp. on High. Exc. Stat. and Nuc. Struc. (Orsay 1983)

147) E.Hayward

Scott. Univ. Summer. Sch. of Phys. Proc. 1964 pg 141

148) N.K.Glendenning

Phys. Rev. 114(1959)1297

CHAPTER 2

DESIGN OF THE HIGH ENERGY GAMMA SPECTROMETER

2-1 General Criteria for the choice of High Energy Gamma Detectors

Large Sodium-iodide crystals, in association with an anticoincidence plastic scintillator shell have become the standard detection system whenever γ-ray spectroscopy has to be performed with high efficiency, large solid angle, good energy resolution and convenient cost [1] to [6]. The technology of semiconductor detectors and of very high Z scintillating materials have begun to reduce, with their progress, the regular applications of NaI(Tl) in both low and high energy spectroscopy. Nevertheless the continuous improvements in the basic design of a typical sodium-iodide anticoincidence spectrometer (including the complexity of design and the crystal growing and polishing techniques)[5], have made this instrument unrivalled in medium energy γ spectroscopy, where semiconductor detectors cannot associate adequate detection volume to complement their excellent resolution, and high Z scintillators cannot provide, together with their high efficiency, a total resolution comparable to that of actual NaI(Tl) detectors. Cost is another important parameter in the choice of such a spectrometer and Sodium Iodide offers by far the lowest cost at comparable perfomances.

2-2 Monte Carlo Simulation of Shower Development in Detection Media

The ability to predict the development of the electromagnetic shower inside the detectors is of the utmost importance both for purposes of design, when all detector parameters must be optimized for best performance and simplest configuration, and in the data analysis stage, where the accurate knowledge of the response function in radiative capture is very important, since the presence of background and continuous spectra generally inhibit the experimental determination of the low energy tail associated with the total absorption peak. This effect is particularly important at photon energies above 10 MeV where energy escape due to electromagnetic radiation losses decreases the total absorption efficiency,

enhancing the tail contribution in the observed spectra. A large number of Monte Carlo calculations [7] to [15] as well as a considerable amount of measurements have been performed and give complementary information about the response function and the detection efficiency of NaI(Tl) scintillators of various sizes. At photon energies below 20 MeV reliable estimates are obtained by an accurate evaluation of ionization energy losses and geometrical effects, while radiative energy losses can be reasonably treated by introducing sharp approximations. At higher energies radiation losses become dominant and the simulation of the electron random walk in the scintillator requires a detailed description of all the involved electromagnetic processes. We developed, for cylindrical scintillators and photon energies up to the GeV region, a Monte Carlo code to simulate the history of the electron photon shower on its way through the scintillator, with particular attention dedicated to the description of the radiation losses.

Three points have been emphasized:

- Ionization energy losses and the multiple scattering effect on the electron and positron trajectories have been taken into account
- The bremsstrahlung energy losses have been included in the calculation using electromagnetic cross sections approximated in the infrared region
- Positron annihilation both in flight and at rest have been included

2-3 Outline of The Program

Standard Monte Carlo methods [16][17] are used to follow the history of a photon and the related electromagnetic shower through a radiation source and a NaI(Tl) scintillator detector. Three main parts should be highlighted in this program:

Geometrical Routines

Photons are generated randomly from a cylindrical isotropic radiation source, as well as from a parallel or divergent beam with angular distribution $P(\vartheta_\gamma)$ inside the detection solid angle $\Delta\Omega$ and with given energy spectrum $n(E_\gamma)$. Up to 8 cylindrical coaxial elements, including the source, the active scintillators and our passive (lead shields) elements, can be included in the spectrometer assembly. Self-absorption in the source is

taken into account. Geometrical routines update at any interaction, within the source or the detector volume, the position and the flight direction of photons and propagate them up to the next interaction point or to escape from the crystal edges. A cut-off energy is fixed (30 keV in all our predictions) below which photons and electrons are considered to be completely absorbed.

Photon Interaction Routines

These routines select the electromagnetic interaction and the final state parameters. The photon is converted after a pathlength X_0 in NaI(Tl) with probability

$$P(E_\gamma) = 1 - e^{-X_0 \Sigma_{tot}(E_\gamma)} \qquad [2-1]$$

where

$$\Sigma_{tot}(E_\gamma) = \Sigma_{ph}(E_\gamma) + \Sigma_C(E_\gamma) + \Sigma_{pp}(E_\gamma) \qquad [2-2]$$

is the total absorption macroscopic cross section including photoelectric effect (ph), Compton scattering (C) and pair production (pp). The relative frequency of each interaction is given by:

$$\frac{\Sigma_y(E_\gamma)}{\Sigma_{tot}(E_\gamma)} \qquad [2-3]$$

where $\Sigma_y(E_\gamma)$ is the process macroscopic cross section as computed by quantum electrodynamics [18]. The kinematic parameters, namely E_γ and angle ϑ_γ of the final products are chosen using differential cross sections $d\sigma_y/d\vartheta_y$, $d\sigma_y/dE_y$ and the generation of random numbers q_ϑ and q_E [16][17]

$$q_\vartheta = \frac{\int_0^{\vartheta_y} d\sigma/d\vartheta \, d\vartheta}{\int_0^{\pi} d\sigma_y/d\vartheta \, d\vartheta}; \qquad q_E = \frac{\int_0^{E_y} d\sigma/dE \, dE}{\int_0^{E_{max}} d\sigma_y/dE \, dE} \qquad [2-4]$$

For a two body reaction only the angular distribution $d\sigma/d\Omega$ is required, since the kinetic energy E_y and the emission angle ϑ_y are related by kinematics. If a Compton event is chosen, the photon scattering angle ϑ_γ is sampled from the Klein-Nishina cross section

$$\frac{d\sigma_C}{d\Omega} = \frac{1}{2} r_0^2 \frac{1+\cos^2\vartheta_\gamma}{[1+\alpha(1-\cos\vartheta_\gamma)]^2}\left[1+\frac{\alpha^2(1-\cos\vartheta_\gamma)^2}{(1+\cos^2\vartheta_\gamma)[1+\alpha(1-\cos\vartheta_\gamma)]}\right] \qquad [2-5]$$

where $\alpha = E_\gamma/m_0c^2$.

The energies of the scattered photon and electron as well as the electron polar emission angle ϑ_e are consequently defined . The azimuthal angles φ_γ and φ_e are opposite and uniformly chosen between 0 and 2π.

When photoelectric conversion is selected, the photon energy is completely transferred to an electron whose flight direction is isotropically chosen.

When pair production occurs, the photon energy is randomly divided between the positron and the electron and their emission polar angle $\vartheta_\pm$ is sampled from the approximated probability distribution:

$$P(\vartheta_\pm) = A\frac{\vartheta_\pm d\vartheta_\pm}{[\vartheta_\pm^2 + (1/\alpha_\pm)^2]^2} \qquad [2-6]$$

with $A = 2(\pi^2\alpha_\pm^2+1)/\pi^2\alpha_\pm^4$, and $\alpha_\pm = E_\pm/m_0c^2$. The azimuthal angles φ_+ and φ_- are opposite and uniformly selected between 0 and 2π

Electron Interaction Routines

The interactions involved favour in most cases photon-electron conversion and the final electron path has to be followed. Positive and negative electrons lose energy in their path in the scintillator by different electromagnetic processes:

i) The interaction with the atomic Coulomb field leads to the well knowr specific ionization energy loss

$$-\left.\frac{dE_\pm}{dx}\right|_{ion} = N\sum_{i=1}^{2} z_i \frac{2\pi e^4}{m_0c^2\beta^2}\left\{\ln\frac{m_0c^2\beta^2(E_\pm - m_0c^2)}{2I_i^2(1-\beta^2)} - \ln 2\,[2(1-\beta^2)^{1/2} - 1 + \beta^2]\right.$$
$$\left. + 1 - \beta^2 + \frac{1}{8}[1-(1-\beta^2)^{1/2}]^2 - \delta\right\} \qquad [2-7]$$

where $I_i = 9.1z_i(1+1.9z_i^{-2/3})$ is an average ionization energy [19][20], δ is the density effect term [19], and N is the total number of NaI(Tl) molecules per unit volume.

ii) Radiation energy losses,which become dominant in NaI(Tl) above an electron energy of 20MeV, are decribed for the i-th atom by the cross section

$$d\sigma_k|_i = 4\frac{z_i^2 r_0^2}{137}\frac{dk}{k}\left\{\left[1+(\frac{E_\pm - k}{E_\pm})^2\right]\left[\frac{\Phi_1(\gamma_i)}{4} - \frac{1}{3}\ln z_i\right] + \right.$$
$$\left. - \frac{2}{3}\frac{E_\pm - k}{E_\pm}\left[\frac{\Phi_2(\gamma_i)}{4} - \frac{1}{3}\ln z_i\right]\right\} \qquad [2-8a]$$

for $\gamma_i \lesssim 2$ and

$$d\sigma_k|_i = 4\frac{z_i^2 r_0^2}{137}\frac{dk}{k}\left[1+(\frac{E_\pm - k}{E_\pm})^2 - \frac{2}{3}\frac{E_\pm - k}{E_\pm}\right]$$
$$\left[\ln\frac{E_\pm(E_\pm - k)}{m_0c^2 k} - \frac{1}{2} - c(\gamma_i)\right] \qquad [2-8b]$$

for $\gamma_i > 2$ being $\gamma_i = [100km_0c^2]/[E_\pm(E_\pm - k)z_i^{-2/3}]$ and $\Phi_1(\gamma_i), \Phi_2(\gamma_i), c(\gamma_i)$ the screening factors [21]. Cross sections [2-8a] and [2-8b] give the emission probability of a bremsstrahlung photon in the energy interval $k \to k + dk$ by an incident electron of energy $E_\pm$. The emitted photon energy ranges from 0 to $E_\pm - m_0c^2$ with an approximated $1/k$ dependence and consequently a divergent behaviour at $k = 0$ (infrared divergency). The probability function

$$P(k, E_\pm) = \frac{\sum_{i=1}^{2}(\int_0^k d\sigma_k|_i)}{\sum_{i=1}^{2}(\int_0^{E_\pm - m_0c^2} d\sigma_k|_i)} \qquad [2-9]$$

required by the Monte Carlo technique is numerically undefined. We have therefore assumed discrete photon emission above a threshold energy E_{th} and continuous radiation energy loss at lower energies . If we define for our medium:

$$-\frac{dE_\pm}{dx}\Big|_{BS} = N\sum_{i=1}^{2}\int_0^{E_{th}} k\,d\sigma_k|_i \qquad [2-10]$$

the total continuous energy loss can be assumed as the sum of a ionization (ion) plus a soft radiation (BS) component:

$$-\frac{dE_\pm}{dx} = -\frac{dE_\pm}{dx}\Big|_{ion} - \frac{dE_\pm}{dx}\Big|_{BS} \qquad [2-11]$$

Above E_{th} the integrals in [2-9] are convergent and the random number generation can be achieved, assuming

$$\sigma_{BS}(E_{\pm})\big|_i = \int_{E_{th}}^{E_{\pm}-m_0c^2} d\sigma_k\big|_i \qquad [2-12]$$

as the total bremsstrahlung cross section for each atom. The energy dependence of the corresponding macroscopic cross section

$$\Sigma_{BS}(E_{\pm}) = N\sum_{i=1}^{2}\sigma_{BS}(E_{\pm})\Big|_i \qquad [2-13]$$

reported in figure 1 has been fitted, for $E_{th} = 300\,\text{keV}$ in NaI, by the expression

$$\begin{aligned}\Sigma_{BS} &= 0.205(E_{\pm} - 0.511) \quad , E_{\pm} < 5\,\text{MeV} \\ &= 0.091E_{\pm} + 0.44 \quad , 5 \le E_{\pm} < 10\,\text{MeV} \\ &= 0.5794\ln(E_{\pm} + 0.489) \quad , 10 \le E_{\pm} < 300\,\text{MeV}\end{aligned} \qquad [2-14]$$

in units $[cm^{-1}]$.

iii) Positrons at rest annihilate creating a photon pair of 0.511 MeV each, isotropically emitted in opposite directions . The annihilation probability is assumed to be 1 in this case. Annihilation-in-flight has also been taken into account; the two photons are emitted at angles ϑ_1 , ϑ_2 with respect to the positron direction with energy k_1 and k_2 given by

$$\vartheta_1 = \arctan\frac{\sin\vartheta_{cm}(1-\beta^2)^{1/2}}{\beta + \cos\vartheta_{cm}} \qquad [2-15a]$$

$$\vartheta_2 = \arctan\frac{\sin\vartheta_{cm}(1-\beta^2)^{1/2}}{\beta - \cos\vartheta_{cm}} \qquad [2-15b]$$

$$k_1 = \frac{E_+ + m_0c^2}{2}(1 + \beta\cos\vartheta_{cm}) \qquad [2-15c]$$

$$k_2 = \frac{E_+ + m_0c^2}{2}(1 - \beta\cos\vartheta_{cm}) \qquad [2-15d]$$

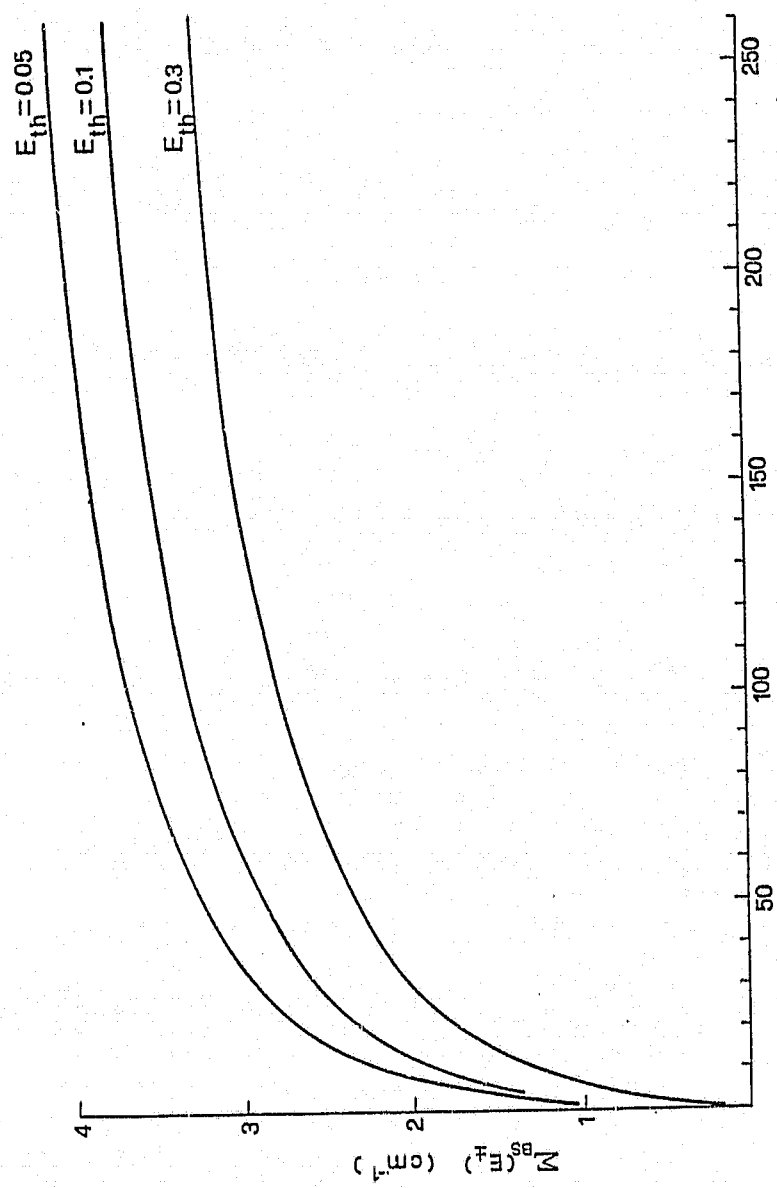

Fig. 1

FIGURE 1 Integrated macroscopic cross section for photon energies above a selected threshold E_{th}.

where ϑ_{cm} is the photon emission angle in the center of mass system (cm). Since in this system the angular distribution is isotropic, $\cos\vartheta_{cm}$ is uniformly chosen between 0 and 1. The macroscopic cross section for the annihilation in flight is [22]:

$$\Sigma_{AF} = N\pi r_0^2 \sum_{i=1}^{2} \frac{z_i}{\alpha+1}\{\frac{\alpha^2+4\alpha+1}{\alpha^2-1}\ln[\alpha+(\alpha^2-1)^{1/2}-(\alpha+3)(\alpha^2-1)^{1/2}\} \quad [2-16]$$

with $\alpha = E_\pm/m_0c^2$.

The electron path has been computed assuming, between two subsequent radiation points, linear trajectories, where the initial electron energy $E_\pm$ is slowed down by continuous (ionization + soft bremsstrahlung) losses. After a path length x the emission probability of a bremsstrahlung or annihilation photon by a negative or positive electron of energy

$$E_\pm - \int_0^x \frac{dE_\pm}{dx}dx \quad [2-17]$$

in the $x \to x+dx$ interval is given by:

$$P(x,E_\pm) = e^{-\left[\int_0^x \mu(E_\pm - \int_0^{x'} \frac{dE_\pm}{dx''}dx'')\right]}\mu(E_\pm - \int_0^x \frac{dE_\pm}{dx'}dx') \quad [2-18]$$

where obviously

$$x < R_I(E_\pm) = \int_0^{E_\pm} (\frac{dE_\pm}{dx})^{-1}dE_\pm \quad [2-19]$$

and

$$\mu(E_\pm) = \Sigma_{BS}(E_\pm) + \Sigma_{AF}(E_+) \quad [2-20]$$

Since it can be shown that:

$$\int_0^{R_I} P(x,E_\pm)dx = 1 - e^{-\left[\int_0^{R_I} \mu(E_\pm - \int_0^{x'} \frac{dE_\pm}{dx''}dx'')dx'\right]} \quad [2-21]$$

the sum of radiation and non-radiation probability results can be correctly normalized over the ionization range R_I. The path lengths can now be determined by a unique random number generation in the $0-1$ interval:

if $q_x > P(R_I, E_\pm)$

all the energy is released for continuous losses and the electron path is coincident with R_I; if $q_x \leq P(R_I, E_\pm)$
a photon is emitted by bremsstrahlung or annihilation-in-flight after a path x given by the usual Monte Carlo rule

$$q_x = \int_0^x P(xl, E_\pm)dxl \qquad [2-22]$$

Numerical values of the probabilities $P(x, E_\pm)$ at various $E_\pm$ energies are reported in figure 2 . In all cases for computing convenience, the Monte Carlo integral

$$R(x, E_\pm) = \int_0^x P(xl, E_\pm)dxl \qquad [2-23]$$

has been fitted [23] by the expression (figure 3):

$$R(x, E_\pm) = 1 - e^{-\varrho(E_\pm)x} \qquad [2-24]$$

with

$$\begin{aligned} \varrho(E_\pm) &= 0.161 \ln(E_\pm - 0.511) - 0.307 \quad E_\pm > 2.5\,\text{MeV} \\ &= 0.06(E_\pm - 0.511) \qquad E_\pm \leq 2.5\,\text{MeV} \end{aligned} \qquad [2-25]$$

(in NaI(Tl) and for $E_{th} = 300\,\text{keV}$) which leads to an analytical solution of equation [2-22] leading to a path length

$$x = -\frac{\ln(1 - q_x)}{\varrho(E_\pm)} \qquad [2-26]$$

As mentioned before, multiple scattering makes the actual electron trajectory between two radiation points a sort of random path lengthy to be followed. We have approximated it by a straight line segment of length x making an angle ϑ_{eff} with respect to the previous electron flight direction. The equivalent Coulomb diffusion angle ϑ_{eff} has been chosen as an average of the mean square multiple scattering angle [24] between the initial $E_\pm^i$ and the final $E_\pm^f$ electron energies:

$$\vartheta_{eff}^2 = \frac{1}{E_\pm^f - E_\pm^i} \int_{E_\pm^i}^{E_\pm^f} < \vartheta^2 >_E dE \qquad [2-27]$$

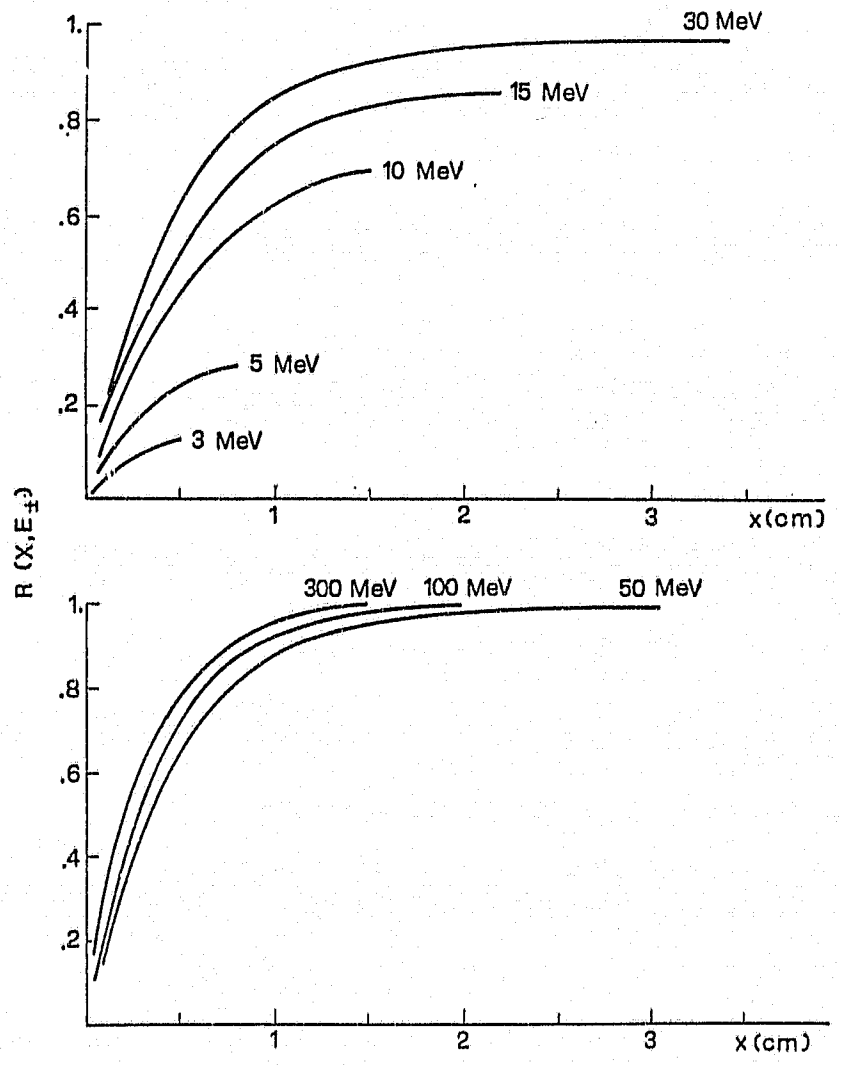

FIGURE 2 Bremsstrahlung plus annihilation in flight probability $R(x, E_{\pm})$ as a function of the electron path length at different energies.

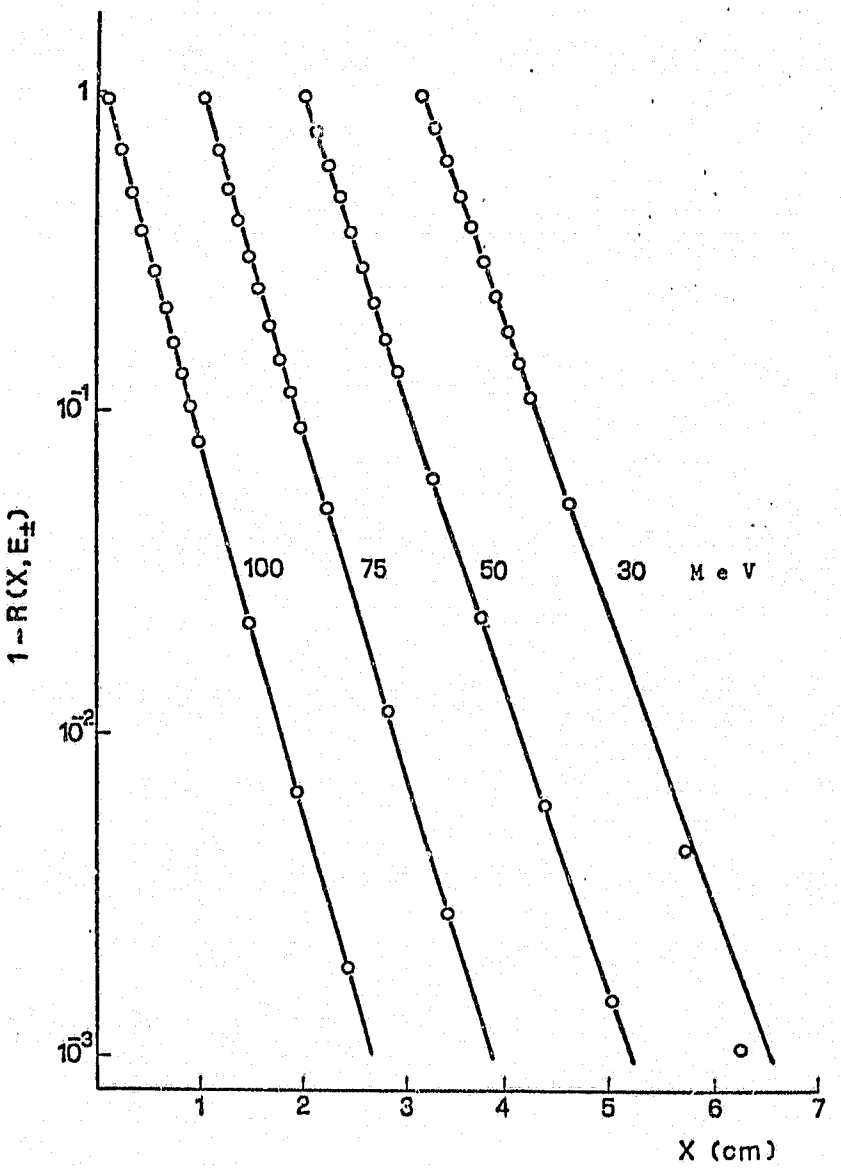

FIGURE 3 Semilog plot of the probability function $1 - R(x, E_{\pm})$.

where $< \vartheta^2 >$ is the multiple scattering angle [24][25]. By this procedure the electron is followed up to the subsequent radiation point; the relative frequency between bremsstrahlung and annihilation-in-flight being determined by the ratio of the macroscopic cross sections at the final electron energy $E^f_\pm$. The bremsstrahlung photon energy k is chosen according to [2-9] in the range between E_{th} and $E^f_\pm$ using the previously quoted electromagnetic cross section [2-14]. For annihilation photons the energies k_1 and k_2 and the polar angles ϑ_1 and ϑ_2 are selected according to [2-15].

In the program the emission point, the energy and the flight direction of each secondary emitted photon are temporarily stored and the electron history followed again up to total energy loss, annihilation at rest, or escape from the crystal boundary. Then the program recalls the secondary photon parameters and follows the photon-electron shower by the same procedures.

2-4 Code tests and discussion

The most delicate approximation involved in this work is the numerical evaluation of the bremsstrahlung cross section [2-8] in the low energy region. Since this approximation should strongly affect the interaction probability [2-18] and, through it, the total electron range, we have checked our calculations by the comparison of the computed electron mean ranges with the predictions obtained by other methods. The range distribution function in NaI(Tl) at different electron energies is reported in figure 4. The distributions are approximately gaussian in the electron energy interval where the total range is much lower than the ionization range R_I [2-19] with a percent straggling approaching 40%. At lower energies the maximum range is given by R_I. The energy dependence of the Monte Carlo mean range $< R > = \int RP(R)dR$ and straggling (computed without multiple scattering) $S = (\int (R - < R >)^2 P(R)dR)^{1/2}$, are reported in figure 5. The full curve is an average range R_{av} calculated in the continuous slowing down approximation over the whole bremsstrahlung energy interval

$$R_{av} = \int_0^{E_\pm - m_0c^2} \left(\frac{dE_\pm}{dx}|_{ion} + \frac{dE\pm}{dx}|_{rad}\right)^{-1} dE_\pm \qquad [2-28]$$

with

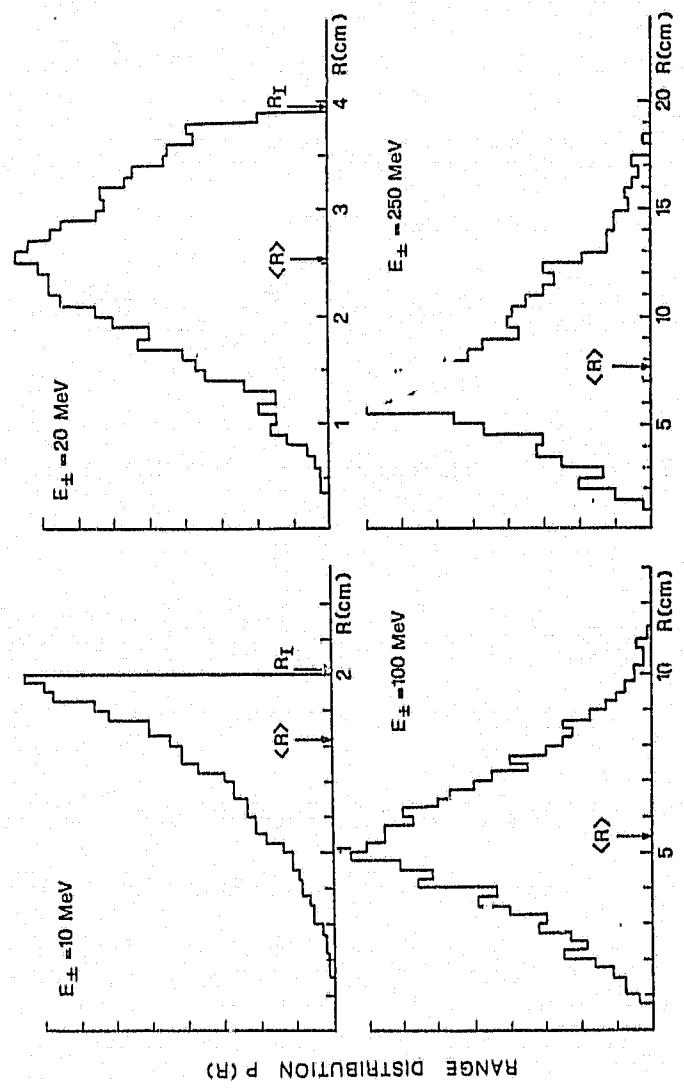

FIGURE 4 Range distribution function $P(R)$ at different electron energies.

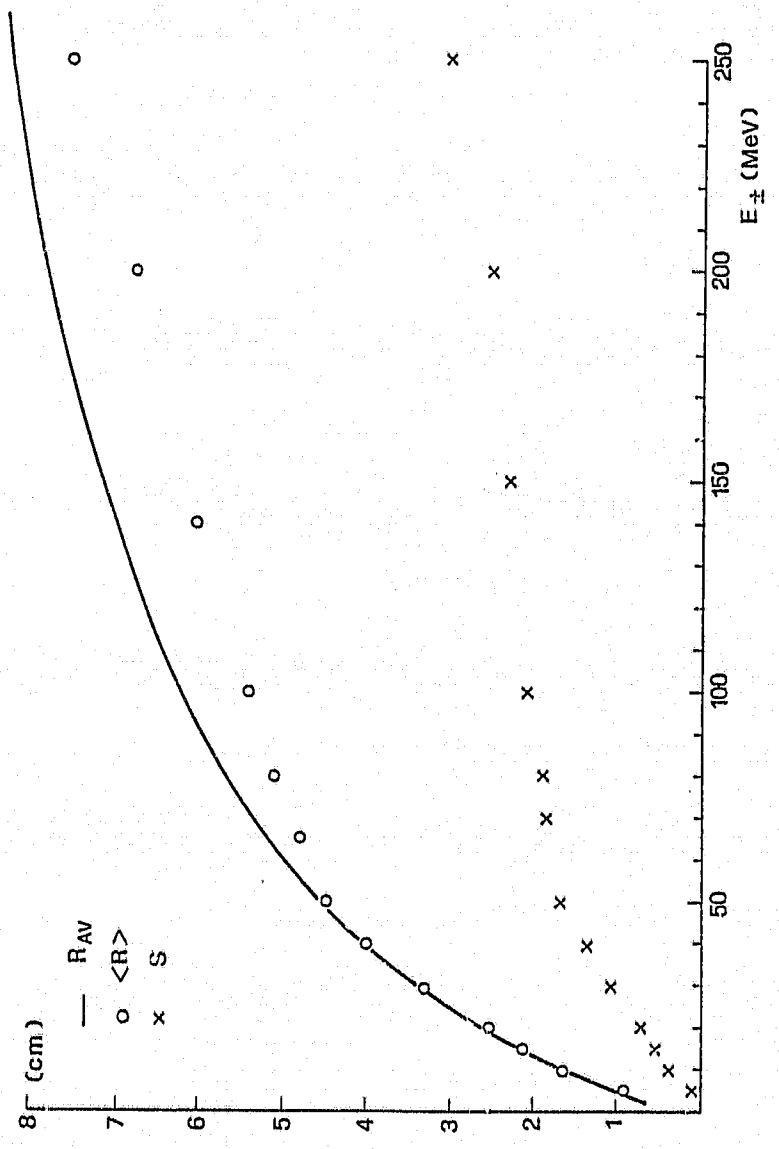

FIGURE 5 Monte Carlo mean range $< R >$, continuous slowing down range R_{av} and straggling S as a function of the electron energy $E_{\pm}$.

$$\left.\frac{dE_{\pm}}{dx}\right|_{rad} = N\sum_{i=1}^{2}\int_{0}^{E\pm-m_0c^2} k\,d\sigma_k|_i\,dk \qquad [2-29]$$

Our R_{av} values [23] are in excellent agreement with similar calculations and coincident up to electron energies around 50 MeV with the computed $< R >$; above this limit the curve gives values systematically higher than our evaluations. This disagreement is not surprising since formula [2-28] ignores large bremsstrahlung losses; and the rate of radiation loss, along the entire track, is always equal to the mean rate $dE_{\pm}/dx|_{rad}$. Range calculations performed using shower theory and the Monte Carlo method by Wilson [27] give $< R >$ values about 20% lower than our estimates with a straggling $S/< R >$ still around 40%. A maximum difference of about 10% between $< R >$ and R_{av} below 300 MeV, is reasonable and is in support of the reliability of this code.

On the other hand the intrinsic response function $F_n(\Delta, E_\gamma)$ i.e. the pulse height Δ distribution corresponding to n monochromatic photons of energy E_γ incident on the scintillator volume and the percent efficiency

$$\varepsilon(E_\gamma) = \frac{1}{n}\int_0^{E_\gamma} F_n(\Delta, E\gamma)\,d\Delta \qquad [2-30]$$

has been evaluated by the code at different photon energies and detector geometries. The comparison of the observed response function $S_n(\Delta, E_\gamma)$ with the experimental data requires a folding of $F_n(\Delta, E_\gamma)$ on the experimental resolution

$$S_n(\Delta, E_\gamma) = \int F_n(\Delta\prime, E_\gamma)G(\Delta\prime - \Delta)\,d\Delta\prime \qquad [2-31]$$

where the resolution function is assumed to be gaussian

$$G(\Delta - \Delta\prime) = \frac{1}{\sqrt{2\pi}\sigma(\Delta)}e^{-\frac{(\Delta-\Delta\prime)^2}{2\sigma^2(\Delta)}} \qquad [2-32]$$

and $\sigma(\delta) = a\sqrt{\Delta} + b\Delta$ consistent with statistical arguments. It should be noted that at photon energies above 20 MeV the statistical resolution σ only affects the high energy side of the absorption peak, the remaining features being mainly fixed by the energy escape probability. Parameters a and b have been determined by a simultaneous analysis of a

set of measurements from the same crystal [28][29]; in the other cases a reasonable percent resolution of 10% at 0.662 MeV (^{137}Cs) has been assumed.

A systematic set of measurements at photon energies between 9 and 60 MeV has been performed by the LADON group in Frascati [28] using their monochromatic and polarized photon beam[30]. The parallel beam was face centered on a cylindrical NaI(Tl) crystal and collimated to a 8 mm spot. The experimental results are reported in figures 6 and 7 together with the computed response functions; the agreement is generally very good except in the case of $E_\gamma = 30$ MeV where the Monte Carlo predictions seem to overestimate the tail at the lower Δ values. Unfortunately the peak tail has been experimentally determined after subtraction of a low intensity photon spectrum due to bremsstrahlung of the electron beam on the residual vacuum of the ADONE storage ring. This subtraction makes the experimental data less reliable in the low Δ region and does not afford any conclusion on the observed discrepancy.

Monochromatic capture photons from $^3H(p,\gamma_0)^4He$ reaction with $E\gamma = 20.5$ MeV have been used [31] to measure the response function of a cylindrical NaI(Tl) crystal. Photons were collected 76 cm away from the target and collimated to a spot of 12 cm diameter on the cylindrical face. The response function $S_n(\Delta, E_\gamma)$ is plotted in figure 8a together with the computed curve. In this case the calculation has been performed using two different values for the effective bremsstrahlung threshold, namely $E_{th} = 50$ keV and $E_{th} = 300$ keV. The agreement is excellent over the whole Δ range and the dependence from the assumed threshold practically negligible.

Real monochromatic photons have been obtained in Saclay [32] by tagging the forward emitted high energy annihilation photon with its low energy partner. The response function at $E_\gamma = 46.5$ MeV of their crystal is shown in figure 9; the beam spot at the detector face was 12.5 cm diameter and the collimation solid angle $5 \cdot 10^{-6}$ sr. The agreement is completely satisfactory also in the low Δ region observed in this experiment without subtraction.

Apart from the few examples selected for this discussion, due to the fact that they concerned real monochromatic photons of reasonably high energy in single sodium iodide crystals; the reliability of this code has been exstensively proved in the past years when it has been applied to the systematic deconvolution of high energy capture γ ray spectra,

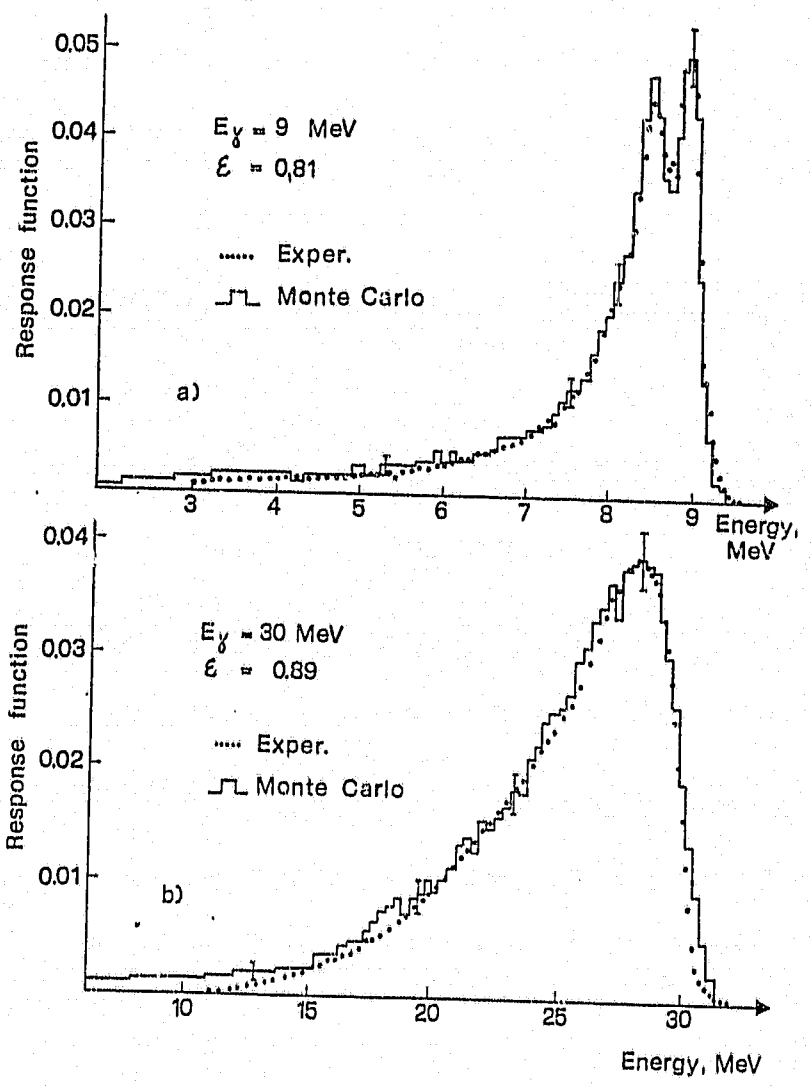

FIGURE 6 Experimental [28] and computed response functions at $E_\gamma = 9$ MeV and $E_\gamma = 30$ MeV normalized to the detection efficiency. The statistical uncertainties on the calculations are reported; experimental errors are comparabable with the spot dimension.

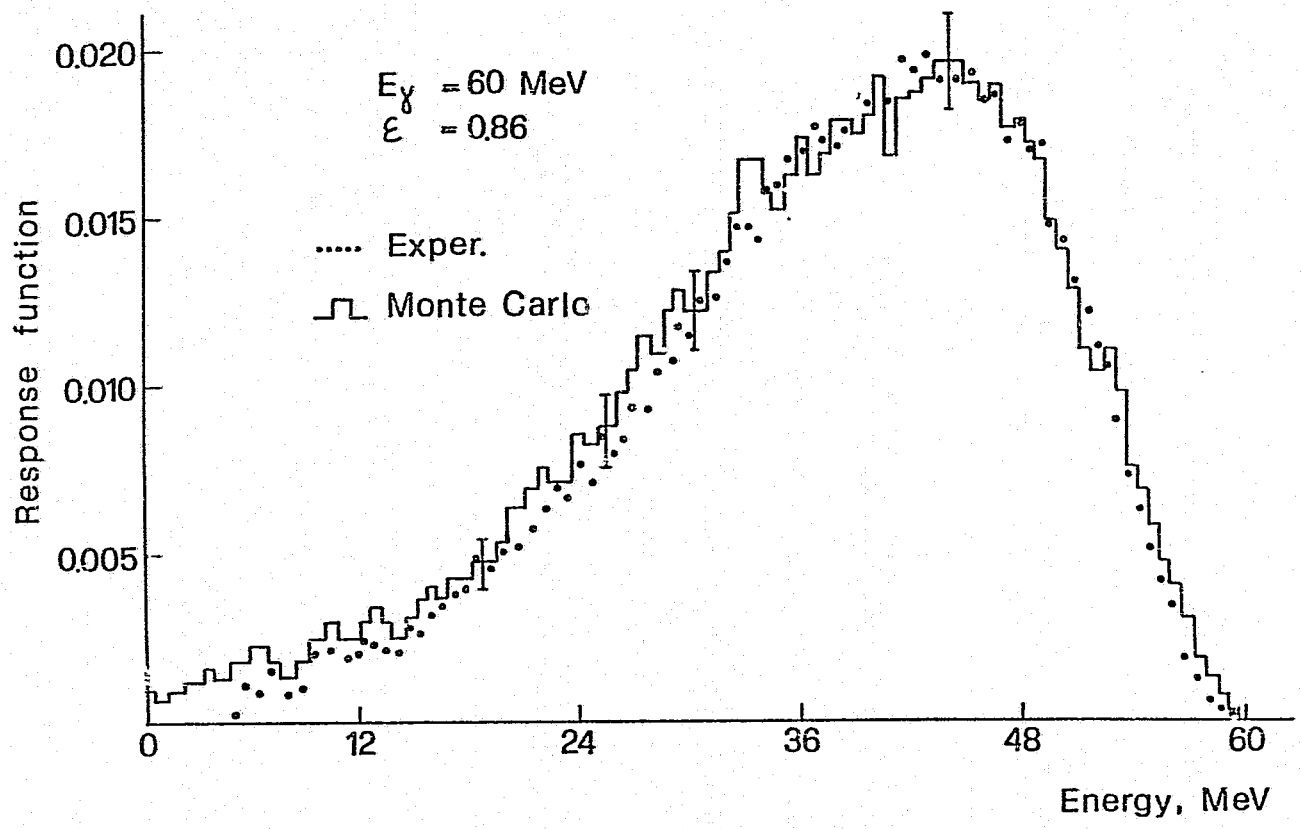

FIGURE 7 Experimental [28] and computed response function at E_γ = 60 MeV.

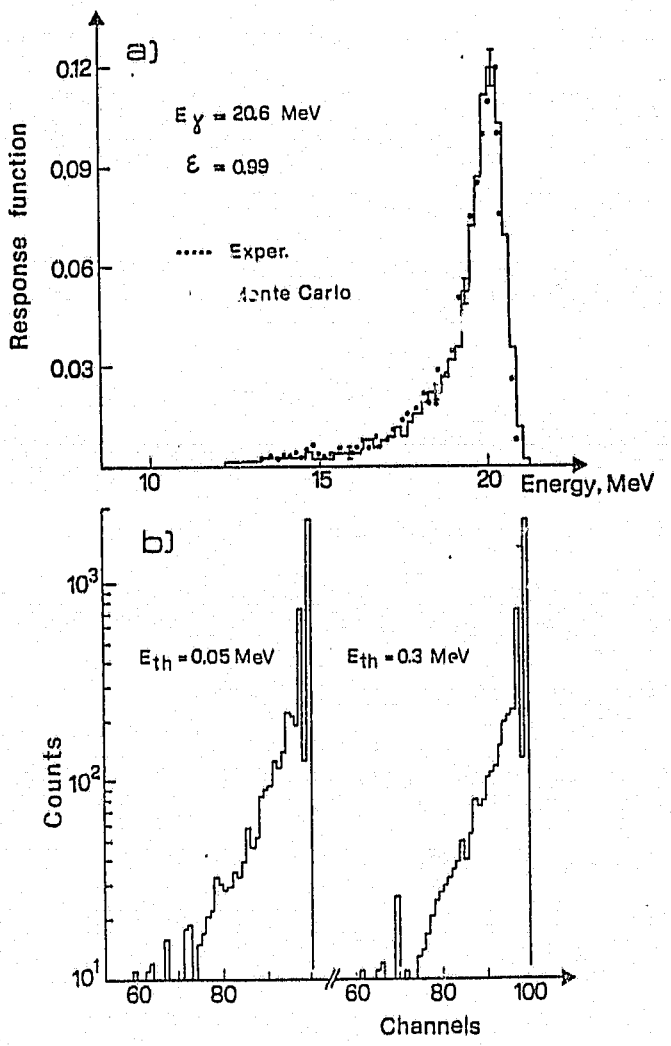

FIGURE 8 *a)* Experimental [31] and computed response function at $E_\gamma = 20.6$ MeV ; *b)* unfolded response function at the same photon energy for two different E_{th} thresholds.

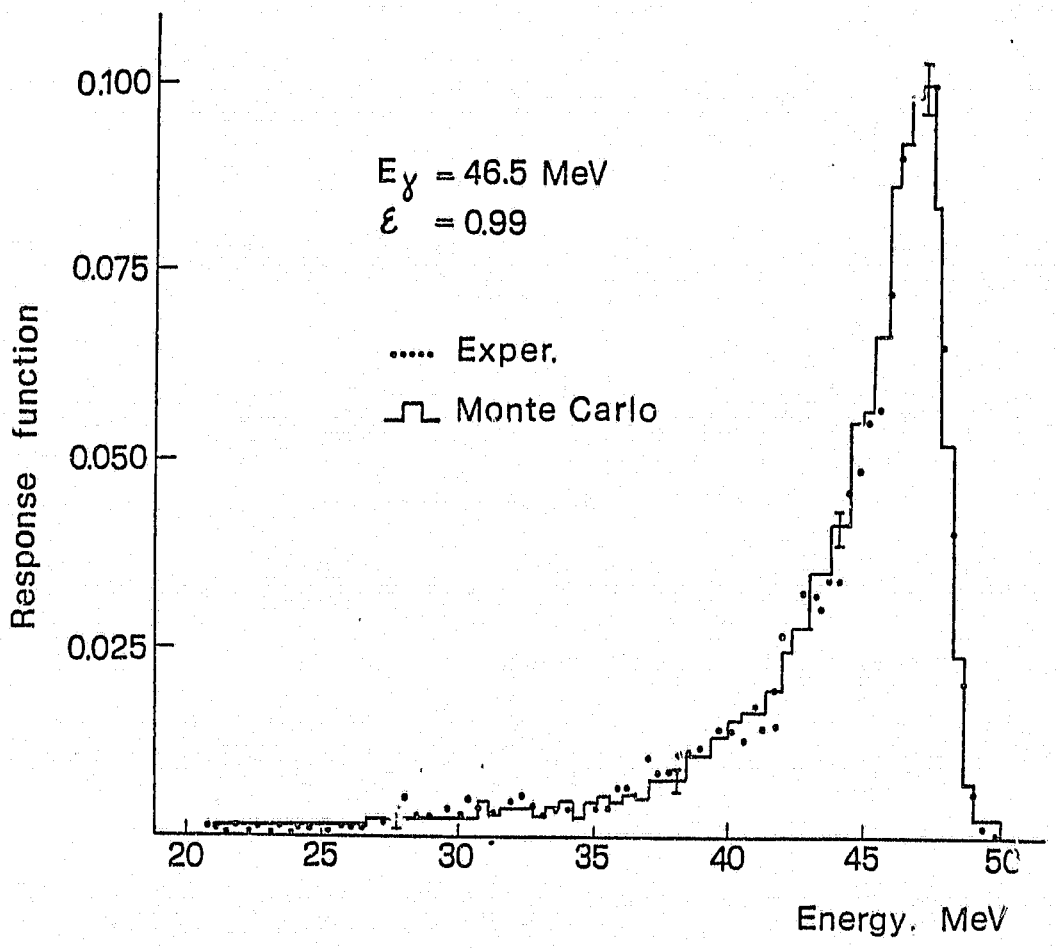

FIGURE 9 Experimental [32] and computed response function at $E_\gamma = 46.5$ MeV

and in comparison [33] to other relevant simulation codes [15] at energies even in the GeV range.

2-5 Configuration selection and geometry calculations

As we have seen, the experiment can be carried out reliably up to about 60 MeV, but in the region of higher energies, where this detector is intended to be specifically used, any increase in the background-to-signal ratio will penalize the evaluation of the contribution due to the low energy tail associated with the total absorption peak. Computed figures give reliable and sometimes unique information, to be used both in the design stage, as we shall now see, and in the deconvolution of experimental spectra.

We have followed a design philosophy which has permitted a series of refinements resulting in an appreciable improvement of the overall detector performance [5]. The configuration which we use for calculation of the detector performance is sketched schematically in figure 10; it includes as sensitive elements a main NaI(Tl) crystal and two plastic scintillator detectors, one as a front plug and the second as an annulus surrounding the main detector. Also included in our considerations are the substantial lead shields which serve to collimate the primary photon beam but also to reduce the environmental background and to convert the hard muon component of the cosmic radiation. Optimal detector dimensions are reported in the table associated with figure 10. The code follows the development of the electromagnetic shower inside these shields in the same way as it does in the active elements of the spectrometer accounting for collimation effects and eventual conversion of primary photons [34]. Additional shielding layers for neutron moderation (e.g. paraffin) and neutron absorption (e.g. LiH) may be required to reduce the diffuse neutron background but these have not been included in our calculations.

Critical dimensions which we determine are firstly the length and diameter of the NaI(Tl) crystal, since these affect both the resolution and efficiency, and secondly the thickness and length of the anticoincidence shield, since these determine the efficiency of rejection of the energy escape from the crystal boundaries as well as the efficiency of rejection for the cosmic component.

Regarding the correct NaI(Tl) size, we can show, by comparing the results obtained

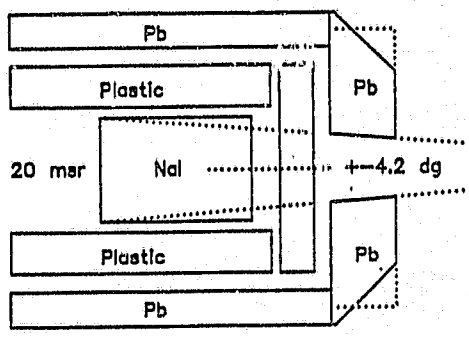

	ID	OD	L	TD
NaI	---	23.81	35.56	120.00
Disc	---	46.58	8.05	105.25
Annulus	28.88	48.56	80.97	115.38
Pb later.	57.00	73.00	75.00	101.50
Pb front	13.28	65.00	15.00	86.5

FIGURE 10 Schematic diagram of the spectrometer configuration used in the numerical calculations. The dotted lines refer to the cylindrical shape used in the calculations for the front lead collimator, the actual ones being conical as indicated by the full lines. The table (Table I) summarizes the basic dimensio in the definitive configuration of the spectrometer(ID=inner diameter, OD=outer diameter,L=lenght and TD=detector-target distance).

for a single crystal illuminated along its axis by a photon beam of energy up to 100 MeV, that while the detection efficiency exhibits small variations [35] with the absorption length when this increases above 20 cm, never the less the resolution (figure 11) continuously improves up a to detector length of about 35 cm. This detector is therefore chosen to have a length of 35.8 cm. The crystal diameter, as in all of the few large γ-ray spectrometers now in operation, is chosen to be about 24 cm. This matches current manufacturing capabilities and has proven to be effective since it represents a good compromise between the angle of collection for the reaction photons, which must be kept reasonably small (± 5 deg) if one is to resolve details of the experimental angular distribution, the efficiency of collection of the electromagnetic shower and the need to reduce the crystal volume in order to optimize both the light collection (and consequently the resolution) and the overall cost of the device.

With an efficient anticoincidence shield a crystal having a diameter of 23.8 cm, such as this one, can be used for photon beams up to 100 MeV with no appreciable loss of efficiency while still maintaining a reasonably small angle of collection and a convenient detector-target distance. The distance will be set in our case at 120 cm since it will then allow efficient $\gamma - n$ discrimination by the time-of-flight technique, while still subtending at the detector a solid angle of 20 msr and a collection angle defined at ± 4.2 deg.

For this assembly we have studied particularly [36] the effect of the two (front and lateral) anticoincidence detectors. They play some important roles in the overall performance of the spectrometer. Firstly, they detect escape events and, in the anticoincidence (reject) mode, they maintain the best peak energy resolution, albeit at the expense of the detection efficiency. Secondly, they provide rejection for external cosmic ray events, which, for radiative capture reactions at high energies, will have a count rate comparable if not bigger than that for "true" events. Thirdly, they act as moderators for the (slow) neutron background, but the code used is not able to account for this effect.

In computing spectra for the anticoincidence configuration we choose to group the energy deposited in the NaI(Tl) in intervals of $\Delta E_\gamma = 0.01 E_\gamma$. We then consider the effect of the front plastic scintillator on the resolution and efficiency of the spectrometer for four incident energies, 25, 50, 75 and 100 MeV respectively (figures 12 and 13). The combined anticoincidence shield (annulus + front disc) has an outer diameter of 48.6 cm, the annulus

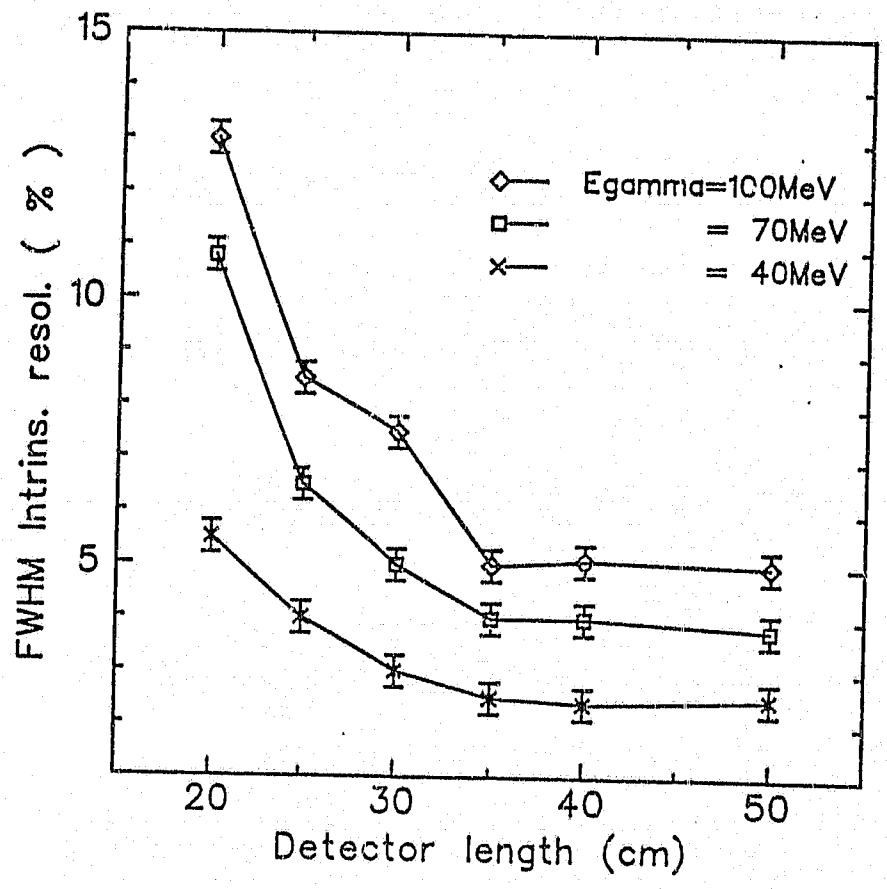

FIGURE 11 The intrinsic FWHM resolution of a single 24 cm diameter NaI crystal as a function of the detector length for three different photon energies.

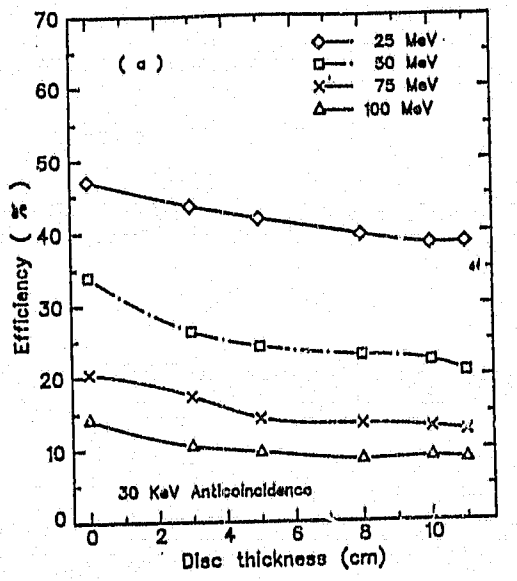

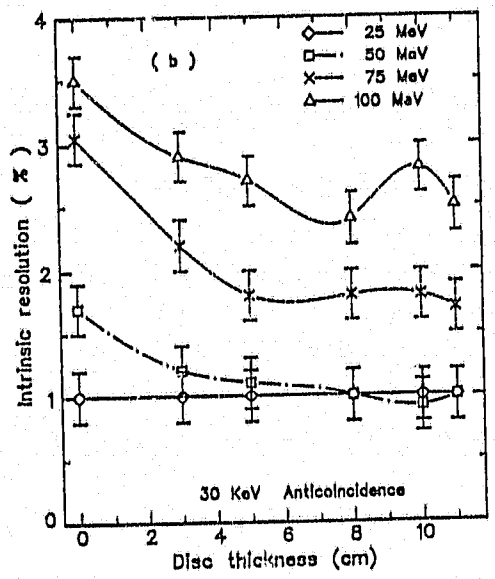

FIGURE 12 Efficiency (part a) and resolution (part b) of the full anticoincidence γ spectrometer as a function of the front disc thickness for four diff(ent energies. The anticoincidence shield energy threshold is fixed at 30 keV .

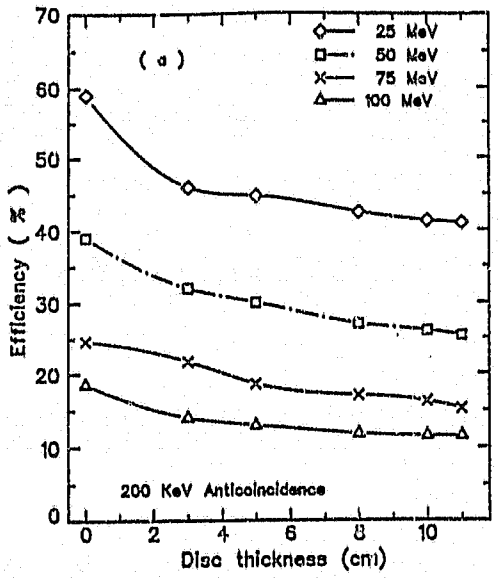

FIGURE 13 Efficiency (part a) and resolution (part b) of the full anticoincidence γ spectrometer as a function of the front disc thickness for four different energies. The anticoincidence shield energy threshold is fixed at 200 keV .

being 9.86 cm thick and 60.9 cm long. Errors in the efficiency curves are not shown but a relative error between 1.3% (25 MeV at 200 keV threshold) and 3.4% (100 MeV at 30 keV threshold) represents our best estimate. The 1% resolution values at 25 MeV (figures 12 and 13) reflect the fact that with the selected energy resolution of $\Delta E_\gamma = 0.01\, E_\gamma$, the contribution of the total absorption peak is limited to one single energy channel in our computer calculation, and indeed clearly separated from those of the first ($E_\gamma - 0.511$ MeV) and second ($E_\gamma - 1.022$ MeV) escape peaks. The 30 keV anticoincidence threshold case (figure 13) and the 200 keV case (figure 14) do not show substantial differences in either efficiency or resolution for a front disc of 8 or 10 cm: the efficiency curves are found to vary smoothly in that range, and both sets of resolution values fall within the computational errors (although some small fluctuations are revealed in these curves). Front cap thickness of less than the 8 cm selected are not recommended since, as can be seen, the FWHM values (expressed as a percentage), increase appreciably for a smaller disc thickness or for higher energies.

In a similar way we consider the combined effect of the disc thickness and both the annulus thickness and its length. For photons of 50 MeV and the two different anticoincidence thresholds used (30 keV in figure 14 and 200 keV in figure 15) we have plotted the efficiency (figures 14a and 15a) and resolution (figures 14b and 15b) as a function of three sets of parameters given in Table I.

TABLE I

Anticoincidence size

Case	Annulus length	Ann. thickness	Ann. and disc diam.
1	60.9 cm	9.86 cm	48.6 cm
2	60.9	8.86	46.6
3	45.9	9.86	48.6

As is evident from the calculations a reduction in the annulus thickness (case 2) improves the overall detection efficiency for the full anticoincidence detector configuration, since the smaller volume of the annulus in which the interaction takes place of the escape

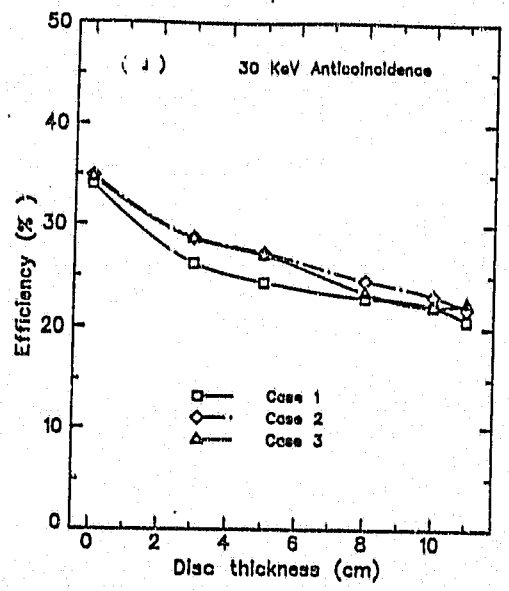

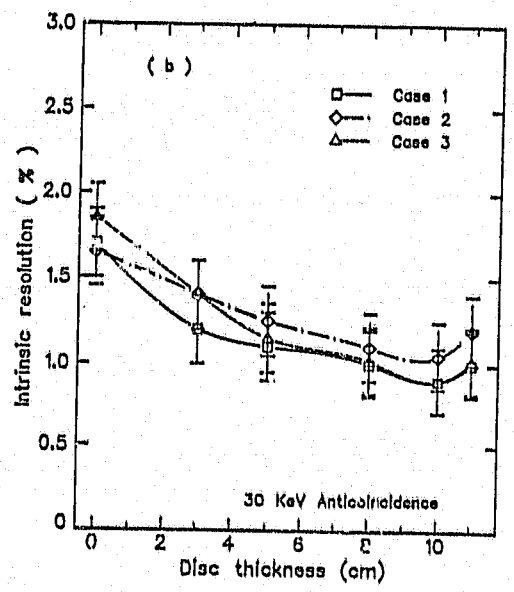

FIGURE 14 Efficiency (part a) and resolution (part b) as a function of the front disc thickness for several choices of the annulus length and thickness. The three cases are summarized in table I. The anticoincidence energy threshold is fixed at 30 keV .

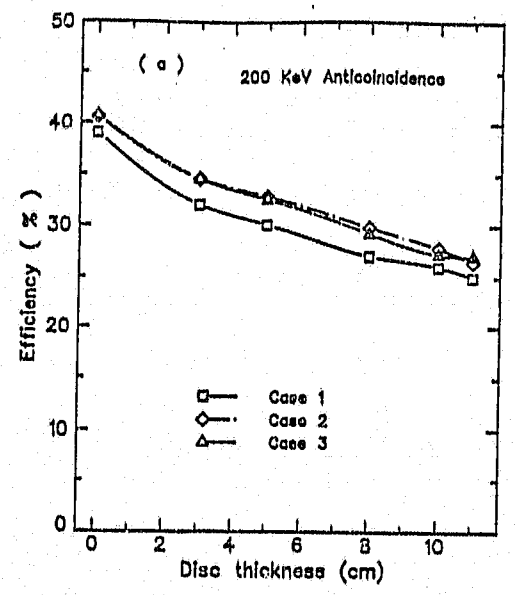

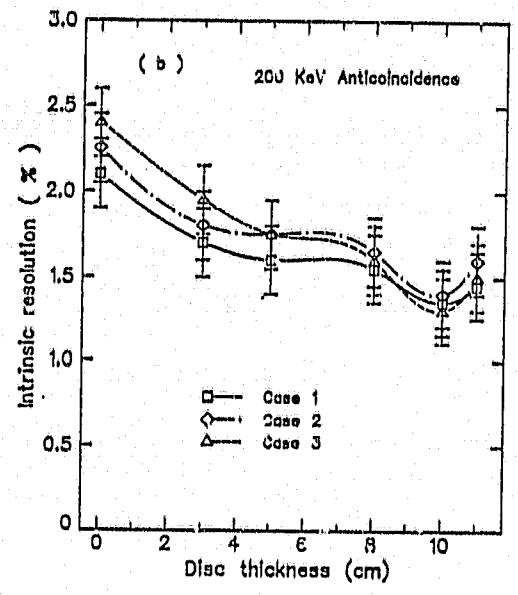

FIGURE 15 Efficiency (part a) and resolution (part b) as a function of the front disc thickness for several choices of the annulus length and thickness. The three cases are summarized in table I. The anticoincidence energy threshold is fixed at 200 keV .

gammas, reduces the rejection probability. On the one hand, not extending the annulus over the full main crystal length introduces no appreciable changes in the efficiency and resolution results, since the main crystal length is already quite adequate for this diameter to contain in the crystal volume the full electromagnetic shower for an incident photon of even 100 MeV. On the other hand, it is obviously important to reduce by as much as possible the solid angle for cosmic rays to reach the main crystal with zero (or very low) probability of interaction in the anticoincidence shield. For this reason the extension of a thick annulus ($\approx$ 10 cm) beyond the end of the NaI(Tl) crystal must prove worthwhile. Based on these arguments we have selected the set of detector parameters reported in figure 10, for further representative calculations.

The detector response functions for this configuration, for both the single main crystal and the full anticoincidence configuration, are presented in figure 16. The good intrinsic energy resolution obtained in each case up to 40 MeV incident gamma energy as well as the evident improvement introduced as a result of using energy escape rejection in the high energy response functions, confirm the excellent performance characteristics of such a configuration. Detector resolution and efficiency are the fundamental parameters of any γ spectrometer and are presented for this instrument, in its final chosen dimensioned configuration, in figures 17 and 18. Also shown in figure 17 are the actual measured FWHM experimental points taken on the nearest similar spectrometer [5]. The overall resolution of such an instrument depends on three terms:

- $R_I(E)$: the intrinsic resolution which, as we see from figure 17, is energy dependent
- $R_S(E)$: a term related to the statistics associated with the number of photoelectrons collected at the photocathode and with an energy dependence given by $R_S(E) = 1/\sqrt{PE}$ where P is the average number of photoelectrons collected per unit energy released in the scintillator
- R_0: a term not related to energy but depending inter alia on the uniformity and efficiency of light collection from the detector volume, on the uniformity of the photocathode response and on the gain stability of photomultipliers.

Our final detector configuration incorporates a series of quite remarkable technical

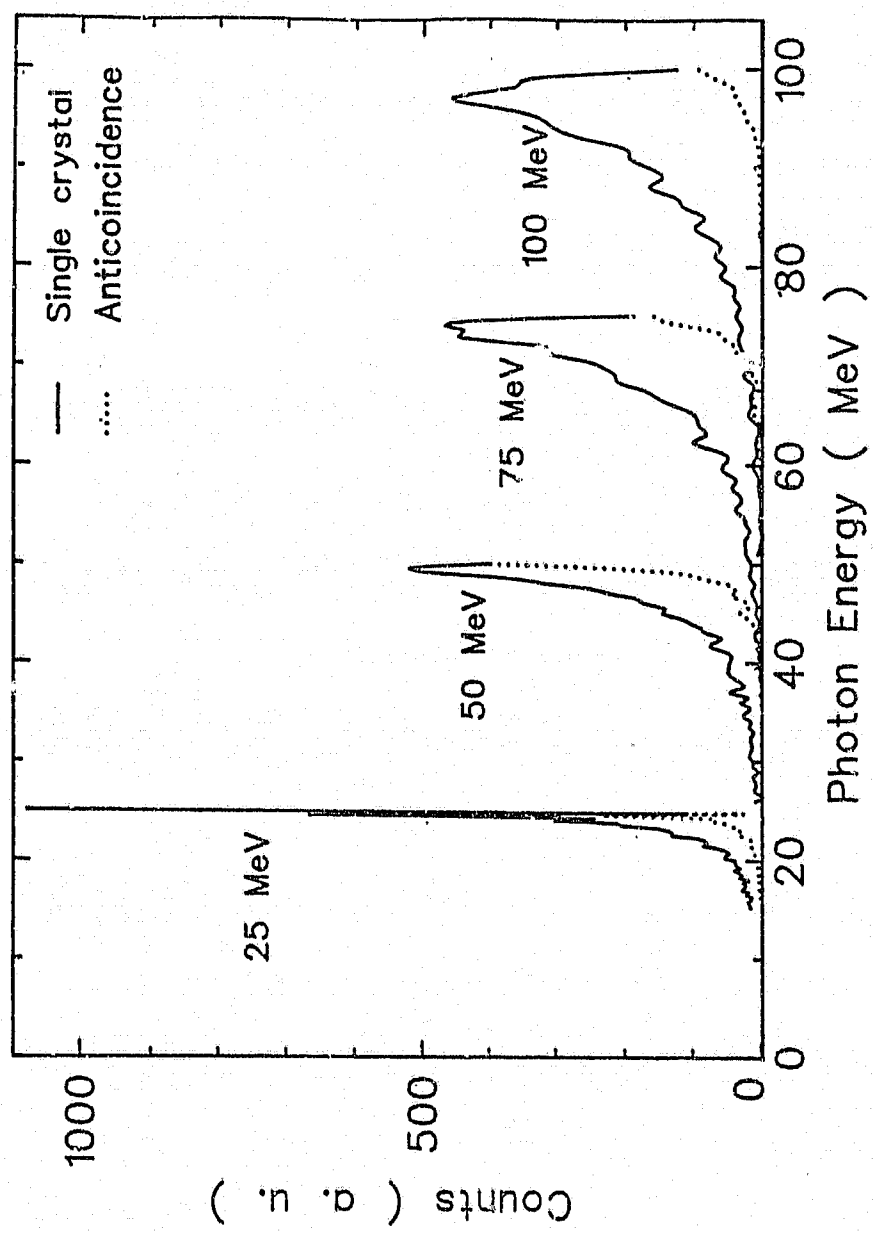

FIGURE 16 The single crystal (full lines) and the anticoincidence (dashed lines) intrinsic response function for the γ spectrometer as computed by the Monte Carlo code at four different energies. Counts are in arbitrary units.

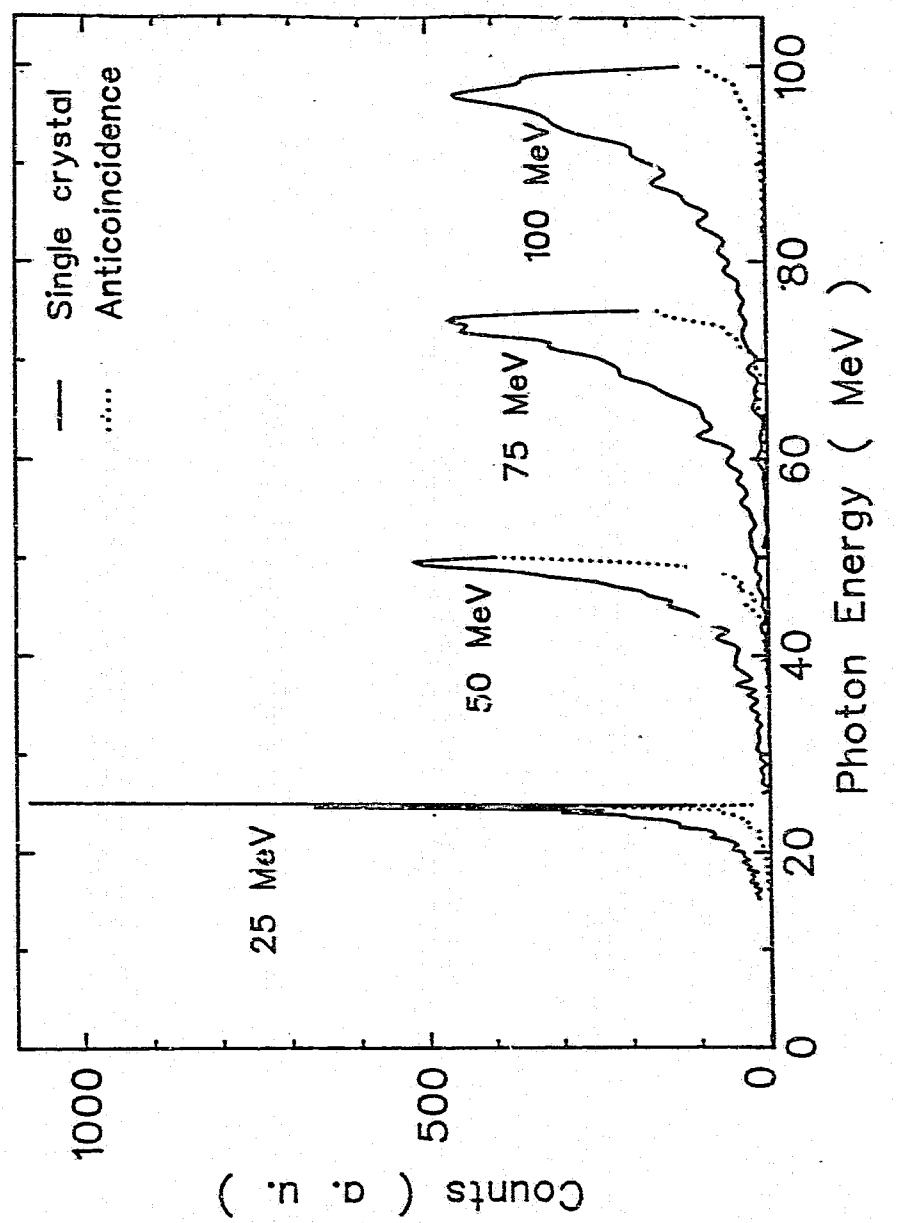

FIGURE 16 The single crystal (full lines) and the anticoincidence (dashed lines) intrinsic response function for the γ spectrometer as computed by the Monte Carlo code at four different energies. Counts are in arbitrary units.

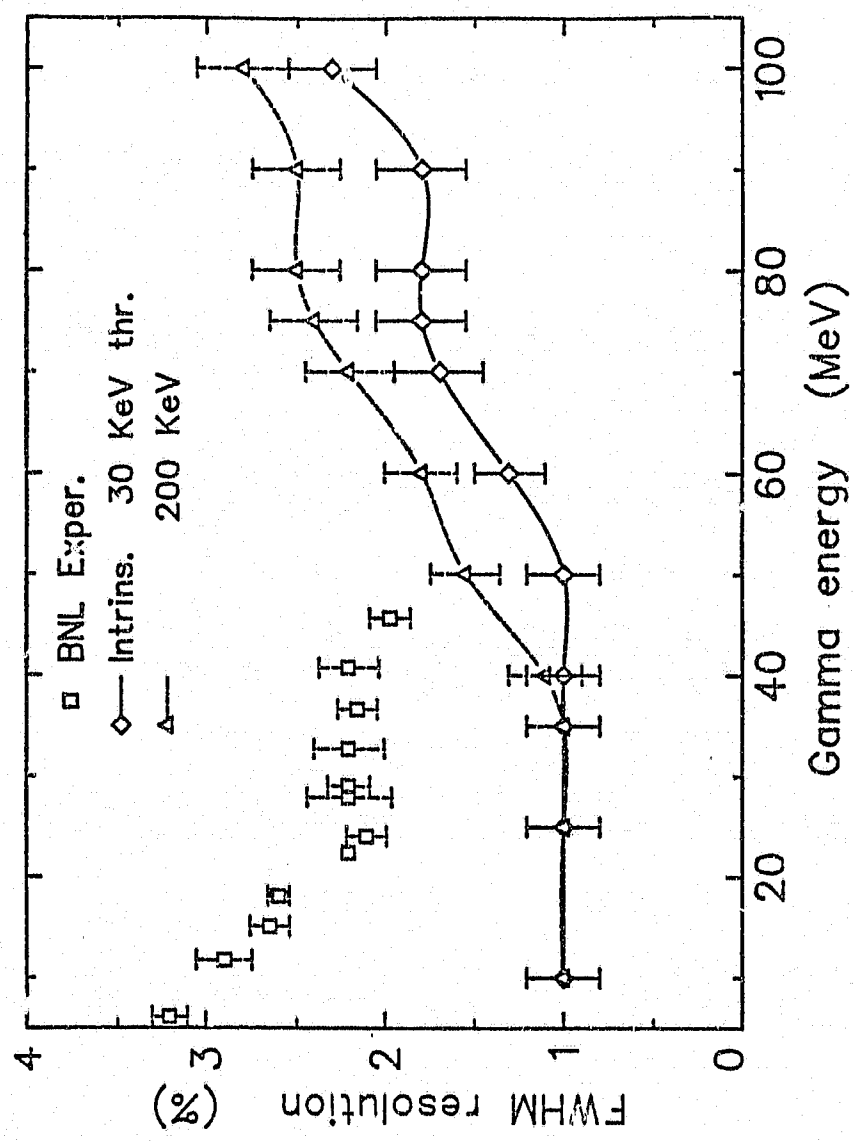

FIGURE 17 Intrinsic FWHM resolution as a function of the photon energy for two values of the anticoincidence threshold: 30 keV (full line) and 200 keV (dashed line). Also shown are the experimental points obtained for the nearest similar spectrometer [5].

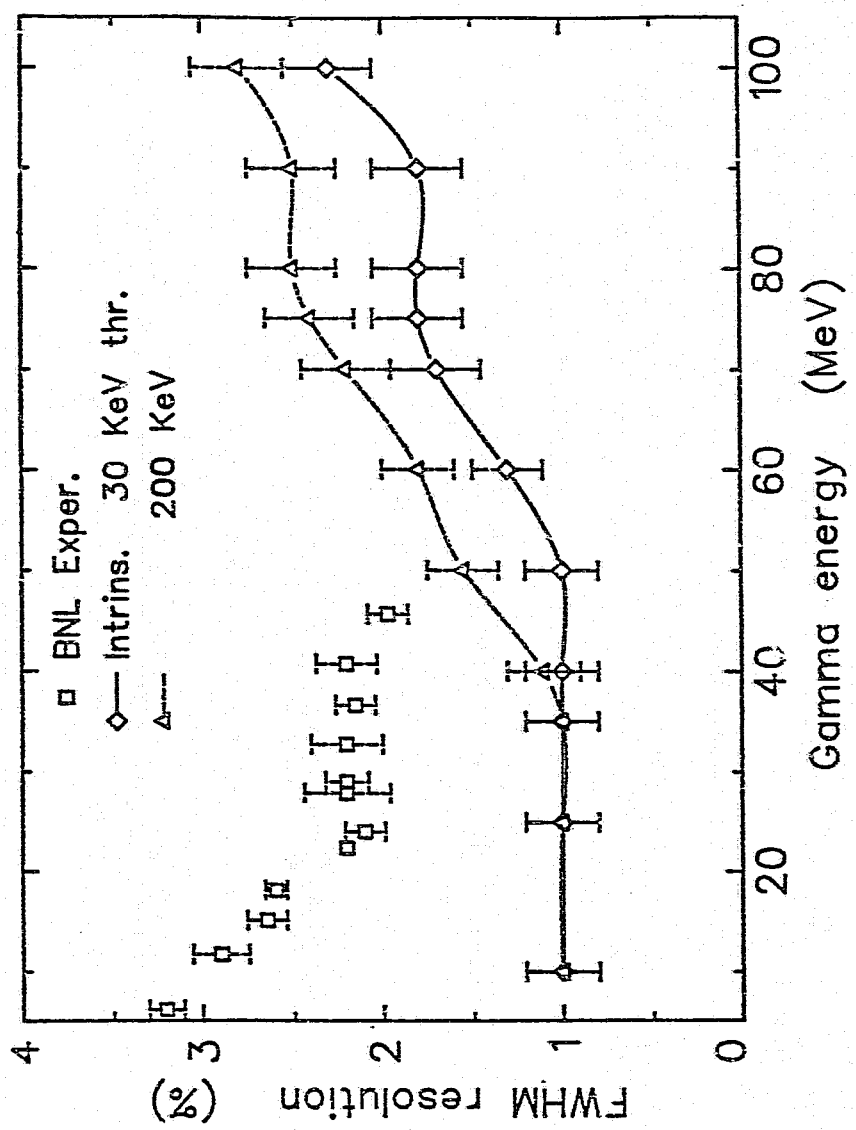

FIGURE 17 Intrinsic FWHM resolution as a function of the photon energy for two values of the anticoincidence threshold: 30 keV (full line) and 200 keV (dashed line). Also shown are the experimental points obtained for the nearest similar spectrometer [5].

improvements which prove to be highly effective in reducing R_0, resulting in an overall excellent performance up to 46MeV (figure 17) as measured on the nearest similar instrument[5]. This point will be discussed later when describing the construction details of our detector. The three resolution terms couple quadratically to give

$$R_T(E) = \sqrt{R_S^2(E) + R_0^2 + R_I^2(E)} \qquad [2-33]$$

As shown in the data of figure 17, the experimental points (for BNL) show a trend of improving resolution with increasing photon energy up to about 25 MeV, where the statistical contribution R_S is dominant and the intrinsic R_I still negligible. In the region between 25 and 50 MeV the statistical contribution falls below R_0 while the effect of R_I is still not appreciable, as is shown by the constancy of the experimental curve, reflecting a behaviour typical of an energy independent R_0 term. Above 50 MeV the resolution figures will certainly deteriorate due to the greater effect of energy escapes on the crystal response function.

Taking these results into consideration we can infer also that this instrument can be operated at high anticoincidence thresholds ($200 - 300$ keV) up to $E_\gamma = 40$ MeV which will improve the count rate capability without any appreciable deterioration in the overall FWHM energy resolution. But above $40 - 50$ MeV it should increasingly be operated at the lowest possible anticoincidence threshold (typically 30 keV) since in this energy region the peak resolution will be the major limiting factor in the spectrometer performance.

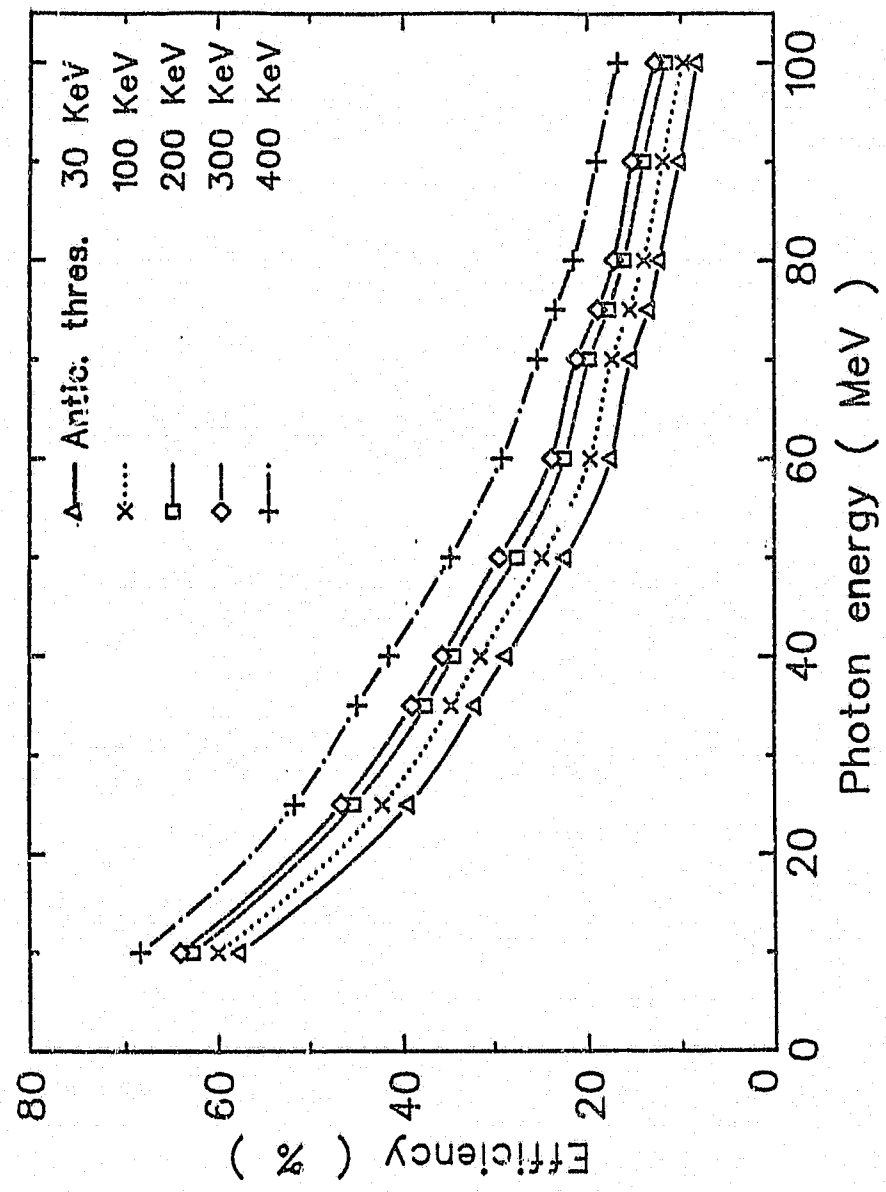

FIGURE 18 The spectrometer efficiency in the full anticoincidence configuration as a function of the photon energy for five different anticoincidence thresholds: 30, 100, 200, 300, and 400 keV .

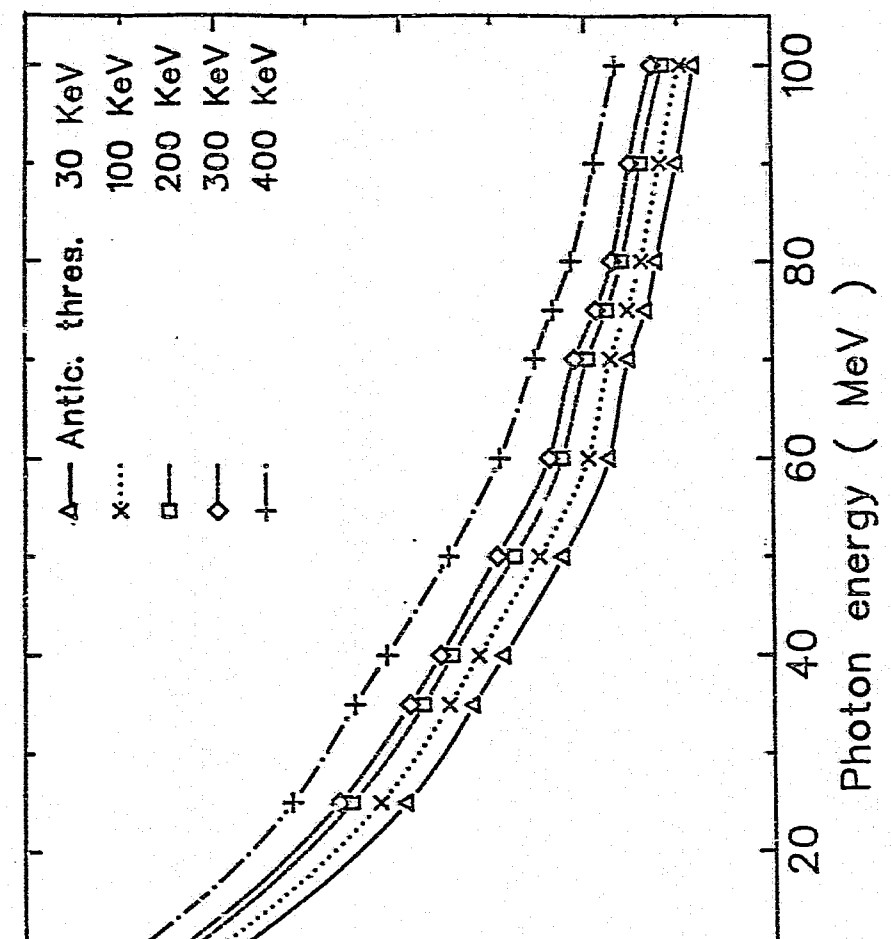

FIGULE 18 The spectrometer efficiency in the full anticoincidence configuration as a function of the photon energy for five different anticoincidence thresholds: 30, 100, 200, 300, and 400 keV .

REFERENCES FOR CHAPTER 2

1) M.D.Hasinoff, S.T.Lim, D.F. Measday and T.S.Mulligan
Nucl. Instr. and Meth. 117(1974)379

2) M.Suffert, W.Feldman, J.Mahieux and S.S.Hanna
Nucl. Instr. and Meth. 63(1968)1

3) E.M.Didier, J.F.Amann, S.L.Blatt and P.Paul
Nucl. Instr. and Meth. 83(1970)115

4) M.Anghinolfi, P.Corvisiero, E.Durante, M.Guarnone, M.Taiuti and A.Zucchiatti
Il Nuovo Cim. 77A(1983)277

5) A.M.Sandorfi and M.T.Collins
Nucl. Instr. and Meth. 222(1984)479

6) T.Kishimoto, T.Shibata, M.Sasao, N.Nomauchi and H.Ejiri
Nucl. Instr. and Meth. 198(1982)269

7) C.D.Zerbi and H.S.Moran
Nucl. Instr. and Meth. 14(1961)115

8) M.Gianniri, P.R.Oliva and M.C.Ramorini
Nucl. Instr. and Meth. 81(1970)104

9) M.J.Berger and S.M.Seltzer
Nucl. Instr. and Meth. 104(1972)317

10) T.Nakamura
Nucl. Instr. and Meth. 105(1972)77

11) M.Belluscio, R.De Leo, A.Pantaleo, and A.Vox
Nucl. Instr. and Meth. 118(1974)553

12) S.M.Seltzer
Nucl. Instr. and Meth. 127(1975)293

13) B.Grosswendt and E.Waibel
Nucl. Instr. and Meth. 133(1976)25

14) R.L.Ford and W R.Nelson
Report SLAC-210(1978)

15) W.R.Nelson

Report SLAC265(1985)

16) E.D.Cashwell and C.S.Everett
"*Monte Carlo Methods for Random Walk Processes*" Pergamon Press 1975

17) M.Taiuti
Thesis, University of Genova, unpublished

18) E.Storm and N.I.Israel
*Nucl. Data Tab.*A3(1970)565

19) R.M.Sternheimer
Phys. Rev. 103(1956)514

20) L.Marton
"*Methods of Experimental Physics*" vol 5A Academic Press 1963

21) H.W.Koch and S.W.Motz
Rev. Mod. Phys. 31(1959)920

22) W.Heitler
"*The Quantum Theory of Radiation*" Oxford Clarendon 1959

23) P.Corvisiero, F.Masulli and A.Zucchiatti
Report LNF-79/2(R)

24) G.Moliere
Z. Naturforsch. 2A(1947)133

25) W.T.Scott
Rev. Mod. Phys. 35(1963)231

26) M.J.Berger and S.M.Seltzer
Nucl. Science Series 39(1964)205

27) R.R.Wilson
Phys. Rev. 84(1951)100

28) G.Matone
Private communication(1981)

29) *A.Veyssiere*
Private communication(1981)

30) *R.Caloi, L.Casano, M.P.De Pascale, L.Federici, S.Frullani, G.Giordano,*

B.Girolami, G.Matone, M.Mattioli, P.Pelfer, P.Picozza,E.Poldi, D.Prosperi and C.Schaerf
Lect. Notes in Phys. 108(1979)234

31) G.Kernel, W.H.Mason and N.W.Tanner
Nucl. Instr. and Meth. 89(1970)1

32) A.Veyssiere, H.Beil, R.Bergere, P.Carlos, J.Fargot and A.Lepretre
Nucl. Instr. and Meth. 165(1979)417

33) M.Mattioli
Private communication(1986)

34) *P.Corvisiero, M.Taiuti, A.Zucchiatti and M.Anghinolfi*
Nucl. Instr. and Meth. 185(1981)251

35) M.Taiuti, M.Anghinolfi,P.Corvisiero, G.Ricco and A.Zucchiatti
Nucl. Instr. and Meth. 211(1983)135

36) A.Zucchiatti and J.P.F.Sellschop
South Afr. J. . . . Phys. 9(1986)24

CHAPTER 3

SPECTROMETER SET UP AND TESTS

3-1 Spectrometer layout

The actual **H***igh energy* **A***nticoincidence* **GA***mma* **R***ay* (**HAGAR**)spectrometer has the configuration indicated by the cut view in figure 1. It consists of three detectors:

- a NaI(Tl) cylinder (Ø= 23.8 cm, height= 35.6 cm) seen by seven RCA 4900 7.6 cm photomultipliers;
- an annulus of plastic scintillator (BC408) (inner Ø= 28.86 cm, thickness= 9.84 cm, length= 61 cm) divided into six optically separated sectors each seen by two Amperex XP-2202 5 cm photomultipliers;
- a front disc (Ø= 48.58 cm, thickness= 8 cm) seen by three XP-2202 photomultipliers sitting on the disc side and spaced 120 degrees to each other.

The assembly is completed by a cast modular interlocking lead shield extending both laterally and in front for a shielding thickness of not less than 11 cm with a maximum of 25 cm in the direction of the target. Photon collimation is insured by a component of this shield which can be easily replaced if a different solid angle has to be selected. In the test runs we are now considering, the collimation was such that with the sodium iodide front surface positioned 120 cm away from the target, the whole back surface of the crystal was spanned by the reaction photons. This is precisely the situation shown by the spectrometer section of figure 1.

The detectors have been manufactured by Bicron Corporation, following the remarkable improvements obtained with the Brookhaven MKIII model [1]. The characteristics of these detectors are:

a) the NaI(Tl) is grown as a single ingot, Bicron being the builder of the largest single ingot crystals in the world, with factory capabilities already at a record size of 19 in Ø × 19 in. With such large sizes involved two factors can seriously affect the de-

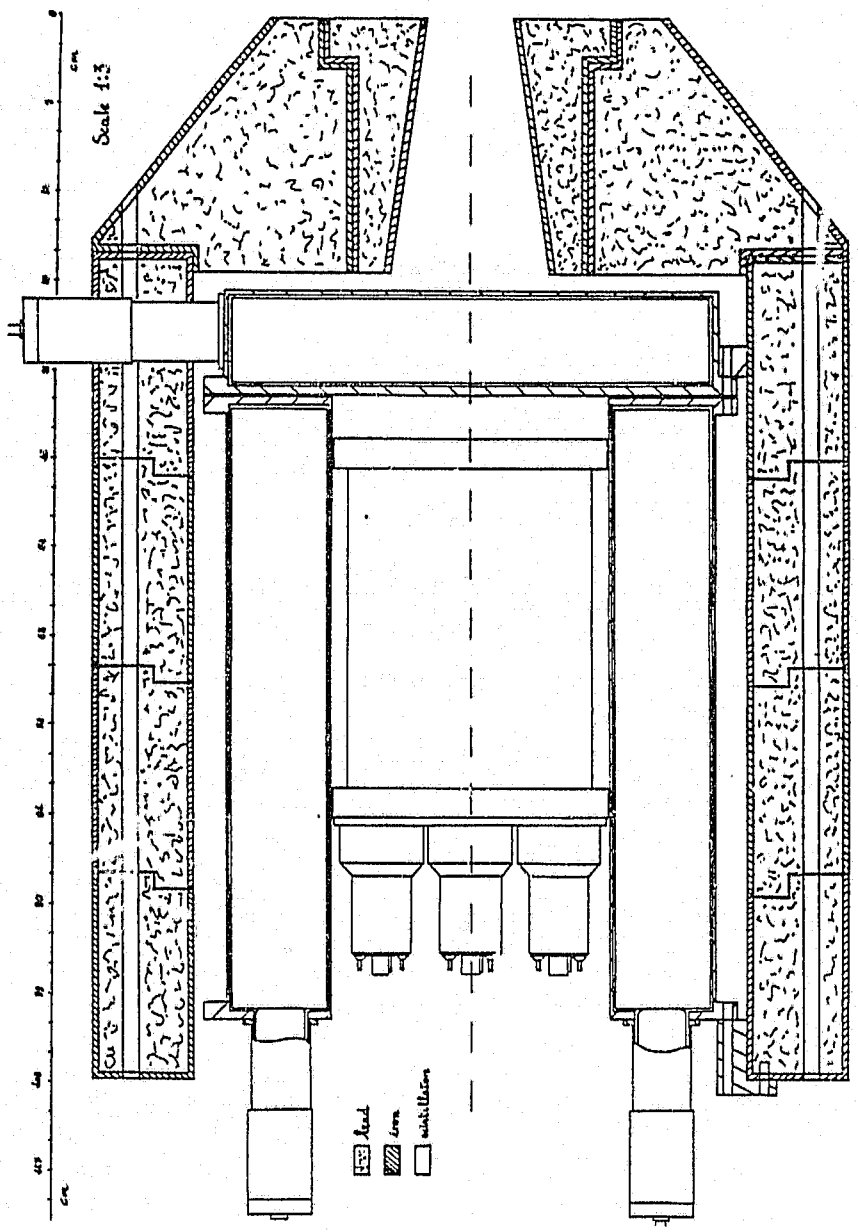

FIGURE 1 Cross section over the three scintillators and the lead shield and collimator.

tector response uniformity if not taken under stringent control. One is the possible non-uniform distribution over such a large volume of the crystal dopant (Thallium). This is dependent on the crystal growing technique, but the results obtainable with current facilities are definitely satisfactory on this point. The second is the ultimate variability of the reflection properties at the crystal edges, which could be due both to crystal cutting and polishing and to the application of the reflector layer between crystal and housing. Non-uniform surface patches could therefore affect the intensity of emitted light, to an extent depending on the smaller or larger solid angle under which the patch is seen from different crystal points and consequently produce considerable disuniformities over the volume of interaction for the detected particles. The techniques to achieve the best surface perfection are continuously in progress, using a multiple muon scan over the whole scintillator volume. The factory process that has been adopted for our crystal, is still the most usual and convenient in the size range of our interest. It consists of an accurate polishing of the crystal surface and deposition of the reflector layer, imposing uniformity contraints at 6.13 MeV ($^{244}Cm - ^{13}C$ source; average penetration depth 8 cm), instead of at 0.661 MeV as usually before (^{137}Cs; penetration depth 1 cm). We shall see how iterating this polishing technique improves considerably the uniformity of light collection from any point of the crystal and therefore the ultimate energy resolution of the detector.

b) The plastic shell is divided into six optically separated sectors each seen by two photomultipliers. This ensures much better light collection than that of a single annulus or a double semi-shell anticoincidence shield. There is a double advantage in doing this, namely in overall resolution and in uniformity. The resolution of the entire annulus can in fact be improved on that of a single sector, provided a correct intercalibration is made to reduce the non-uniformity contributions thus allowing a more precise definition of the energy threshold in the anticoincidence detector and a more accurate rejection of events falling on the peak tail. The inclusion of the front disc, whose geometry cannot match the same, excellent light collection conditions of the annulus sectors, does not alter appreciably the overall performance of the (annulus + disc) anticoincidence shield that can be tuned sector-by-sector for a negligible response

uniformity spread. This avoids square summing of the uniformity spread contribution , light collection statistics which remains,in practice, the ultimate parameter responsible for total energy resolution.

c) great care has to be devoted to the short and long term stability of the NaI detector, since the radiative capture cross sections are in the range from some μb/sr down to nb/sr and require long counting statistics, a condition for which any gain instability could even result in the total smearing out of kinematically defined peaks. Photomultiplier drifts and gain variations as a function of time and average anode current are long since known and are expected to be predominant with respect to electronic chain drifts and gain changes. We use therefore stabilized photomultiplier bases on the main crystal phototubes. We could also think of using a precision light pulser (e.g. model BNC 6010) to monitor inclusively the photomultipliers and the electronic chain against beam related instabilities. However radiative capture experiments run at tandem energies for test purpose are very little sensitive to gain stability effects, as will be clarified below.

3-2 Detectors Uniformity

Anticoincidence shield

The photomultipliers on the plastic annulus, and in particular the two on the same sector, can be tuned for equal gain making the comparison at the half height channel of a ^{137}Cs peak along the trailing edge. Tests were performed passing alternatively each of the PM anodes through a passive Mixer box, a Canberra 2020 amplifier and a Canberra 8080 MCA; 1 μs shaping time was selected for the amplifier. Before analyzing any result one has to consider that the energy calibration , the surface uniformity and instrumental resolution are not straightforwardly determined for the plastic sectors and disc because of the somewhat complex response function of such detectors to photons of energy around 1 MeV.

Due to the low Z and density of the absorption medium, the total absorption probability for the 0.662 MeV peak of ^{137}Cs and the 1.17 MeV and 1.33 MeV peaks of ^{60}Co is low compared to that of other possible interaction processes. This is easily understood

from the intrinsic response function whose prominent structure is due to the Compton edge and falls as $E_e = E_\gamma(1 + m_0c^2/2E_\gamma)$. The computed points of figure 2 were obtained from our computer code simulating the interaction of the primary photons with all interposed detection media [2] [3] [4]. In particular the example of figure 2 assumed an ideally collimated ($\Delta\vartheta = 0$) photon beam of 1.33 MeV. We see that the maximum of the response function is at an energy of 1.11 MeV, corresponding exactly to that of a backward Compton scattering, with the photon escaping without further interactions and the electron totally absorbed. At this energy the gross spectrum shows already an intrinsic FWHM of the order of 20%, which will necessarily be the lower limit of performance of any sector. The final FWHM value will also suffer, to a rather large extent, from the contribution of the source collimator and the statistics of light collection at the photocathode surface. Although the geometry of the annulus sectors cannot be given exactly as the input parameter for our code, nevertheless a reasonably good approximation of the detector and source collimators could be chosen to calculate the intrinsic spectra due to a ^{137}Cs and a ^{60}Co source (normalised sum of two peaks at 1.17 and 1.33 MeV) as given by the dotted histograms of figures 3a and 3b. A 20% statistical Gaussian convolution of these histograms produces the simulated final spectra of figures 3a and 3b (full lines) which closely match the experimental points (black dots).

We therefore conclude that although the measured FWHM for ^{137}Cs and ^{60}Co are of the order of 41-42%, only 20% comes from statistical resolution of the detectors while the rest must be attributed to intrinsic energy escape effects. Our 20% statistical value is in agreement with the 20% value reported for the nearest similar instrument [1] if we take this figure, in the absence of further details, as the statistical contribution to their spectra too.

The advantage of having a well simulated detector response can be extended to the evaluation of the total uniformity over the whole (annulus + disc) surface since the correct energy scale can now be attributed to the Cs and Co spectra. In particular half height channels correspond to 0.448 MeV and 0.951 MeV respectively. This gives a calibration line of the form

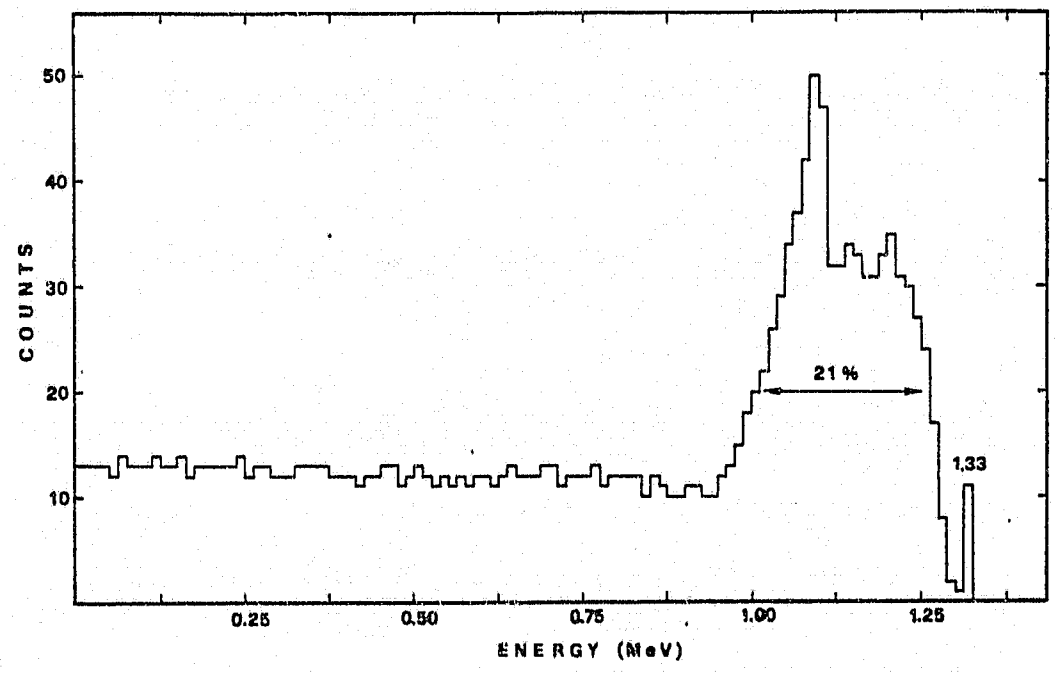

FIGURE 2 The computed spectrum resulting from the interaction of a 1.33 MeV ideally collimated γ-ray in the plastic annulus.

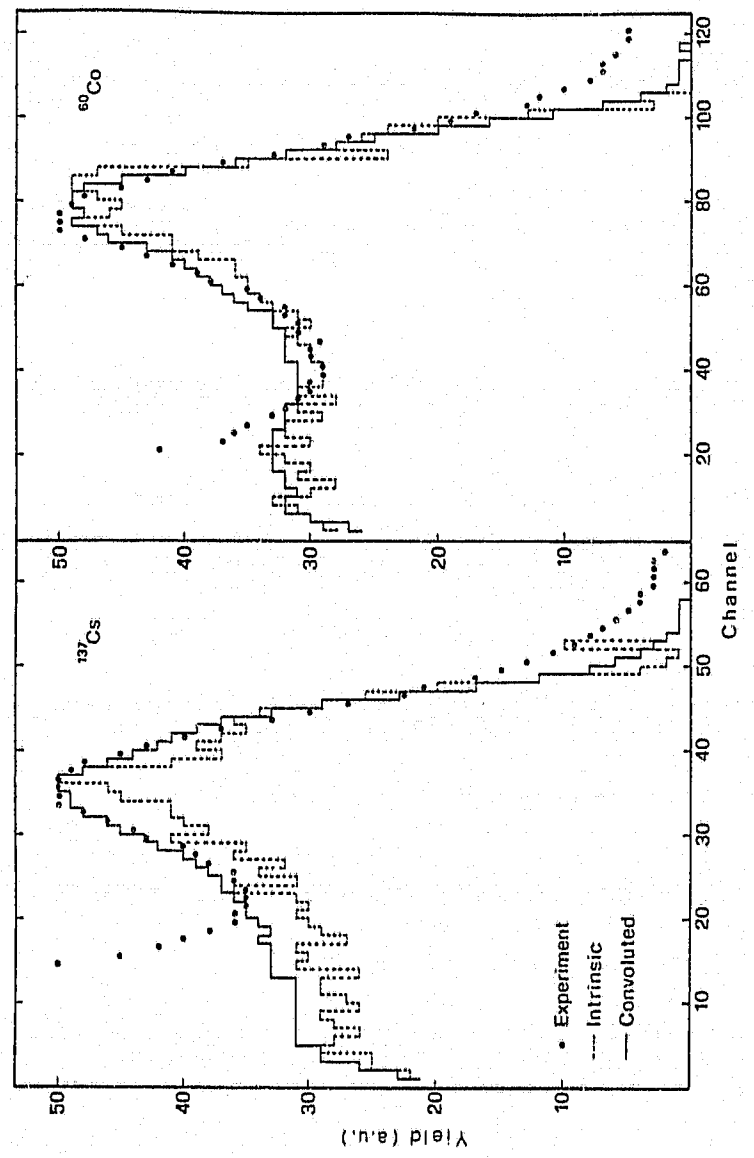

FIGURE 3 Computed, convoluted and experimental ^{137}Cs (part a) and ^{60}Co (part b) photon spectra in the annular detector.

$$E_\gamma(\mathrm{MeV}) = N_{chan} \times 0.00117 + 0.1176; \qquad [3-1]$$

which is perfectely compatible with an electronic chain expected to be quite free from extra biases. The disc was similarly tuned, positioning the source in the centre and imposing the same overall response of one of the annulus sectors with the three phototubes giving independently equal responses. In this way we could achieve an energy uniformity spread over the entire (annulus + disc) anticoincidence shield of 9.8% (figure 4a), when a collimated ^{137}Cs source was moved across 79 points of the shield inner surface. Similar results were obtained when the source was moved along the anticoincidence axis, perfectly in agreement with data previously reported for the BNL MKIII anticoincidence shield [1]. The total uncertainty with which the entire plastic shield will classify the energy deposited by a single event in the anticoincidence spectra is determined by statistical and non-uniformity contributions and will be therefore given by:

$$\frac{\Delta E}{E}(\%) = \sqrt{20^2 + 10.2^2} = 22.5\,\% \qquad \text{at } E_\gamma = 0.448\,\mathrm{MeV}; \qquad [3-2]$$

At energies approaching the "optimum" [5] threshold ($E_{th} = 100\,\mathrm{keV}$) we can assume that the uniformity spread contribution remains the same. The statistical contribution is generally found to have a $\Delta E/E = \alpha\sqrt{E}\,(\%)$ energy behaviour. This gives in our case ($\alpha = 29.9$ as computed from a 20% value at 0.448 MeV) an expected 30% statistical contribution at 100 keV for a total resolution of 31.6% or 32 keV, proving that in the present situation, we have basically reduced to unappreciable figures the possible size effects of the large anticoincidence shield upon the net resolution of escape events, which sets a remarkably good value for a shield of such a large surface.

NaI(Tl)-detector

Each of the seven NaI(Tl) phototubes was adjusted for the same gain when a collimated ^{60}Co source was positioned along the detector axis about 30 cm away from the front surface. As before the anode pulses were passed through a passive mixer box, a Canberra 2020 amplifier (shaping time constant 1 μs) and a Canberra 8180 MCA. Once the same high voltage bias was selected for all photomultipliers, only small dynode chain gain ad-

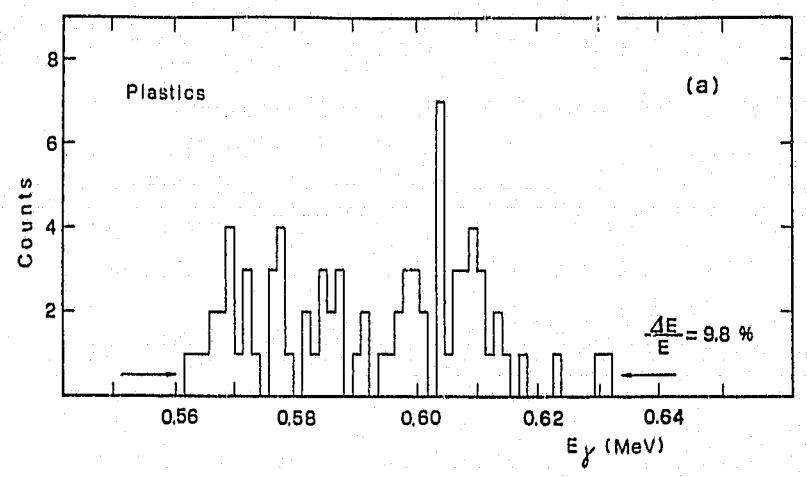

FIGURE 4 Measured energy uniformity for the anticoincidence (annulus + disc) shield (part a) and the NaI central crystal (part b).

justements were necessary, confirming that the photomultipliers had been factory selected for best uniformity. This type of tuning with a point-like source was found essentially equivalent to the tuning performed with volume distributed background radiation (e.g. ^{41}K), to which the NaI(Tl) was extremely sensitive. A collimated ^{60}Co was moved across 79 points of the lateral and front NaI(Tl) surfaces and the resulting overall uniformity spread was 1.78% at 1.17 MeV and 1.54% at 1.33 MeV as figure 4b shows. The seven anodes were then coupled to a 93 Ω system and processed by an Ortec 113 preamplifier and a Canberra 2010 Amplifier. A collimated source was positioned along the crystal axis 27 cm away from the front surface . The single crystal resolution for the ^{137}Cs line was 7.7% (figure 5a) and values for the two ^{60}Co lines were 5.9% and 5.3% respectively (figure 5b) when a shaping time of 1 μs was chosen. If we compare our results with those of reference [1] we see that both the ^{137}Cs resolution and the uniformity spread are slightly larger. This is expected to affect the resolution at 22 MeV but it has already been stressed that the higher the energy at which calibration is performed, the better the results at very high energy should be. On the other hand, if we compare our results with those of a crystal [5] mainly equivalent in size, but with less strict factory surface uniformity constraints, we can appreciate (figure 6) the improvement obtained.

3-3 A simplified electronic scheme for Tandem runs

Data handling is an important part of the experiment since most of the functions involved contribute significantly to the final resolution of the apparatus [5] and thus to the quality of the information extracted from the high energy photon spectra. The electronics system should be able to perform five basic functions: NaI(Tl)-plastics coincidence, pile-up rejection, linear analysis, $n - \gamma$ discrimination, and stability controls.

For the use at tandem energies, namely at the peak of the GDR in light nuclei, we devoted little attention to gain stabilisation since it was reputed to be relatively important, due to the short collection times required for the accumulation of a statistically significant high energy photon spectrum, on account of the rather large cross section values. Furthermore the extremely low count rate recorded when the Schonland Research Centre van de Graaff EN tandem beam pulsing (5 ns every 500 μs) was used, brought the cosmic

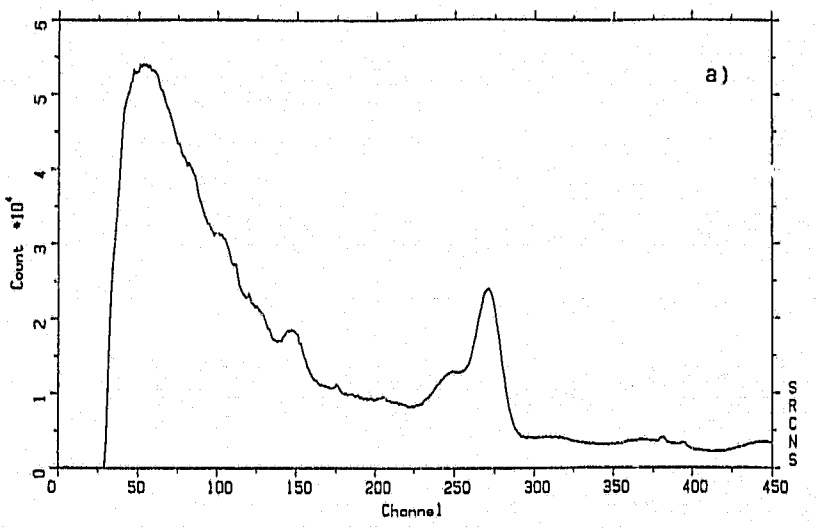

FIGURE 5 Single crystal energy photon spectra for a ^{137}Cs (part a) and a ^{60}Co source.

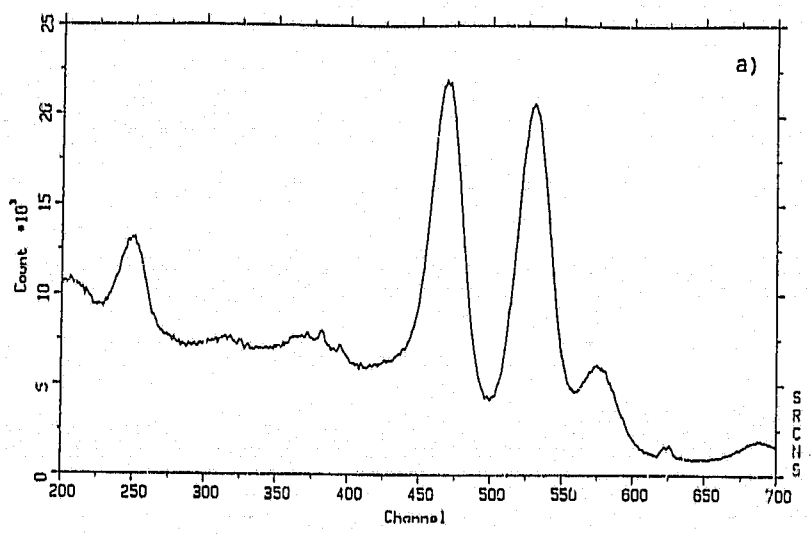

FIGURE 6 Single crystal ^{60}Co photon spectra in the case of a surface compensated (part a) detector and an equivalent size crystal (part b).

contribution to entirely dominate the recorded spectra making $n-\gamma$ discrimination totally ineffective. We thus developed a simplified version of the electronics system (figure 7), the final one being planned to follow closely the most relevant schemes reported in the literature. The functions we performed at this stage are three, namely:

i) *NaI(Tl)-plastics anticoincidence.* The anode pulses of both scintillators are summed after time compensation. NaI(Tl) PM's are equipped with ordinary passive high impedence bases and the anodes have to be summed (MIXER) over an high impedence to feed a preamplifier (Ortec 113). The plastics anodes are coupled (MIXER) to a 50 Ω load. Plastics anode pulses are processed in a conventional way through a timing filter amplifier (Ortec 474) and a constant fraction discriminator (Ortec 584). The same procedure, though not conventional, is adopted for the preamplifier output. A universal coincidence unit (Ortec 418A) detects escape events. Time compensation and pulse reshaping are performed by a gate and delay generator (Ortec 416A) and fast coincidence (Canberra 2144). The time resolution of this coincidence, as measured by a ^{60}Co source is reported in figure 8 and gives a result of 6.0 ns FWHM; this value can certainly be ascribed to the use of preamplifier output signals for timing but is still acceptable.

ii) *Pile-up rejection.* If E_{th} is the energy threshold in the NaI(Tl) crystal, the chain rejects events above E_{th} when piled- up with a pulse occurring either in the energy range $E \geq E_{th}$ or in the interval $E_{low} < E < E_{th}$. The value E_{low} has to be comparable to the energy resolution of the spectrometer to prevent peak broadening. The first rejection is provided by a pile-up inspector (Ortec 404A). The second is by a coincidence (Ortec 418A hl) between the NaI(Tl) timing pulse (Ortec 584 eh) that has already selected the anticoincidence function, and a second pulse generated in the following way. A constant fraction discriminator (Ortec 584 el) provides pulses at energies above E_{low}. But it is anti-gated by any pulse corresponding to energies above E_{th} generated by a (already mentioned) constant fraction discriminator (Ortec 584 eh). Events above E_{th} will trigger the constant fraction discriminator (Ortec 584 el) but at the same time will antigate it. Events between E_{low} and E_{th} only will trigger the CFD. Time compensation is provided by a gate and delay generator (Ortec 416A)

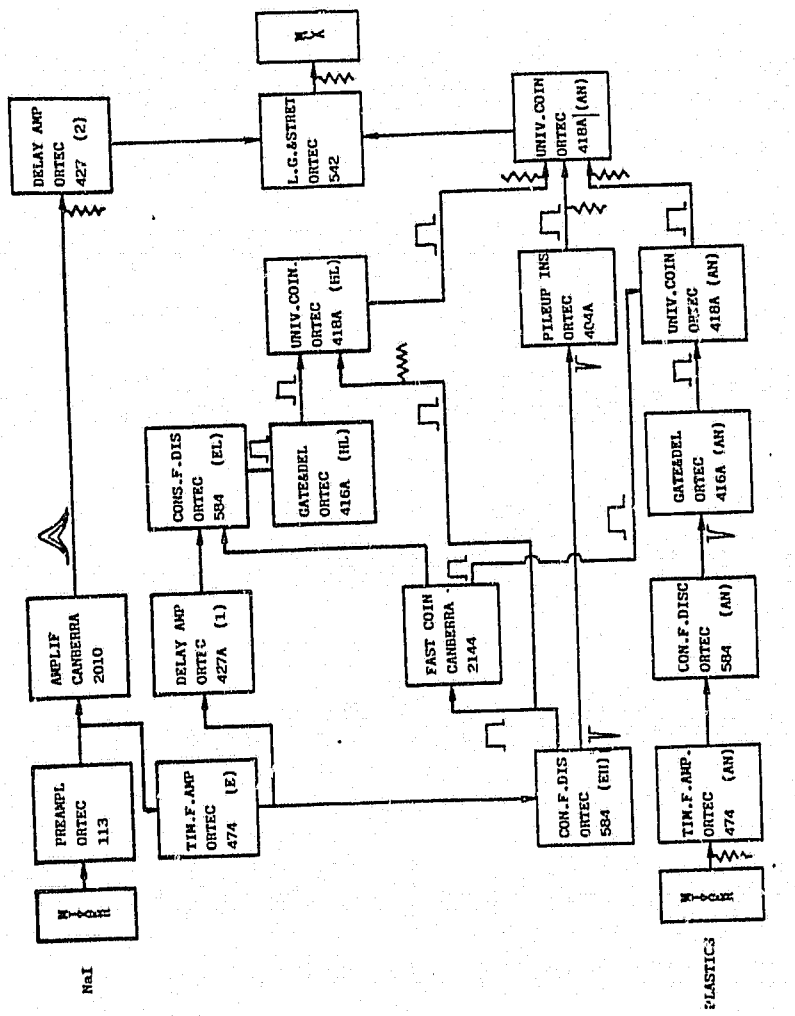

FIGURE 7 The scheme of the simplified electronic set-up.

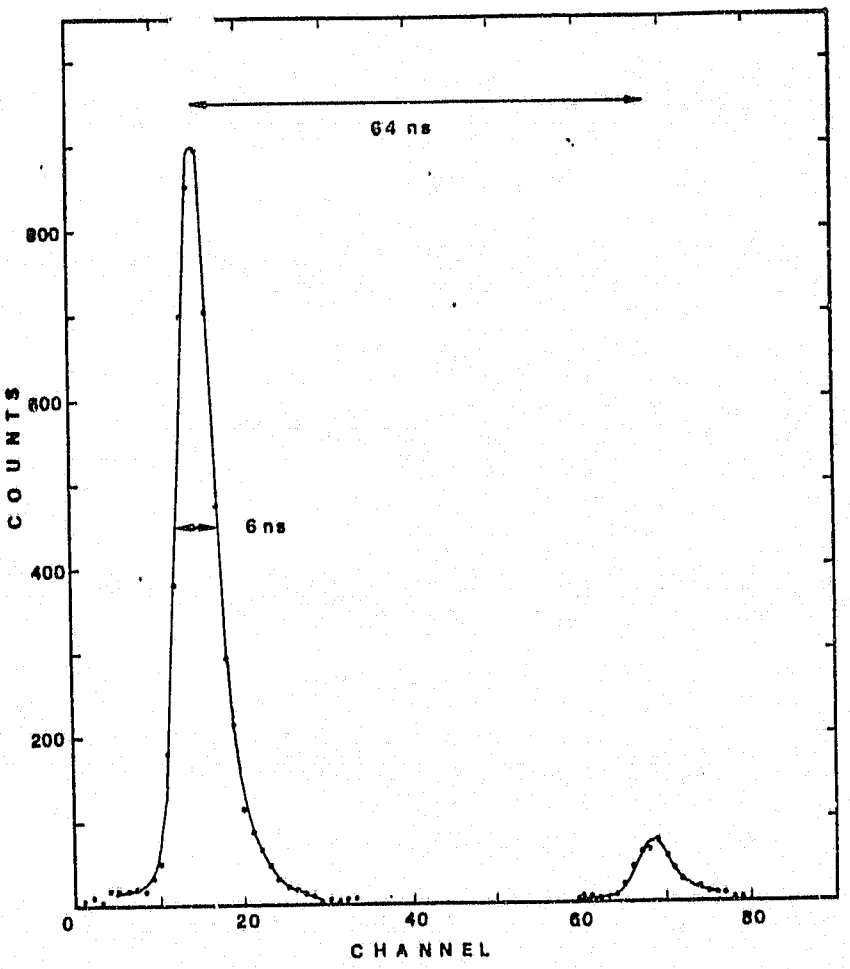

FIGURE 8 Time resolution of the anticoincidence set up as in the conditions of figure 7.

and a delay amplifier (Ortec 427A).

iii) *Linear analysis.* Linear analysis is performed by a preamplifier (Ortec 113) and an amplifier (Canberra 2010) through a linear gate and stretcher (Ortec 542) that is anti-gated by the OR sum (Ortec 418A all) of the two possible pile-up events and the anti-coincidence signal. Time compensation is achieved by a delay amplifier (Ortec 427). The electronics system did not provide gain stability nor dit it provide $n-\gamma$ discrimination. The results achievable by this simplified chain are already appreciable in the anti-coincidence spectrum of a ^{60}Co source positioned in front of the scintillators (figure 9). The FWHM resolution of the two peaks is in fact 5.7% (1.17 MeV) and 5.3% (1.33 MeV).

3-4 Tandem tests at GDR energies

Despite the simplified electronics system we have run successfully the reaction $^{11}B(p,\gamma)^{12}C$ at $E_p = 7$ MeV on a 250 μg/cm^2 natural boron target with the detector at 90 degrees and 120 cm away from target. The result is seen in figure 10. The anti-coincidence threshold was set at a nominal value of 40 keV; the energy threshold for the NaI(Tl) logics was set at 9 MeV and the NaI(Tl) lower threshold for pile-up rejection was set at 0.5 MeV. In our experimental conditions the rate above 9 MeV was 40 Hz and the plastics count rate was 40 kHz. The overall pile-up rejection was around 9% while the collection efficiency at 22 MeV was measured from the spectra in figure 10 at 46.6% against a 43% value computed in the design stage [4].

These conditions ensured an energy resolution of 2.35% FWHM and 8.0% FW$\frac{1}{10}$M for the (p,γ_0) line at 22.38 MeV. The values compare favourably with the best in the literature [1] and the fact that they are slightly larger than those can be with no doubt attributed to the absence of $n-\gamma$ discrimination and to the effects of tuning not at the best (6.13 MeV) energy, with some possible little effects still coming from the absence of short and long term stabilisation.

3-5 Experimental Set-up at the NAC Cyclotron

The Hagar spectrometer is positioned along beam line "F" inside the southern ex-

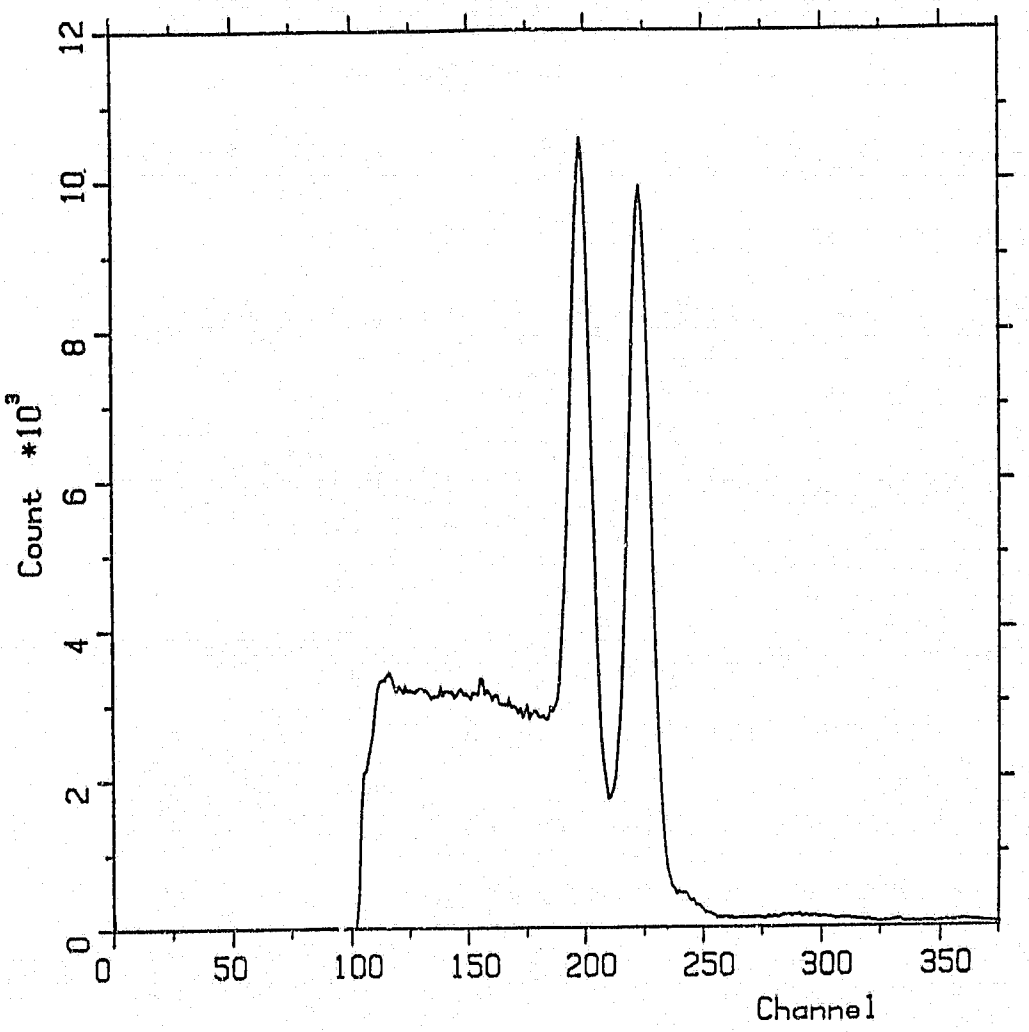

FIGURE 9 A ^{60}Co photon spectrum in the anticoincidence scintillators configuration.

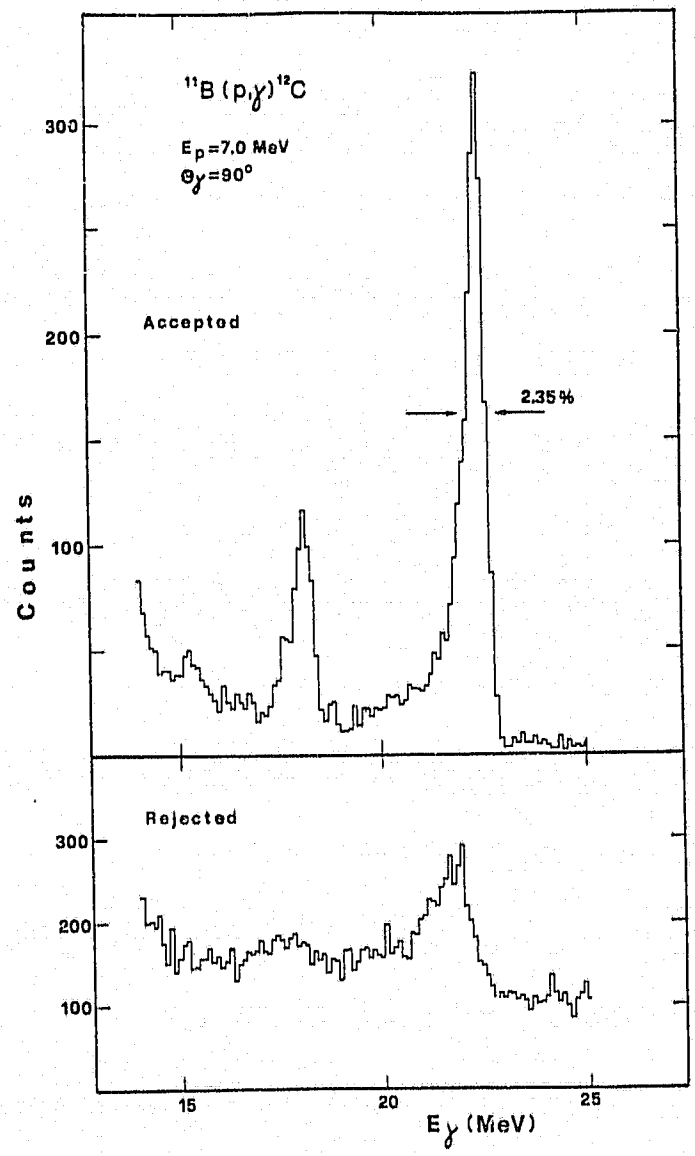

FIGURE 10 The accepted and rejected photon spectra from the reaction $^{11}B(p,\gamma)^{12}C$ at $E_p = 7.0$ MeV as measured by the complete detector set up positioned at 90 deg to the beam line.

perimental hall of the National Accelerator Centre (see figure 11). The entire apparatus, consisting of the three detectors, the lead shields, borated paraffin bricks and part of the photomultipliers power supply, is placed on a rotating platform covering angles from 30 to 148 deg. The platform movement is provided by four air pads which ensure easy mobility of such a heavy apparatus while guaranteeing a position reproducibility within parts of a millimeter both in height and distance. The NaI(Tl) crystal rotates at exactly 120 cm from the target centre. The scattering chamber consists of a parallelepipedal frame (dimensions $12 \times 12 \times 50\,cm^3$), connected to the standard 5" Ø beam pipe. The lateral sides of the chamber have perspex windows to allow the use of TV cameras for beam focusing and to reduce to a minimum the photon absorption by the chamber walls. A four-position target ladder is provided for solid targets and there is also the facility of installing a gas target consisting of a thin aluminium cylinder (Ø40 mm, length 440 mm), with mylar entrance and exit windows, that can be pressurized to a maximum of 3 atm. The beam catcher consists of a 25 cm thick aluminium cylinder. This is located inside the bunker walls at about 320 cm from the target, being shielded, apart from the 1 m concrete wall, by 10 cm of lead all around the Faraday cup. We have also added a positionable wall of borated wax bricks and additional iron slabs around the beam pipe in the proximity of the bunker wall, to prevent backscattered neutrons from reaching the detector at limit detection angles.

3-6 Electronics

The electronics system (figure 12) has been extended largely to meet the more stringent experimental conditions and the necessity of collecting the widest possible set of information during the on-line data acquisition. While the general philosophy of the electronics set-up remains the one explained in section 3-3, the numerous additions must be described in detail.

a) *Photomultiplier stabilization*

We have already indicated that possible ways of improving the overall detector stability are the use of stabilized photomultiplier bases and to introduce a computer controlled calibration. New photomultiplier bases, with diode controlled voltage steps for the last dynodes have been adopted (figure 13). The performance of such PM

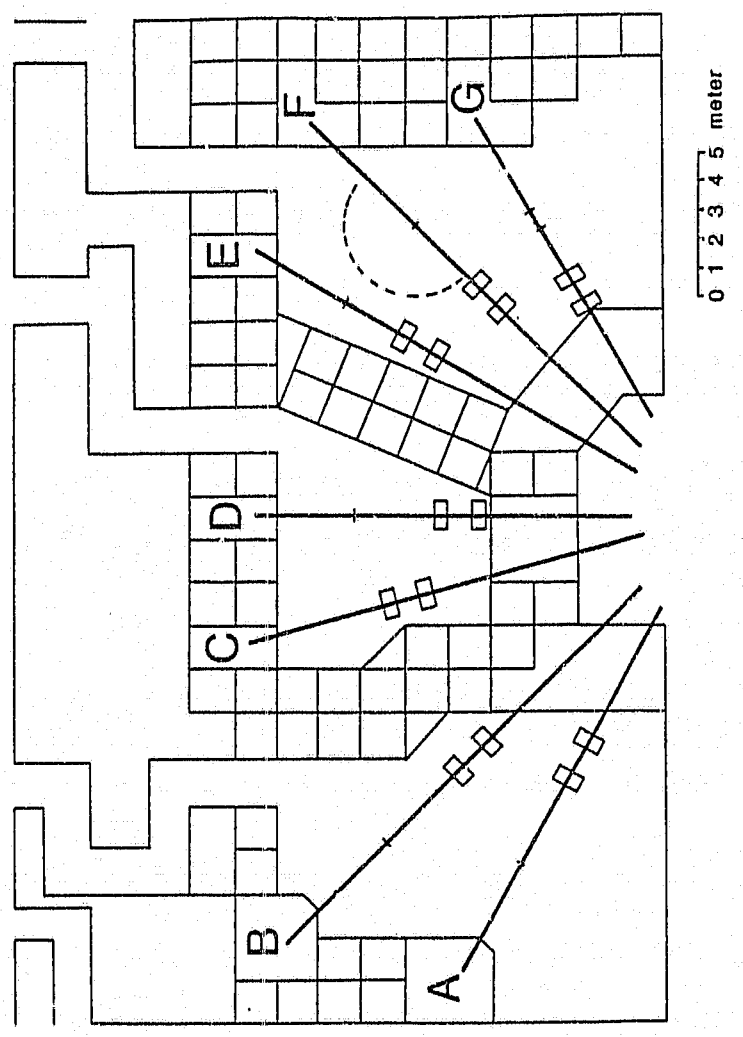

FIGURE 11 Layout of the NAC experimental area with Hagar position indicated by the dashed semicircle around line F.

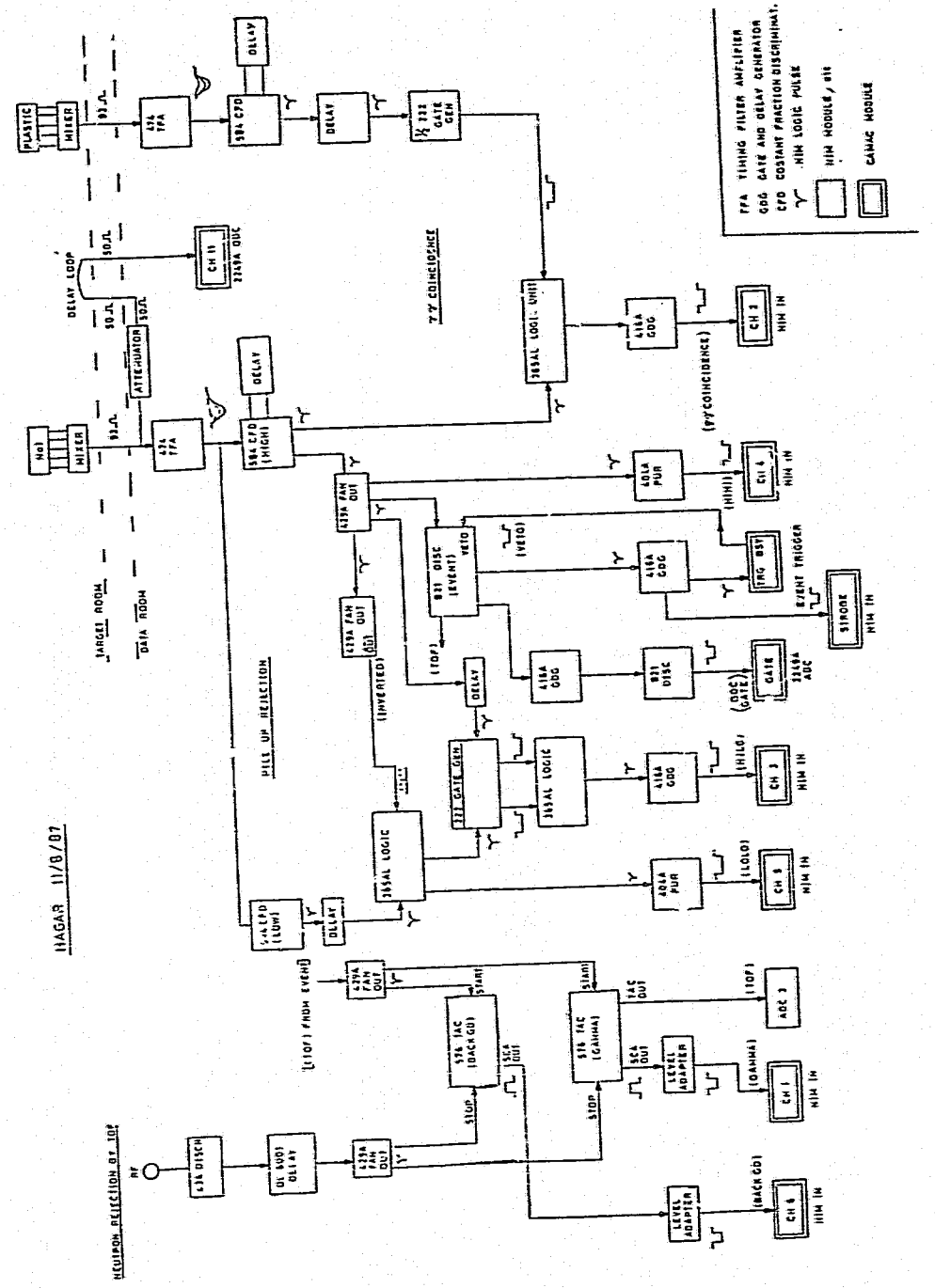

HAGAR 11/8/82

FIGURE 12 The electronic scheme adopted in cyclotron experimental runs.

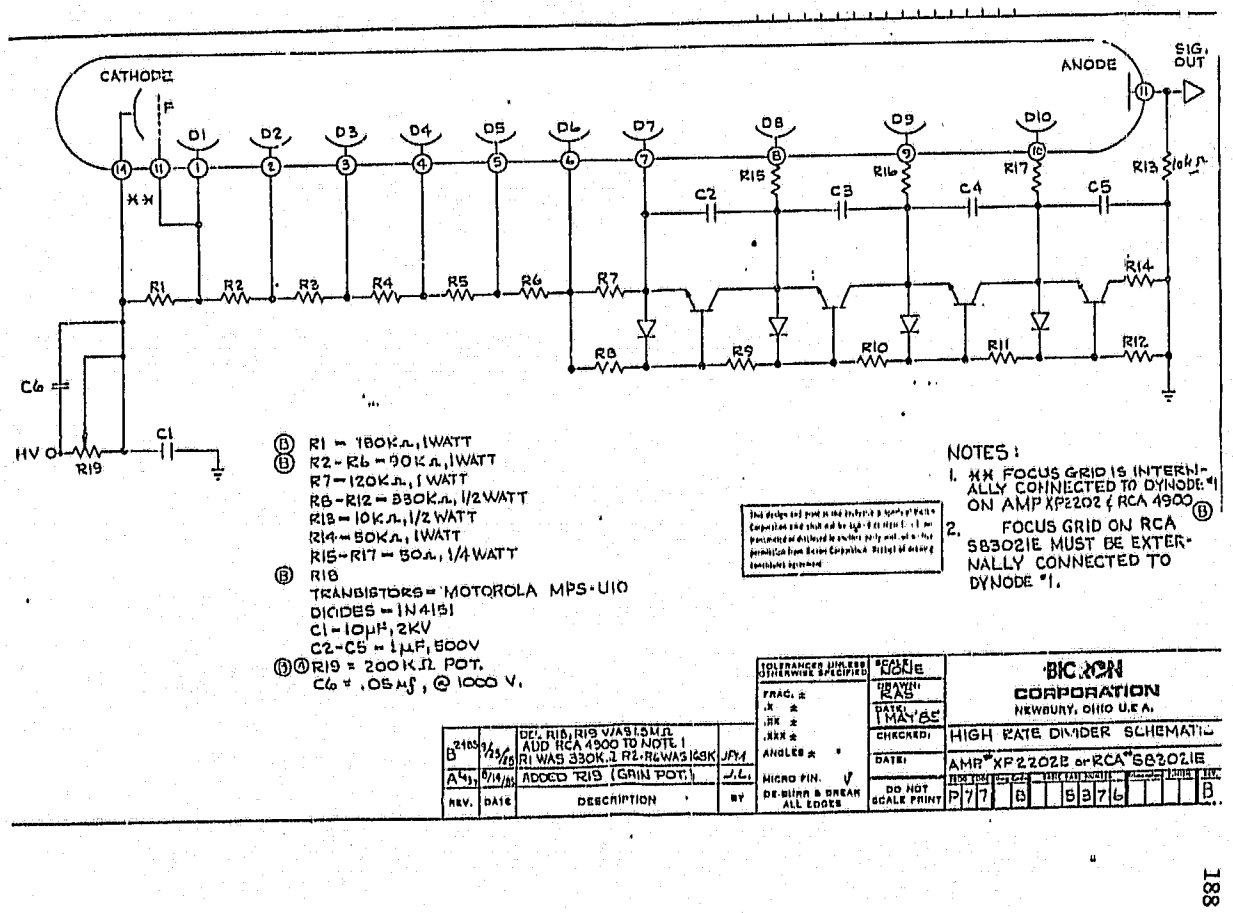

FIGURE 13 Active photomultiplier bases installed on the seven NaI photomultipliers for best stability.

bases has been thoroughly investigated [6] and the effective result is in giving constant PM gain from a few kHz up to about 2 MHz of real particle events. The NAC beam stability, in energy and position, was particularly good in all the accelerator runs; therefore the implementation of a computer controlled calibration set, though designed, could be postponed without any inconvenience as the data presentation will show.

b) *Pulse handling*

We have decided to reduce to a minimum the number of pulses traveling from the target room to the data room. This was achieved by summing in a resistive mixer both the 7 NaI(Tl) and the 15 plastic scintillator anode pulses. Only the two sum pulses were then transmitted through a 93 Ω coaxial cable to the data room for the complete logic and linear analysis.

c) *Linear Analysis*

Only the NaI(Tl) pulse was prepared for linear analysis. It was picked from the output of the mixer box, then attenuated to match the gain conditions of the Digital Converter and delayed through a 50 Ω delay loop to make the anode pulse coincident with the gate pulse at the input of the LeCroy 2249A Camac QDC.

d) *NaI(Tl) Trigger Pulse*

The most important logic function in this chain has to be the trigger pulse generated by any event that corresponds to an energy release above a fixed threshold (14 MeV usually) in the Sodium Iodide crystal. For this the anode sum pulse is reshaped and amplified by an Ortec 474 Timing Filter Amplifier. Then a fast NIM logic pulse is provided by an Ortec 584 (High) Constant Fraction Discriminator and subsequently split, by a couple of Lecroy 429A Linear Fan Out's. The setting conditions for the electronic boxes are as follows:

MIXER Output	$t_r \approx 80$ ns	$t_d \approx 600$ ns	$V_E \approx 3$ mV/MeV		
474 TFA Setting	Gain 6 × 7.9	Int 20 ns	Diff 20 ns	PZ adj	NonInv
474 TFA Output	$t_r \approx 120$ ns	$t_d \approx 280$ ns	$V_E \approx 50$ mV/MeV		
584 CFD(HI) setting	Shap.Del. 79.5 ns	Block Time 30 ns			

t_r = Rise Time t_d = Duration V_E = Pulse Height

e) *Anti-coincidence Veto Pulse*

The escape of part of the shower energy from the NaI(Tl) crystal boundaries is detected by a coincidence between the NaI(Tl) logic pulse and a signal from the plastic scintillator annulus or disc. The anode sum pulse from the plastic shield is processed similarly to the NaI(Tl) pulse. It is amplified and reshaped by a 474 TFA and a logic trigger is provided by a 584 CFD. This fast NIM logic pulse is delayed,to insure adequate coincidence conditions, by a passive delay box and reshaped by a LeCroy 222 Gate Generator to fix (by the width of the 222 output) the resolving time of a LeCroy 365A Logic Unit. The coincidence output, indicating an escape event is processed by a Ortec 416A Gate and Delay Generator to be acceptable at the right timing by a Nim-In Camac module that will record anti-coincidence events. Settings and pulse shapes were as follows:

MIXER Output	$t_r \approx 10\,\text{ns}$	$t_d \approx 35\,\text{ns}$	$V_E \approx 30\,\text{mV/MeV}$		
474 TFA Setting	Gain 20×6.2	Int 20 ns	Diff 20 ns	PZ adj	NonInv
474 TFA Output	$t_r \approx 30\,\text{ns}$	$t_d \approx 105\,\text{ns}$	$V_E \approx 500\,\text{mV/MeV}$		
584 CFD setting	Shap.Del. 32 ns	Block.Time 30 ns			
Passive delay	104 ns				
222 GG	Neg NIM out	$t_d \approx 100\,\text{ns}$			
416A GDG	Neg NIM out	$t_d \approx 500\,\text{ns}$			

Time spectra were recorded at different times and with different threshold settings. For low thresholds (^{60}Co) the FWHM of the time spectra were about 7 ns and we recorded about 40 ns at baseline. These figures improved when we restricted the dynamical range of the discriminators i.e. in proton capture running conditions. For threshold settings like 200 keV (plastic) and 14 MeV (NaI(Tl)) the TAC spectrum of the anti-coincidence is reported in figure 14 and shows a peak of 4.5 ns FWHM and

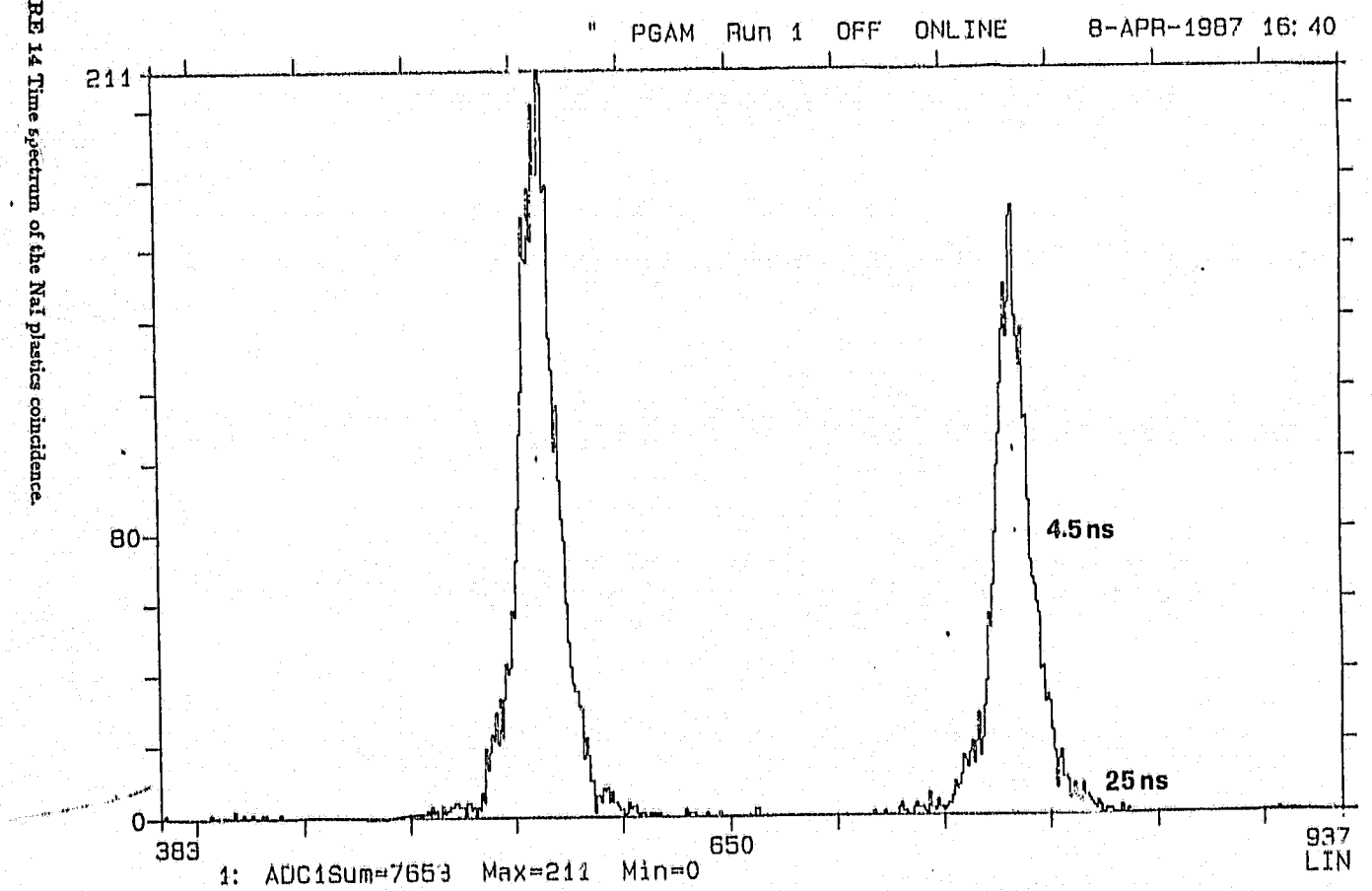

FIGURE 14 Time spectrum of the NaI plastics coincidence.

25 ns at baseline.

f) *Neutron-gamma Time-of-Flight Discrimination*

The cyclotron radiofrequency (RF) pulse is used to provide a time reference for the measurement of time-of-flight performed over the path length of 120 cm that separates the target from the front surface of the NaI(Tl) detector. In such a path length the travel times of photons (3.3 ns/m) and of energetic neutrons (e.g. 11.79 ns/m at E_{kin} = 40 MeV) are perfectly distinguishable. The RF signal has for example frequencies of 12 MHz (period 83 ns) at 25 MeV, of 16.4 MHz (61 ns) at 66 MeV and of 26 MHz (38.5 ns) at 200 MeV so that the time difference between subsequent beam bursts is adequate to reject target-born fast neutrons against gammas. The RF signal is passed through an Ortec 436 100 MHz Discriminator to be converted into a sequence of standard NIM fast logic pulses. These are delayed ($\Delta T = 50$ ns), split by a LeCroy 429A Fan Out and sent to the stop input of two identical Ortec 547 Time-to-Amplitude Converters. The start pulses to the TAC's come from the NaI(Tl) event trigger and for this to remain within the operation range of the TAC's, it is limited to 1 MHz rates. The conversion range is selected to be 50 ns and proved to be convenient at all beam energies. A typical spectrum is shown in figure 15 and we see how neat the identification and separation of the 1.5 ns FWHM photon peak is from the cosmic constant background and the large neutron bump. It has to be noted that TAC spectra may differ in relative time as a result of beam focus changes and it is therefore necessary to monitor them at any time an operation is performed on the beam adjustment parameters. The advantage of having a double TAC chain is that we are capable of setting time windows around different portions of the time spectrum to examine the gamma events as well as the contribution to the inclusive NaI(Tl) energy spectra from different background regions. After level adjustment the single channel outputs of the TAC's are sent to a Camac NIM-IN while the linear outputs are sent to a Camac ADC for conversion and storage.

g) *Event Logic Trigger*

We have already explained how we produce a NIM fast logic pulse for any event above an energy threshold in the sodium iodide as set by the Ortec 584 CFD ("High" in

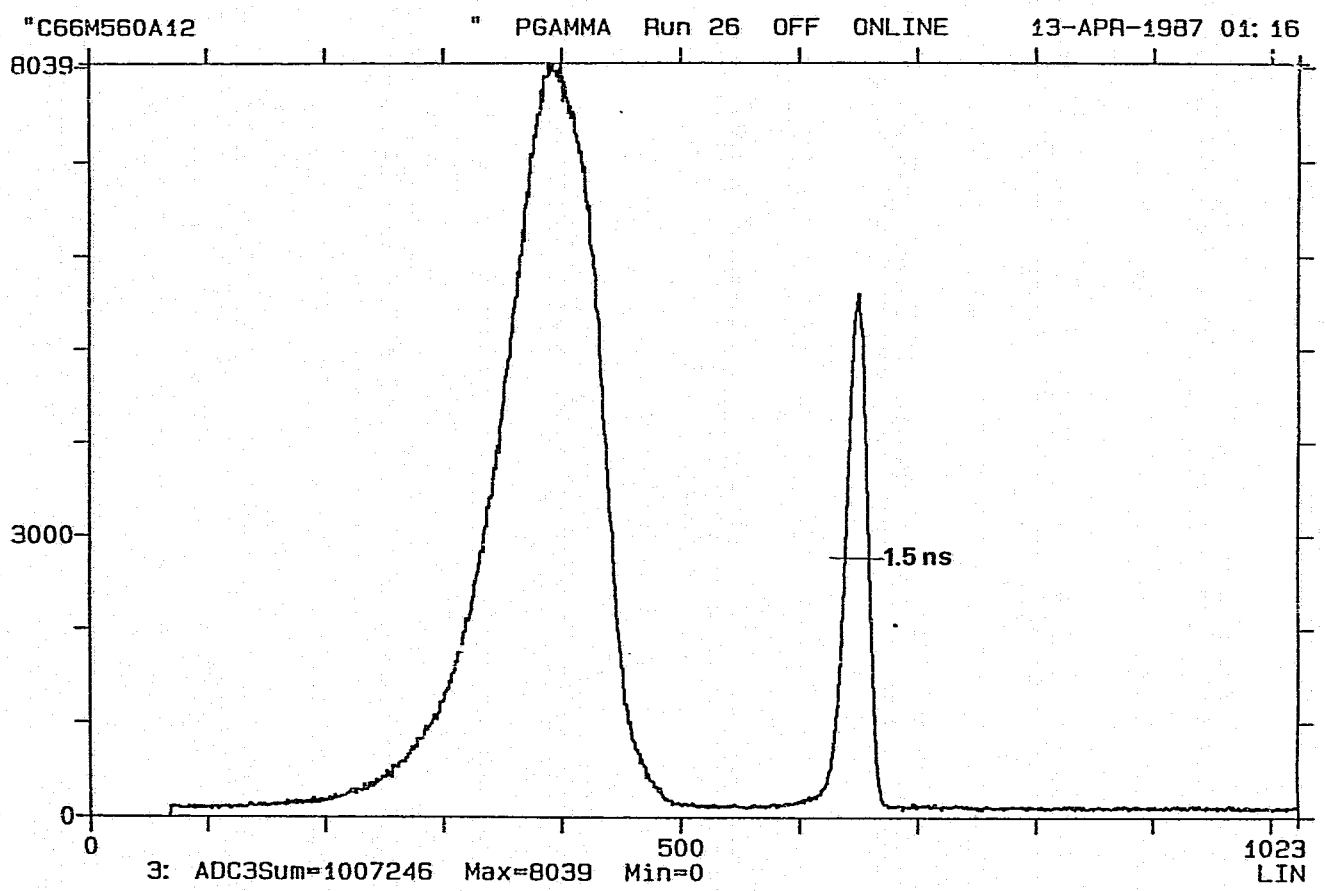

FIGURE 15 Time of flight spectrum for the reaction products with the constant background due to random cosmic start or stop signals.

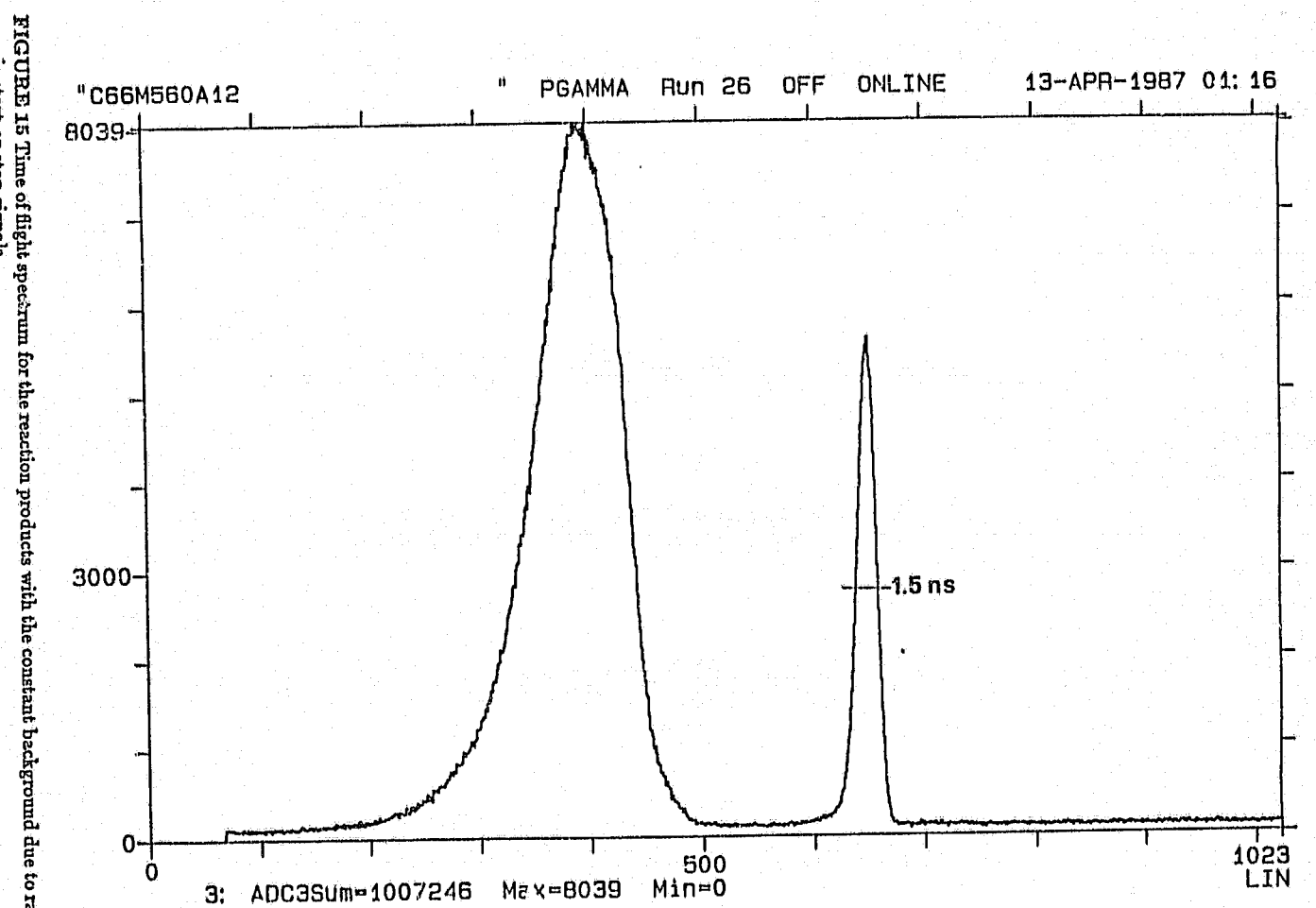

FIGURE 15 Time of flight spectrum for the reaction products with the constant background due to random cosmic start or stop signals.

figure 12). The same pulse is used to provide a gate for the Charge to Digital Converter that generates the linear spectra of selected events and also the necessary trigger and strobe pulses to drive the Camac cycle on the VAX 11/730 on-line computer. To do so the CFD Fast-NIM pulse is fed into a Lecroy 821 discriminator whose Fast-NIM outputs are delayed by means of two Ortec 416A Gate & Delay Generators. One generates a Fast-NIM logic pulse as a trigger for the Camac cycle and a negative NIM 300 ns wide strobe pulse. During the time a Camac cycle is taking place a veto pulse is given by the Camac Busy Output to prevent multiple triggering. The second G&DG is coupled to another LeCroy 821 discriminator to generate at the correct time a gate pulse for the QCD, the coupling being imposed by the large width of the 416A outputs, inadequate to the needed 116 ns wide gate for our anode NaI(Tl) pulses.

h) *Pile-up Rejecton*

The electronics system provides information about the pile-up of two pulses both above the NaI(Tl) threshold (14 MeV);of two pulses both within a lower energy range (100 keV $< E <$ 14 MeV) and finally of two pulses of which one is above the NaI(Tl) threshold and the other is within the lower energy window. The LO-LO and HI-HI discrimination is achieved by the use of two equal Ortec 404A Pile Up rejectors with resolving times of 2 μs whose outputs are sent as usual to a Camac Nim In.

The scope of the HI-HI pile up check is to take account of those events that are removed from the actual spectral peaks towards very high energies while the scope of the LO-LO pile-up check is to prevent two small pulses from adding in the lower end of the accepted spectra in the vicinity of the 14 MeV threshold although the number of these events is usually very low. More complex is the LO-HI logic. We want in fact a pulse from those events included in an energy range between the threshold of the 584 CFD (Low) and that of the 584 CFD (High) without the need of any resetting apart from that of the 584 CFD (High) threshold according to the experimental needs. This is obtained by processing the HI fast NIM pulse by a 429A Fan Out that produces a OUTneg signal a few ns wide. Delaying the 584 CFD (low) Fast-NIM pulse generates a superposition of the two pulses in case of coincidence and therefore no output is produced at the 365AL logic unit where the sum of the two

pulses will be constantly above the zero level in this circumstance. This will normally be true for pulses that are above the 584 CFD (high) threshold and obviously above the 584 CFD (low) threshold as well. For pulses within the window only the 584 CFD (low) discriminator will trigger and the superposition of pulses at the 365AL logic unit will consist only of a negative NIM pulse that will generate an output. This LO output and the HI output will feed the two halves of a 222 Delay Generator to be reshaped at about 600 ns i.e. to approximately the width of the NaI(Tl) anode pulses fed to the 2249A QDC. The stretched logic pulses will be analysed by a 365AL logic unit that will generate an output any time a HI pulse is preceded or followed (within 600 ns) by a LO pulse. The coincidence output is as usual reshaped by a 416A GDG for use in a Camac Nim-In module.

l) *Time relation between pulses*

The time requirements are that the trigger event precedes any other pulse to be analysed during the Camac cycle and that any of the logic pulse provided (TOF, HI-LO etc.) is superimposed to some extent on the Strobe pulse . The time relation between pulses is reported in figure 16 where the reference time is given by the trigger pulse.

l) *Scalers*

Three Camac scalers are used. Two see the event trigger but one of them is also sensitive to the veto pulse to inhibit counting while the system is dead. In this way we have an indication of the dead time of our data acquisition system. The third scaler monitors the pulses from the current integrator and we can store and display the accumulated charge.

m) *Data Sorting*

During an acquisition run a few memory areas are filled with experimental information and subsequently dumped on disk for further analysis. The data processing and storage is organized as in figure 17, the different areas corresponding to

TOF	TAC linear spectrum
RAW	Unprocessed NaI(Tl) linear spectrum
ACCEPT4	NaI(Tl) linear spectrum: all rejections included

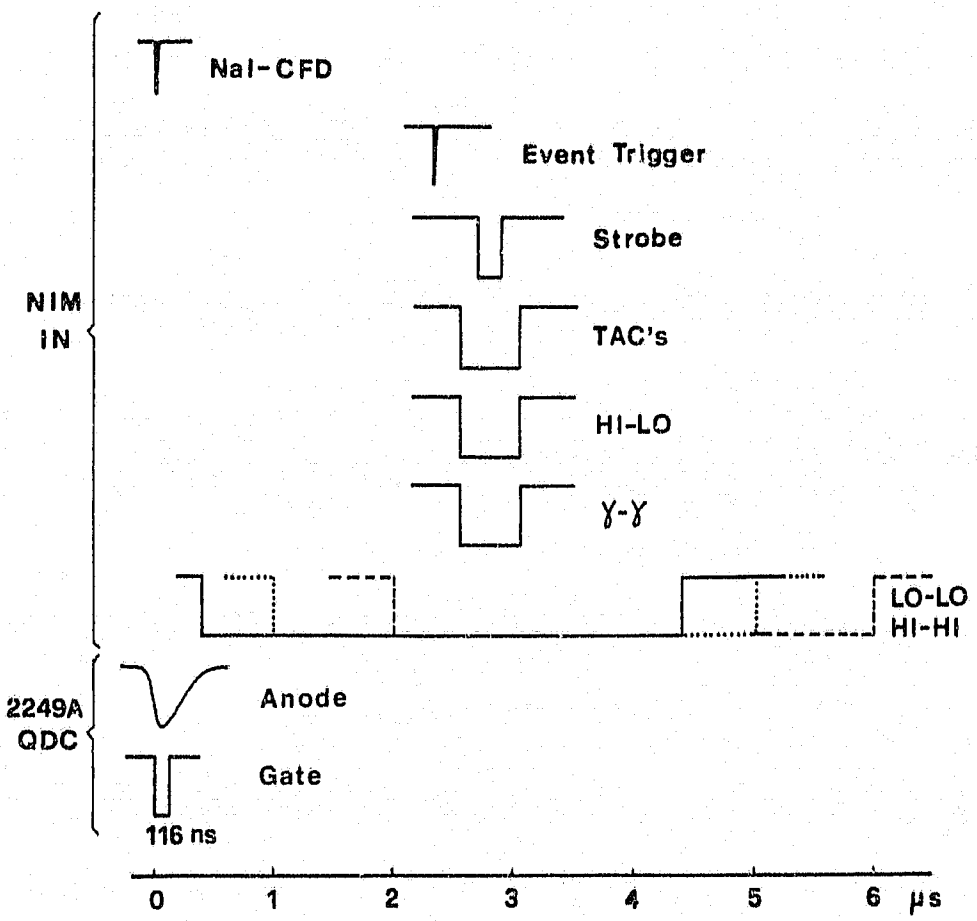

FIGURE 16 Time relation between pulses inside a CAMAC cycle.

```
Run number =  C4960224
Area  Name    Type      X-size  Y-size  #Pages  Len(LW)     Data-sum
  1   TOF     I*4   1D    1024    1       8      1024   4.099870E+05
  2   ZAM     I*4   1D    1024    1       3      1024   1.593154E+06
  3   ACCEPT4 I*4   1D    1024    1       1      1024   1.713140E+05
  4   AVTICD4 I*4   1D    1024    1       1      1024   6.068900E+04
  5   HILD4   I*4   1D    1024    1       1      1024   5.376900E+04
  6   MINI4   I*4   1D    1024    1       1      1024   4.481000E+03
  7   LOLD4   I*4   1D    1024    1       1      1024   1.003000E+04
  8   REJECT4 I*4   1D    1024    1       1      1024   2.379840E+05
  9   ROUTE   I*4   1D    128     1       1       128   1.593184E+06
 10   TOFPK   I*4   1D    1024    1       1      1024   4.092970E+05
 11   TOFSS   I*4   1D    1024    1       1      1024   1.179210E+05
 12   BACKSD  I*4   1D    1024    1       1      1024   2.674000E+04
 13   WORK    R*4   1D    1024    1       1      1024   0.000000E+00
 14   SCALERS_SCAL  I*4   40      1       1        40   9.043525E+06
 2990 ID_GATES GATE I*4     2    256      1       512  -5.160030E+02
 3400 DSA_AREA CIRC REAL*4 64     1      1       640
 3500 PGAMMA   FILL I*4   256     1      7       896   2.813310E+11
Total of  17 data area(s)      11* pages.
```

FIGURE 17 An example of computer output list showing for a given run (C4960224) the memory occupation and organization.

ANTICO4	NaI(Tl) linear spectrum: $\gamma - \gamma$ coincidences rejected
HILO4	NaI(Tl) linear spectrum: HI-LO pile up rejected
HIHI4	NaI(Tl) linear spectrum: HI-HI pile up rejected
LOLO4	NaI(Tl) linear spectrum: LO-LO pile up rejected
REJECT4	Linear spectrum of all rejected NaI(Tl) pulses
ROUTE	Log of all logic pulses collected
TOFPK	NaI(Tl) spectrum as triggered by TAC pulses in the γ peak
TOFBG	NaI(Tl) spectrum as triggered by TAC pulses out of the γ peak
WORK	A working area
Scalers	The account of scalers: collected charge is in position 35
1D Gates	
DSA AREA	Displays
PGAMMA	Initialisation

3-7 Detector resolution at high energies

We have already discussed in detail what kind of performance one can get from Hagar when this is operated in almost optimum conditions as concerns target thickness, count rate,collection time, target choice, background and so on. All these requirements were met at the Wits Tandem and gave a resolution value of 2.35% at $E_\gamma = 22.38\,\mathrm{MeV}$ in very good agreement with the values recorded by similar spectrometers. We know that the performance of high energy spectrometers [1] is such that FWHM resolutions of 2.0% at 50 MeV are achieved, if the same optimum conditions are maintained. We have had to decide not to carry on any particular experimental run dedicated to the exploration of the ultimate performance limits of our detector, so as to dedicate the largest portion of the available beam time to the completion of the experimental program [7]on radiative capture by Carbon at excitation energies around $2\hbar\omega$ in ^{13}N. This decision was supported by three main arguments. The first concerned the limited availability of continuous beam time in view of the forthcoming daily medical operation of the cyclotron, which would have as a matter of fact forbidden any complete angular distribution measurement without the necessary and time consuming intercalibration of partial runs. The second concerned the

fact that, as we already observed, extreme resolution values are achieved only at the price of a substantially reduced collection efficiency with consequent much longer collection times per single statistically significant spectrum, not to mention the difficulties related to a more complex electronics tuning. As we shall see in the forthcoming data, the standard resolution values that we had on our spectra were perfectly adequate to allow the separation of prominent structures in the investigated reaction. The third reason was that the detector had proved its reliability at low energies and since it is constructed following exactly the same criteria and employing the same techniques as others, there is no reason to doubt that the same performances, under the same conditions, can be achieved.

It is, however, important to give some examples of standard Hagar performance at high energies. First we show in figure 18 a comparison of raw and accepted spectra. The improvement introduced by the various gates imposed on the linear pulses is evident here and it can also be remarked that the collection efficiency worked out from this figure (38.3%) is in very good agreement with that computed by our code (35%) as the efficiency value at 22.38 MeV. As concerns energy resolution, we can look at figures 19 and 20 for photon peaks at 15.11 MeV, at 38.4 MeV, at 43.72 MeV and 45.93 MeV respectively, and at figure 21 for the behaviour of FWHM resolution with peak energy. All quoted values are extracted from spectra taken at high currents (20-40 nA) on thick target (36.6 mg/cm^2) with no subtraction of any background.

3-8 Summary

The design criteria for this anti-coincidence large-volume scintillation spectrometer were maximal uniformity of response over the entire scintillation volume, an energy resolution close to 2% over the range of energies spanning from 20 to about 50 MeV and the possibility of flexible treatment of logical and analog information from the detector. From the data presented in this chapter it is evident that even at this early stage of implementation Hagar has in practice met all the design objectives, and matched the performance of the best detectors ofthis type.

As far as uniformity criteria are concerned, both the NaI(Tl) crystal and the complete plastic anti-coincidence shield(s) can be tuned to such a degree of equalization that the

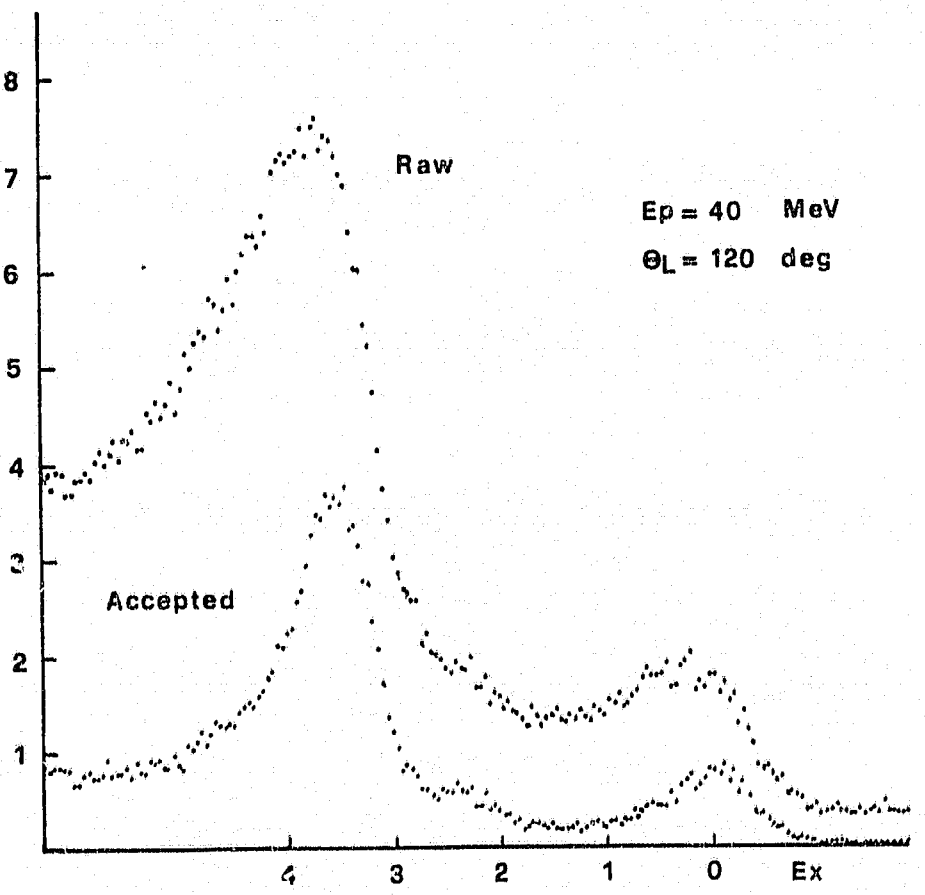

FIGURE 18 A comparison of Raw and Accepted gamma spectra taken at $E_p = 40$ MeV and $\theta_\gamma = 120$ deg. The anticoincidence threshold was set at 200 keV.

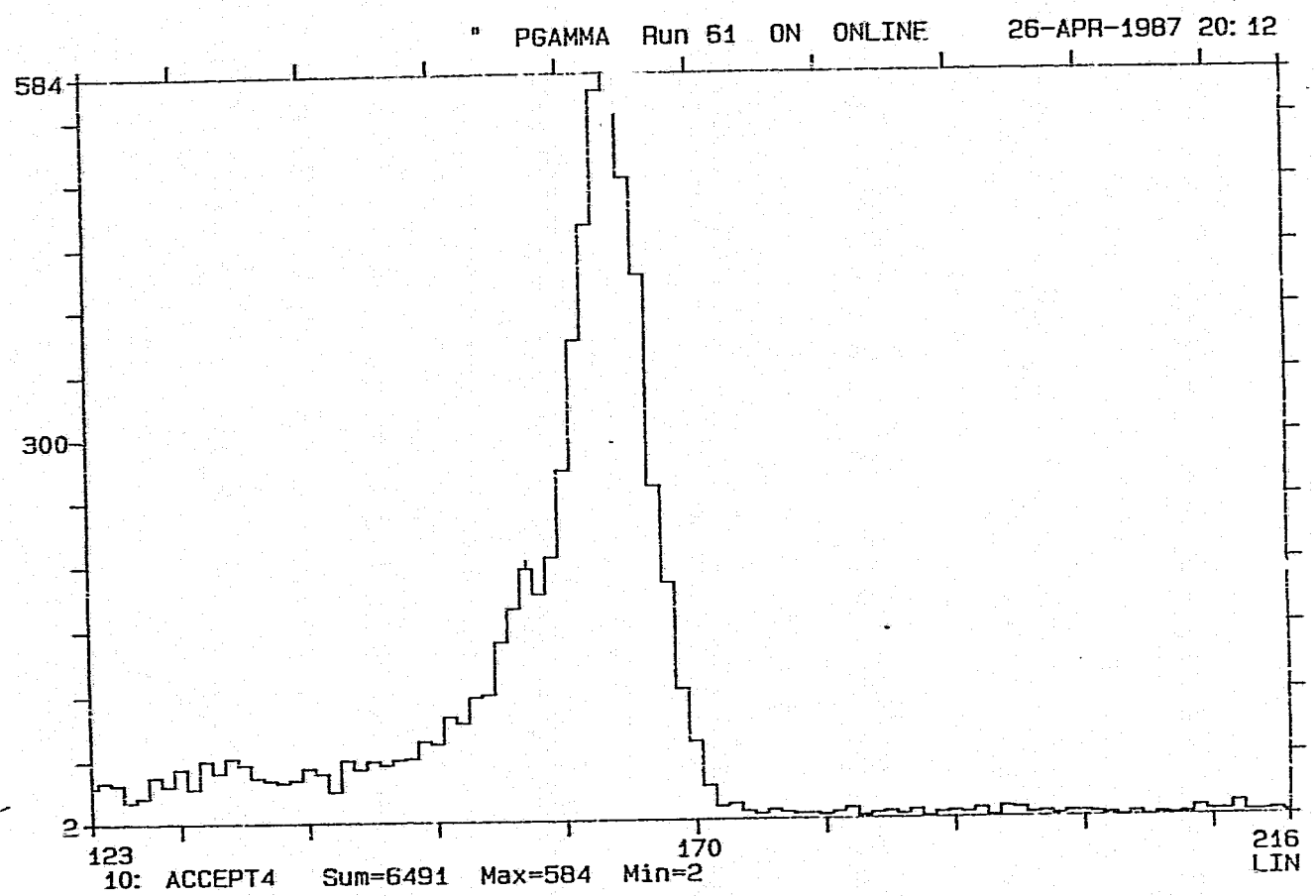

FIGURE 19 The 15.11 MeV line spectrum shows the separation of the first escape (15.11 − 0.511 MeV) peak.

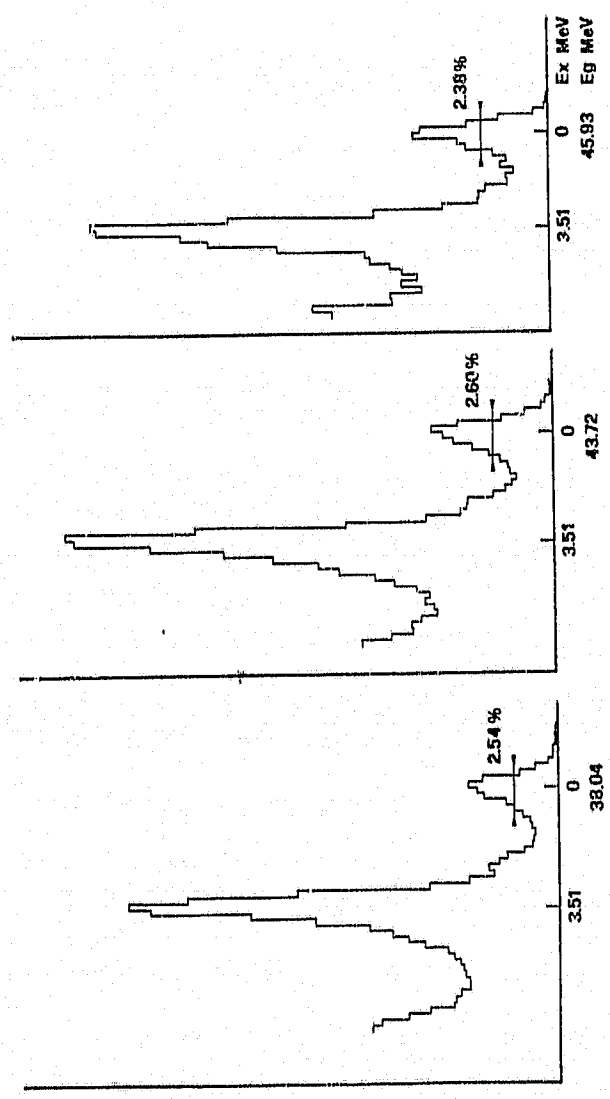

FIGURE 20 Photon spectra at thr- different high energy values to show the FWHM resolution of Hagar in standard experimental conditions.

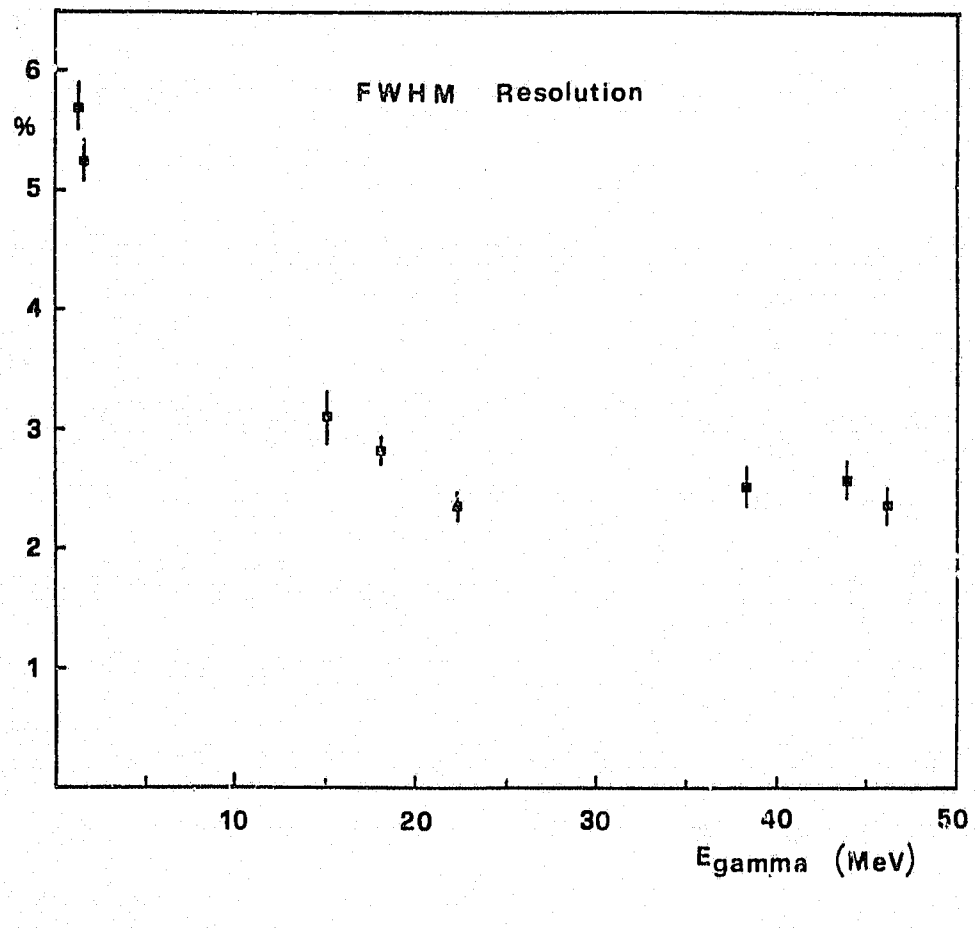

FIGURE 21 FWHM energy resolution as a function of peak energy as measured in standard Hagar running conditions.

effects of any remnant spread in uniformity on energy resolution are negligible.

As far as overall energy resolution is concerned, stringent tests using beams from the Tandem accelerator proved that both the design and the technical execution of the design resulted in state-of-the-art detector performance. Similarly in the demanding experimental conditions in radiative capture studies at substantially higher energies, with thick targets and in high beam current exposure, the performance of this detector was comparable to that of other spectrometers of the same type, even though we have further optimisation possibilities, such as on-line dynamic calibration and gain adjustment.

The electronics system deployed with Hagar proved for the combined assembly to have excellent timing characteristics with consequently very clean separation of neutrons and gamma rays. Hence accurate identification of photon events was readily achieved, together with excellent efficiency in pile-up rejection down to about 40 ns. Furthermore, following in a discrete and unambiguous fashion the different logic functions is comprehensive, allowing the dynamic analysis of essentially all possible reaction paths, so that an ever-improving understanding of the behaviour of the total system is evolving.

Hence we conclude, as will be substantiated also by the analysis of the actual data captured and considered, that design objectives have been met and an excellent detection system for medium energy photons is available.

REFERENCES FOR CHAPTER 3

1) A.M.Sandorfi and M.T.Collins
Nucl. Instr. and Meth. 222(1984)479

2) P.Corvisiero, M.Taiuti, A.Zucchiatti and M.Anghinolfi
Nucl. Instr. and Meth. 185(1981)291

3) M.Taiuti, M.Anghinolfi, P.Corvisiero, G.Ricco and A.Zucchiatti
Nucl. Instr. and Meth. 211(1983)135

4) A.Zucchiatti and J.P.F.Sellschop
South Afr. J. Phys. 9(1986)24

5) M.Anghinolfi , P.Corvisiero , E.Durante , M.Guarnone , M.Taiuti and A.Zucchiatti
Il Nuovo Cim. 77A(1983)277

6) C.Ohmori, N.Horikawa, T.Iwata, T.Nakanishi, S.Sakanaka and T.Toyama
Nucl. Instr. and Meth. A256(1987)361

7) A.Zucchiatti
Proc. Work. on Rad. Capt. Sigtuna 1987 pg 395

CHAPTER 4

RADIATIVE CAPTURE TO GROUND AND EXCITED STATES IN ^{13}N

4-1 The experimental program

The guideline for this research program was to establish information on radiative capture to the ground and excited states in ^{13}N in the excitation energy region from 40 MeV to about 60 MeV, which is characterized by the absence of systematic measurements. This is schematically the region of the second harmonic mode of the GDR collective excitation and of eventual quadrupole collective excitations. Figure 1 can help in locating the energy and relative amplitudes of the basic electric collective excitations built on the g.s. state of all nuclei [1] and give also an indication of where the collective excitations based upon nuclear excited states can be found. The second harmonic mode of the GDR has been observed in a few cases (^{28}Si, ^{12}C, ^{13}N) but described in detail, with complete yield and angular distribution functions only for ^{12}C. This is due to the extent of data from the reaction ^{11}B$(p,\gamma)^{12}$C collected already with low energy accelerators, consequent on the large (15.957 MeV) Q value of this reaction that allows the population of highly excited final states in ^{12}C at beam energies just below 40 MeV.

Before we proceed to a review of available data and to the analysis of our experiment it is convenient to recall, in simple terms, what we can learn, in principle, from our investigations. Let's first discuss the kind of angular distributions produced by a direct plus semidirect proton capture mechanism as opposed to possible influences of compound nucleus formation and decay. The latter involves redistribution of the entrance channel energy through the excitation of a large number of compound states (generally described by complex admixtures of single particle states) which will undergo a long sequence of decays and excitations until statistical equilibrium is reached amongst the various nuclear configurations. Their probabilities will be assigned statistically and the phases of the respective wave functions will be absolutely random. A process of this kind requires a time much longer than the average transit time of a bound nucleon across the nucleus

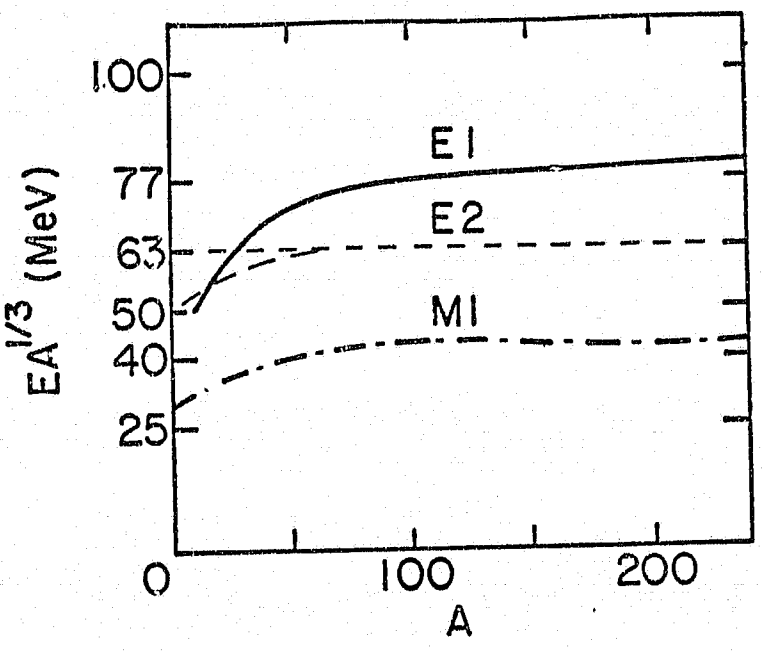

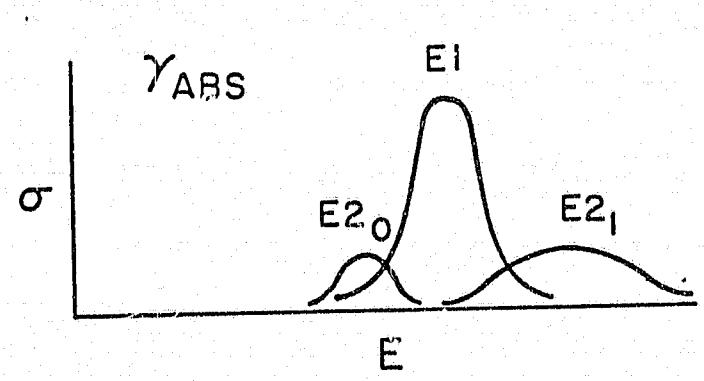

FIGURE 1 *Top* . Centroid energies of giant resonances as given by shell model calculations. *Bottom* Relative positions and heights of $E1$, $E2_0$ (isoscalar) and $E2_1$ (isovector) resonances as seen in an idealized gamma absorption spectrum. (from ref [1])

($\approx \frac{1}{3}A^{\frac{1}{3}}10^{-22}$sec). Therefore there is no correlation between the formation and decay of the compound nucleus; the collision direction will not remain a privileged direction and the reaction products are expected to be emitted isotropically in the c.o.m. system. Formally [2], applying the reciprocity theorem, making use of the hypothesis of independence of formation and decay processes and assuming random phases (i.e. non-interference) for the wave functions of the compound nucleus excited states, one can calculate explicitly:

$$\sigma_{\alpha\beta}(\theta) = \pi\lambda_\alpha^2 \sum_{JPjlj'l'} \frac{(2l+1)}{(2i+1)(2I+1)} A_J(jl,j'l',\theta) \frac{T^J_{\alpha lj} T^J_{\hat{\beta}\hat{l}'\hat{j}'}}{\sum_{\alpha lj} T^J_{\alpha lj}};$$

that is the angular distribution of a reaction proceeding from an incident channel α described by the quantities : i= spin of the incident particle, I = spin of the target nucleus, $\vec{j} = \vec{i} + \vec{I}$ = channel spin, l = orbital angular momentum in the incident channel, with primed quantities for the outgoing channel β and hats for time-reversal. J and P are respectively the spin and parity of the compound state, the T's are the transmission coefficients and λ_α is the wavelength associated with the incoming channel. The angular distribution [5-1] is obtained after summing over all allowed states, specifically over l, j, l', j', J and P subject to the triangular relations $\Delta(iIj)$ (in other words $|i-I| < j < (i+I)$), $\Delta(i'I'j')$, $\Delta(jlJ)$, $\Delta(j'l'J)$ and after averaging over the angular momentum states. The angular dependence of [5-1] is entirely contained in the term

$$A_J(jlj'l'\theta) = \frac{2(l'+1)(2J+1)^2}{4\pi} \left| \sum_L C^{Ll}_{000} C^{Ll'l'}_{000} W(JJll, Lj) W(JJl'l', Lj') P_L(\cos\theta) \right|$$

where the sum extends over all even L such that $0 < L < \min(2l, 2l', 2J)$. L even implies symmetry around 90 deg and, at low energy where s-wave capture dominates, also isotropy. For large spin changes large anisotropies are expected but still fore-aft symmetry should be observed. The direct-semidirect process is a fast process and does not allow rearrangement of degrees of freedom such as the phases between different transition modes, which will as a matter of fact interfere, producing the typical angular distributions [1-2] characterized by sizeable odd a_k coefficients and ultimately by forward peaking, as our analysis will show. To note is that in the case of a single transition (like the $1^- \rightarrow 0^+ 15.11$ MeV in ^{12}C discussed later), no interference is possible and again fore-aft symmetry is expected.

We expect furthermore to see energy spectra dominated by those transitions which involve final excited states with large single-nucleon spectroscopic factors (e.g. the 3.51 MeV state in ^{13}N). The centroid energy of the GDR that is found based upon these states is, according to the Brink hypothesis, independent of the detailed structure of the state. But the GDR width and its strength are often a strong function of the state and of its coupling to the entrance channel, being the GDR's larger for highly excited states, and their strength enhanced for states which match the entrance channel configuration [3]. Exploring the region of the second harmonic of the GDR, it should therefore be possible to see a level substructure reflecting the low-lying levels as well as their influence on the excitation curve of the $2\hbar\omega \rightarrow 1\hbar\omega$ transition.

The actual experimental situation looks as follows. In γ spectra from proton radiative capture to ^{13}N a broad structure has been observed at excitation energies around $2\hbar\omega$ ($E_x \approx 43$ MeV). Only a single energy point [4] has been measured, preventing any proper understanding of this reaction channel. The multipolarities involved in this transition were extracted from the analysis of the $E_p = 44$ MeV angular distribution that was compatible with a dominant E1 transition mode interfering with a quadrupole mode. Also the cross sections for radiative decay to the lowest lying states (*g.s.*, 2.37 MeV, 3.51 MeV) has been measured rather systematically but only below $E_x = 48$ MeV [5] at a fixed angle of 90 deg to the beam direction. Measurements have been taken at a few higher proton energies (40, 50, 60 and 80 MeV) [6] and angular distributions for the g.s and 3.55 MeV transitions at $E_p = 40$ MeV [7]. In relation to the sparse information on the ^{12}C$(p,\gamma)^{13}$N it was observed that, for final states described in neighbouring nuclei (e.g. ^{12}C, ^{13}N) by an inert core plus a proton in the same single particle orbit, the differential cross sections are predicted to be identical [6]. This prediction has found clear experimental support, therefore an approximate extension of the set of data for the reactions ^{12}C$(p,\gamma)^{13}$N and ^{12}C$(p,\gamma_{2+3})^{13}$N [6] at 50 and 60 MeV can be made from the cross sections of the equivalent ^{11}B$(p,\gamma)^{12}$C(4.43) and ^{11}B$(p,\gamma)^{12}$C(19.6) channels. At high energies the addition of beam polarization has given more information on the $< E1 > / < E2 >$ ratio in the (p,γ_0) transition even if in large (≈ 10 MeV) steps [7]. The presence of maxima in the excitation functions of both the g.s. and the γ_{2+3} channels observed by Fisher et al. [5] at excitation

energies from 33 to 46 MeV still remains an open question since they were not confirmed by subsequent experiments. In this framework the possibility of extensively investigating radiative capture in ^{13}N at beam energies from 40 to 60 MeV and more, was recognised and implemented using the facilities at NAC.

4-2 Experimental Details

The allotted beam time and the structure thereof had to be made compatible with both the detector development on one hand and an experimental program of sufficient extent. How the detector set-up has been developed and established has been discussed in chapter 3. The research program was concentrated on the identification and measurement of any possible (p,γ_x) channel in ^{13}N at excitation energies from 40 to 52 MeV. A solid polyethylene target equivalent to 31.7 mg/cm^2 of ^{12}C was bombarded with protons having energies of 40, 43.1, 46, 48, 49, 50, 52 , 54 and 66 MeV, at beam average currents of 10-50 nA. A summary of the experimental program performed is given in table 1, while an example of typical count rate conditions is given in table 2. Doses of $200 - 1000\,\mu$C were accumulated. Detailed angular distribution measurements were taken at every energy, with not less than six angles per energy but usually 9 angles (as seen in table 1). A borax and paraffin plug (15% borax in mix with wax $\rho \approx 0.85\,$g/cm^2) was inserted into the lead collimator to further reduce the neutron background, specially at high energies and extreme collection angles. Its effect on the gamma count rate is taken into account by the simulation code that gives the collection efficiency and the response function of the detector. We can define a collection efficiency ϵ_c as the ratio of the number of photons collected by the system in its anticoincidence ($E_{th} \approx 50-200$ keV for the plastic scintillator) configuration to the number of photons emitted inside the detector solid angle. We can also define an anticoincidence efficiency ϵ_a as the ratio of the number of photons collected in anticoincidence to the number of photons collected in coincidence. Table 3 summarizes the computed ϵ_c and ϵ_a values at different photon energies and plastic scintillator threshold.

TABLE I

Summary of the most relevant experimental quantities

E_p (MeV)	Lab Angle (deg)	Charge (μC)	Current (nA)	Target (mg/cm^2)
40	30	779	50	44.9
	45	1001	53	"
	60	794	53	"
	75	1003	56	"
	90	1004	50	"
	105	1400	50	"
	120	1851	53	31.7
	148	1802	52	"
43.1	30	312	25	44.7
	45	329	25	36.6
	60	246	25	44.7
	75	254	25	36.6
	90	280	25	44.7
	105	354	30	36.6
	120	396	20	"
	136	389	25	"
	148	448	15-35	"
46	30	935	52	44.9
	45	653	49	"
	60	959	53	"
	75	647	33	"
	90	1054	52	"
	105	650	54	"
	120	685	57	"
	135	651	49	31.7
	148	651	54	"
48	30	301	20	44.9
	45	453	20	"
	60	333	20	"
	75	436	20	"
	90	399	20	44.9
	105	448	20	"
	120	450	20	"
	135	346	20	31.7
	147	417	20	"

TABLE I (continued)

E_p (MeV)	Lab Angle (deg)	Charge (μC)	Current (nA)	Target (mg/cm^2)
49	30	566	48	44.9
	45	415	47	"
	60	302	25	"
	90	593	49	"
	100	775	50	"
	135	379	25	31.7
50	30	111	3	44.9
	46	408	20	"
	60	146	11	"
	90	316	10	"
	120	224	11	"
	135	65	20	31.7
	147	169	10	"
52	30	240	17	44.9
	45	323	12	"
	60	360	12	"
	75	293	21	"
	90	208	13	"
	100	205	11	"
	135	378	18	31.7
	148	432	32	"
54	31	153	15	44.9
	45	224	15	"
	60	152	15	"
	75	234	15	"
	90	249	15	"
	105	189	10	"
	120	207	15	"
	148	161	10	31.7
66	42	190	10	44.7
	60	180	10	"
	75	317	25	36.6
	90	185	12	44.7
	105	243	20	36.6
	147	229	20	"

TABLE 2

Typical Count Rate Conditions $E_p = 49$ MeV $I = 12$ nA

Module	Counts/sec
High threshold CF(NaI)	300
LO-HI Cons. Frac. Dis.	5×10^4
Low Threshold NaI	7×10^4
Plastics CFD	1.3×10^5
LO-LO Pile-up Rej.	4×10^3
HI-HI Pile-up Rej	Negligible
LO-HI Pile-up Rej	20

TABLE 3

Computed efficiency values

E_γ (MeV)	ϵ_c(50 keV)	ϵ_a(50 keV)	ϵ_c(100 keV)	ϵ_a(100 keV)	ϵ_c(200 keV)	ϵ_a(200 keV)
20	0.321	0.405	0.342	0.433	0.390	0.493
30	0.242	0.285	0.265	0.312	0.319	0.375
40	0.206	0.233	0.228	0.258	0.272	0.308
50	0.169	0.184	0.187	0.204	0.237	0.258
60	0.133	0.142	0.150	0.160	0.191	0.203

4-3 Spectrum fitting procedure

For the data analysis we have followed a rather practical technique [8] using the program FITGAM [9] slightly adapted to fulfill our new requirements. The fitting strategy consists of reproducing the measured spectra with a series of tabulated response functions and a linear background. The response functions are computed by the Monte Carlo code

discussed in chapter 2, which receives as input data the detector geometry and the nature of the materials exposed to the photon flux.

The response function is convoluted to fit nearly isolated gamma lines, generated basically from the $^{11}B(p,\gamma_0)^{12}C$ and $^{11}B(p,\gamma_{2+3})^{12}C(4.43)$ reactions at various beam energies. It is subsequently digitized in $E_{\gamma_p}/100$ energy steps at selected peak energies E_{γ_p} from 10 to 60 MeV and stored in the file DATFUN.DAT. The response function at any intermediate energy $E_{\gamma_{p1}} < E_\gamma < E_{\gamma_{p2}}$ is interpolated from those tabulated at $E_{\gamma_{p1}}$ and $E_{\gamma_{p2}}$ respectively. The code FITGAM is based on the CERN library minimization program MINUIT and performs the following data reduction. First the calibration line is evaluated; ultimately this is established by a best fit through a set of calibration points (e.g. 15.1 MeV, (p,γ_0) peak, (p,γ_{2+3}) peak, etc. etc.) and the parameters BETA (slope) and GAMMA (intercept) are determined and fixed for the rest of the analysis. The spectrum is divided into a reasonable number of regions (usually five) that are analysed one by one from higher to lower gamma energies. An extra region is chosen above the (p,γ_0) peak so that only cosmic events are included in it. In this region a constant background is fit to the points and then subtracted from the entire spectrum. For all other regions the code adjusts 11 parameters to minimize a χ^2 function. Parameters are the slope TFOND of a linear background whose intercept is for continuity set equal to the value of the background in the previous region at the contact point; the heights of at most five peaks (ACCA1, ACCA2, ACCA3, ACCA4 and ACCA5) and the shift in channels (DELTA1, DELTA2, DELTA3, DELTA4 and DELTA5) measured from the channel value that is attributed, on the basis of a preliminarly estimated calibration line, to any peak in the region. The χ^2 function is minimized to best fit and the portion of the fitted spectrum due to the peak tails, which normally exceeds the limits of the fitted region towards lower energies is subtracted from the rest of the spectrum. The process is iterated until the last region is fitted. For any peak the cross section is evaluated from the area of the fitted response function (N_γ[n]), the solid angle ($\Delta\Omega$[sr]), the collection efficiency (ϵ_c), the target thickness(τ [gcm^{-2}]), and the collected charge (Q [C]) by the usual relation

$$\frac{d\sigma}{d\Omega} = \frac{N_\gamma e_0 A}{Q\Delta\Omega\tau N_0 \epsilon_c}$$

where A is the atomic weight of the target, e_0 the unitary charge and N_0 Avogadro's number. The errors in the physical quantities are added quadratically and extended to the cross section. For any peak the computer output lists the peak area, the cross section, the channel, the absolute gamma energy computed from the calibration line, the measured excitation energy, the efficiency, and finally the absolute gamma energy computed from the reaction kinematics (m_p = projectile mass, M_R = recoiling mass) at the given proton energy (T_p), collection angle (θ) and final state excitation energy (E_x):

$$h\nu(\theta) = \frac{T_p(M_R - m_p) + Q(T_p + M_R) - Q^2/2}{T_p + Q + M_R - \sqrt{T_p(T_p + 2m_p)}\cos\theta} - E_x$$

A few considerations must be made before proceeding to the examination of our spectra. The first concerns the DATFUN.DAT file. Clearly this file can be reliably constructed only from a large set of experimental observations, preferably on rather isolated peaks and over a large energy range, so as to include in the response functions both intrinsic and instrumental effects. We would like to recall that there were some practical limitations imposed by the accelerator. This is a totally new machine and our experiment is only the second one to begin at NAC. Apart from the two test points at 66 and 200 MeV, each of the energies at which we worked, was selected for the first time ever specifically for our runs. This required the development of experience in the operation of the machine and led for example to begin our investigations at 66 MeV, where the machine behaviour was best understood, and to progress to lower energies in not too large steps. Running the accelerator alternatively at very low energies (e.g. 20 MeV; appropriate for response function measurements through the reaction $^{11}B(p,\gamma)^{12}C$) and at higher energies (e.g. 50 MeV; necessary to our systematic investigation of the $^{12}C(p,\gamma)^{13}N$ reaction), proved to be extremely unpractical and priority was therefore given to the reaction study program rather than to an exstensive response function study also. However the DATFUN.DAT file constructed in great detail for a similar spectrometer [10] was available. This other instrument operated at an anticoincidence threshold of 170 keV, but was provided with a shorter plastic scintillator anticoincidence shield. Its convoluted response functions were capable, in almost every instance, of giving good fits to our $^{12}C(p,\gamma_0)^{13}N$ and $^{12}C(p,\gamma_{2+3})^{13}N$ lines

(figure 2) for the runs at 40, 43.2, 46, 49 and 52 MeV. We have therefore assumed identical response function shapes for the two instruments and for the entire large energy range ($\Delta E_\gamma \approx 25\,\mathrm{MeV}$) involved in our spectra, and corrected afterwards for efficiency differences, referring to table 3. The fact that Hagar was operated in these runs at higher beam currents and large solid angle, although at lower anticoincidence rejection threshold, may well account for the striking similarity of the two sets of response functions. Runs at 48, 50 and 54 MeV were performed at even lower anticoincidence threshold ($E_{th} = 50\,\mathrm{keV}$) and low current (never exceeding 20 nA): the analysis of spectra with the DATFUN.DAT response functions proved in these three cases to be relatively poor and showed, as might be expected, that the Hagar response functions are, in more conservative operating conditions, narrower than for the Milan detector. The ultimate goals of this work will go certainly beyond this thesis presentation; a careful investigation of the response function will be made before proceeding to the data analysis of the 48, 50 and 54 MeV runs. Beam time allocation at NAC does not allow that in the immediate future. We have therefore extracted from runs at the last three energies, angular distributions normalized to A_0 for the (p,γ_0) and (p,γ_{2+3}) channels. Although the absolute scale may be incorrect, since we only have integrated a portion of the peaks with no tail included, the relative angular distributions and the Legendre coefficients should be little sensitive to this as the general agreement found in figures 20 and 22 testifies. Despite this forced incompleteness for 3 energies only, we have a good description of the observed phenomena on the basis of all the other energy points.

We would also like to comment on the linear background that is added, in any region, to the set of peaks in order to fit the collected spectra. Some other analyses [11] [12] have been performed using only a set of response functions to fit the spectra but others have used our more extensive technique [13]. We believe that there is some support for the technique we have adopted. On one hand one has to consider that the computed response functions have proven very reliable when compared to well isolated gamma lines measured by detectors of different shape and configuration up to about 300 MeV [14] [15] [16]. There is no obvious reason to object to the predictions of these codes, which normally give not very long tails at low energies, and to arbitrarily extend the predicted tail making them assume a

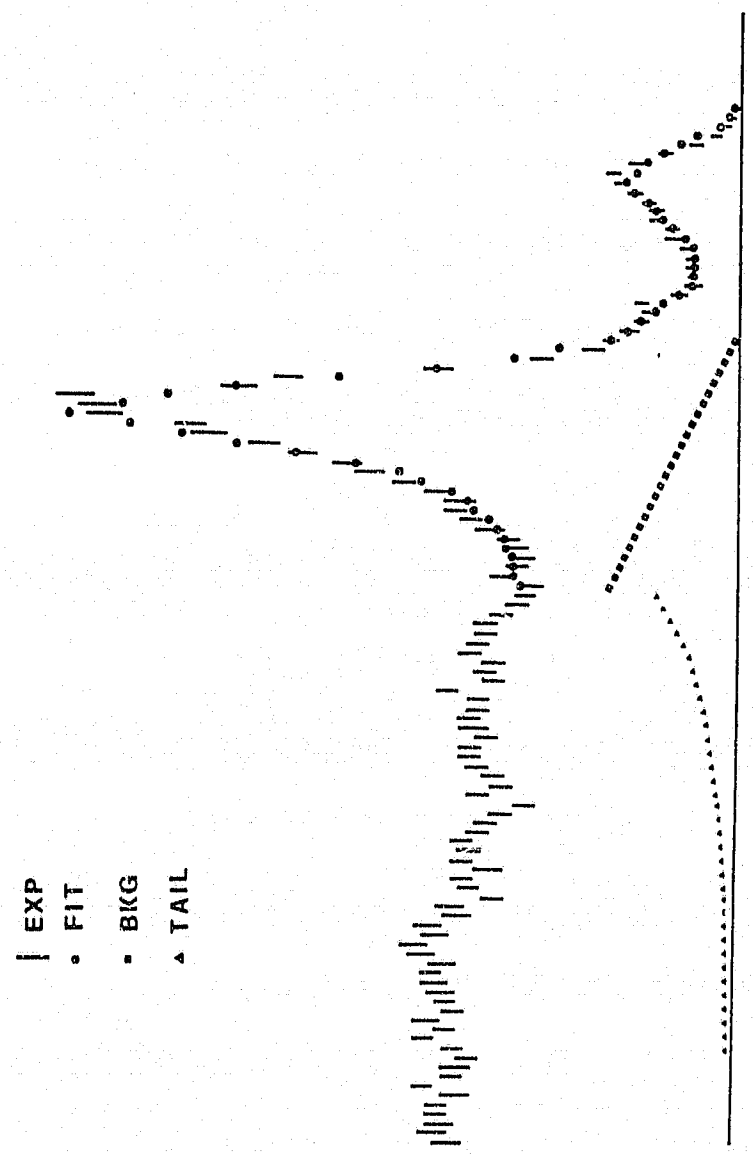

FIGURE 2 An example of our spectrum fitting procedure applied to ^{13}N in the excitation energy region that includes the (p,γ_0), the (p,γ_1) and the (p,γ_{2+3}) transitions. Shown are the total fit, the background and the tail contributions.

very slowly decreasing or even constant trend towards lower energies. These nearly constant tails will add up to generate a sort of step function that ultimately contributes a consistent part of the fitted yield. None of the experiments performed on isolated gamma peaks or with monoenergetic electrons shows such a behaviour. Even for rather well separated peaks like the γ_0 and γ_1 from $^{11}B(p,\gamma)^{12}C$ the background has to be considered [8] [16]. In our case this is evident when we try to fit the first portion of the $^{12}C(p,\gamma)^{13}N$ spectrum with only three computed response functions. A background must be added only from the particle decay threshold energies, which the program computes from standard mass tables and assumes as the background starting point (figure 2). This is logically consistent with the background being due to the many possible reaction channels through which the compound nucleus decays by particle emission and consequent electromagnetic deexcitation before reaching a stable configuration. Ignoring this background component and adjusting the tails to fit the first region of e.g. $^{11}B(p,\gamma)^{12}C$ with only two response functions, assumed subsequently as standard, leads, in our observation, to an overestimate of the transition cross sections specially for the peaks at high excitation energy. A way of complementing the evidence given by the experimental single energy spectra already mentioned, would be to compare the photon spectra collected in and off coincidence with the recoiling compound nucleus. Apart from the detection efficiency, which will be drastically reduced when in coincidence, and other instrumental effects like residual pile-up, gain drifts etc., the two spectra should be equivalent if the first one is due only to photons emitted prior to the compound nucleus deexcitation by particle emission. The difficulty of a coincidence experiment is very well known and sets a practical limit to the selective study of the reaction channels in which we are interested. To the best of our knowledge only two sets of data of this sort are available. One concerns the $D(d,\gamma)^4He$ reaction where recoiling alpha particles were detected in coincidence with gammas [17]; the other relates to the reaction $^{12}C(^{16}O,\gamma)^{28}Si$ [18] measured in and off coincidence with the recoiling ^{28}Si nucleus. In the first case the statistical fluctuations in the collected coincidence spectra are, as a matter of fact, compatible with largely different response functions. In the second case the particle decay threshold is coveniently very low ($\approx$ 13 MeV); we should therefore obtain the same peak-to-valley ratios in both single and coincidence spectra for the first low lying states.

The values extracted from figure 5 of ref [15] are for the first three peaks: 3.40 (g.s.; 3.35 in singles), 8.25 (1.78 MeV; 5.43 in singles), 5.79 (4.62 MeV; 1.42 in singles). Since they should be equal in pairs they therefore indicate that some background is evidently present even in the first portion of the singles spectrum. The singles spectrum suffers indeed from admitted large pile-up contributions that affect the low-lying peaks for which the ratio is lower in the singles spectrum, and prevent the extraction of sensible peak-to-valley ratios in the region of excitation energy above 13 MeV, where we should test our background assumption. In conclusion, while there is no clear experimental evidence of the absence of background in photon spectra generated by radiative capture, the good agreement between the computed and measured isolated high energy gamma response functions justifies our fitting procedure.

4-4 Data analysis

A few examples of spectra collected are given in figures 3, 4, 5, 6 and 7. The excitation and gamma energy scales are reported in each of these figures and help us to draw attention to some very important points on which we would like to comment on a qualitative basis before proceeding to a numerical analysis:

a) We can clearly distinguish, at any explored energy, transitions to the states at $0(\frac{1}{2}^-)$, $2.37(\frac{1}{2}^+)$ and the pair at $3.509(\frac{3}{2}^-)$ and $3.547(\frac{5}{2}^+)$ MeV. The largest transition strength is concentrated on the (p,γ_{2+3}) channel which, from previous observations, extended even to very high energies[6] ($E_p \approx 80$ MeV), is known to remain the most strongly populated state.

b) Transitions take place even to high-lying and very high-lying states as expected. There are in fact, but not reliably separable, transitions to the pairs of states at $6.88(\frac{3}{2}^+)$ and $7.90(\frac{3}{2}^+)$ and $10.78(\frac{1}{2}^-)$ and $11.87(\frac{3}{2}^-)$ MeV. Transitions in a) and b) are clearly interpreted as (p,γ) reactions from the kinematical variation of their peak energy.

c) In the low E_γ region all spectra are dominated by a broad structure that remains centered around $E_\gamma = 24$ MeV whatever the beam energy is, in contrast to what would happen in possible (p,γ) transitions. Looking in finer detail at the spectra in figures 3 to 7, we consistently find evidence of structures at about 19.5, 22.5, 23.5, 24.0, 26 and

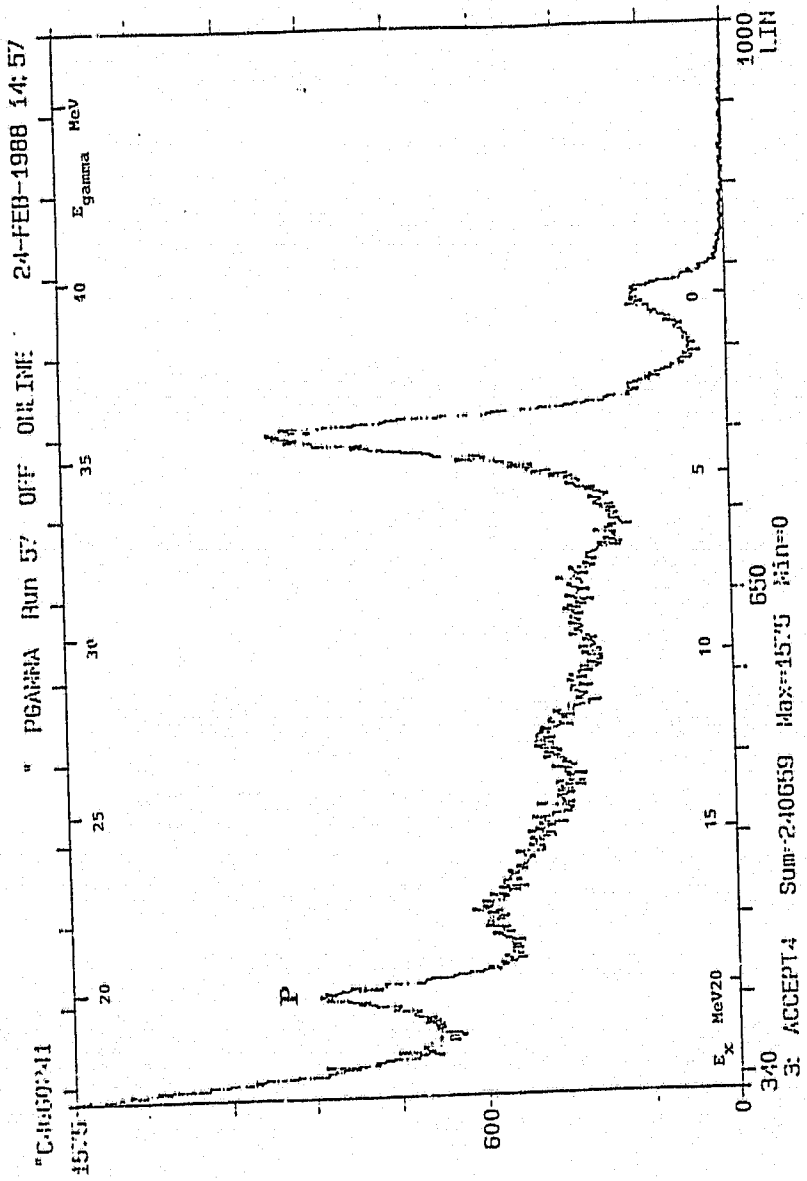

FIGURE 3 A ^{13}N photon energy spectrum from radiative proton capture at $E_p = 40$ MeV and $\theta_\gamma = 60$ deg. Shown are gamma energy and excitation energy scales.

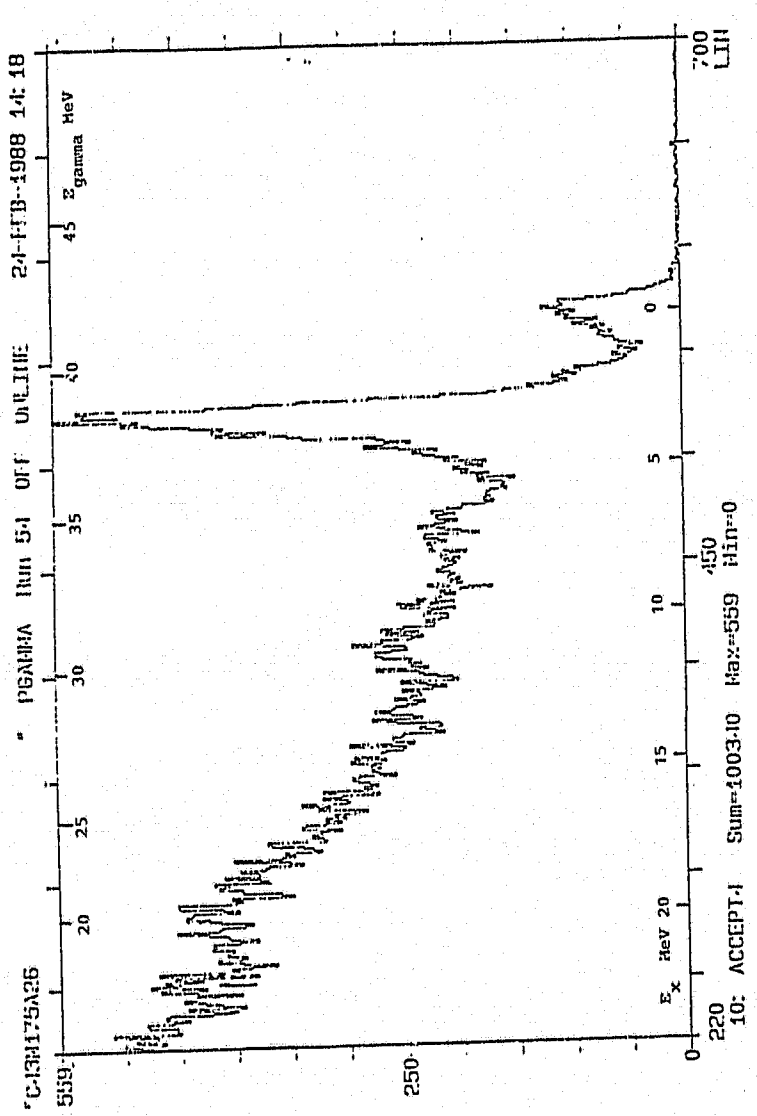

FIGURE 4 A ^{13}N photon energy spectrum from radiative proton capture at $E_p = 43$ MeV and $\theta_\gamma = 75$ deg. Shown are gamma energy and excitation energy scales.

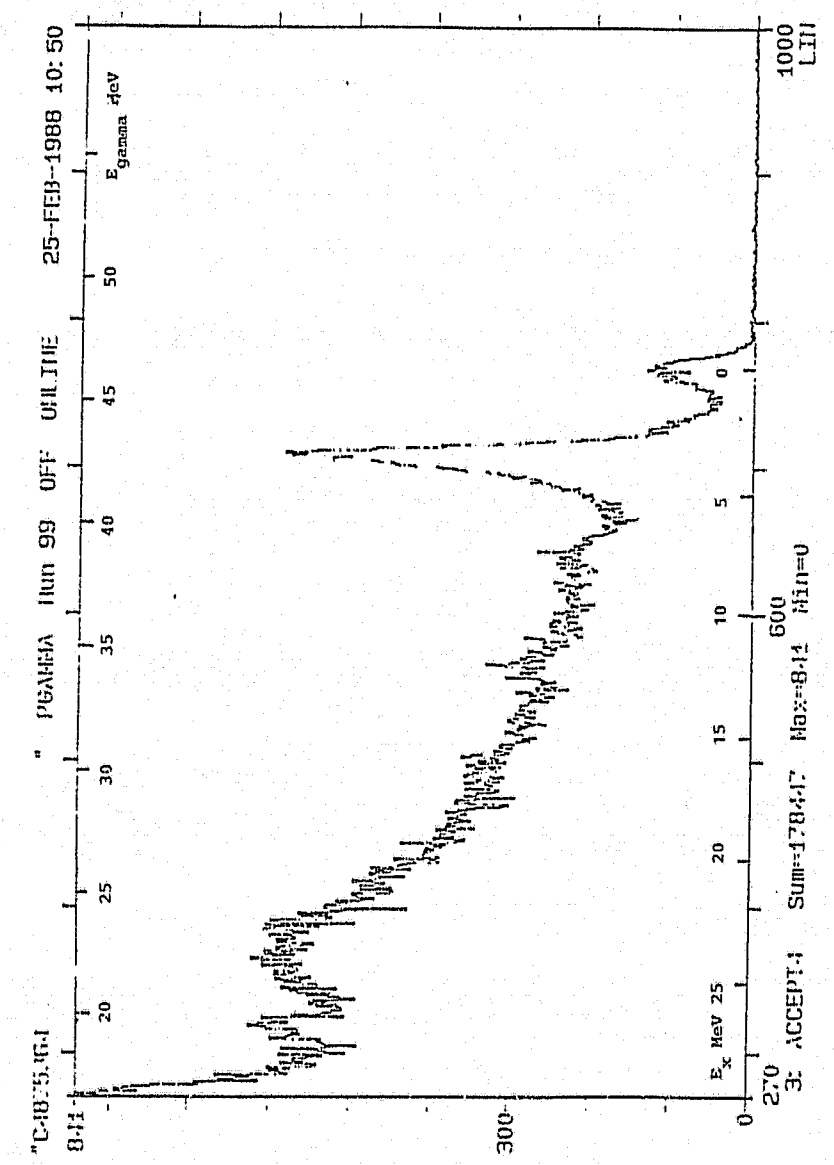

FIGURE 5 A ^{13}N photon energy spectrum from radiative proton capture at $E_p = 48$ MeV and $\theta_\gamma = 75$ deg. Shown are gamma energy and excitation energy scales.

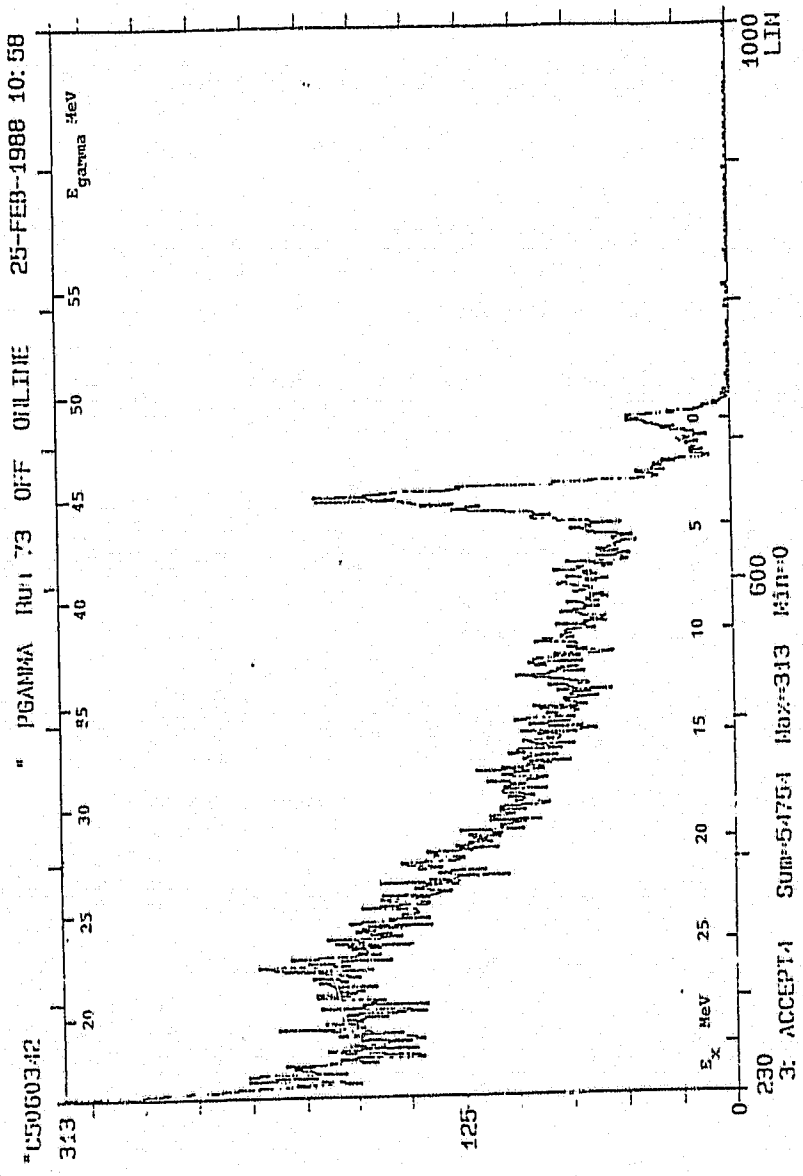

FIGURE 6 A ^{13}N photon energy spectrum from radiativ proton capture at $E_p = 50$ MeV and $\theta_\gamma = 60$ deg. Shown are gamma energy and excitation energy scales.

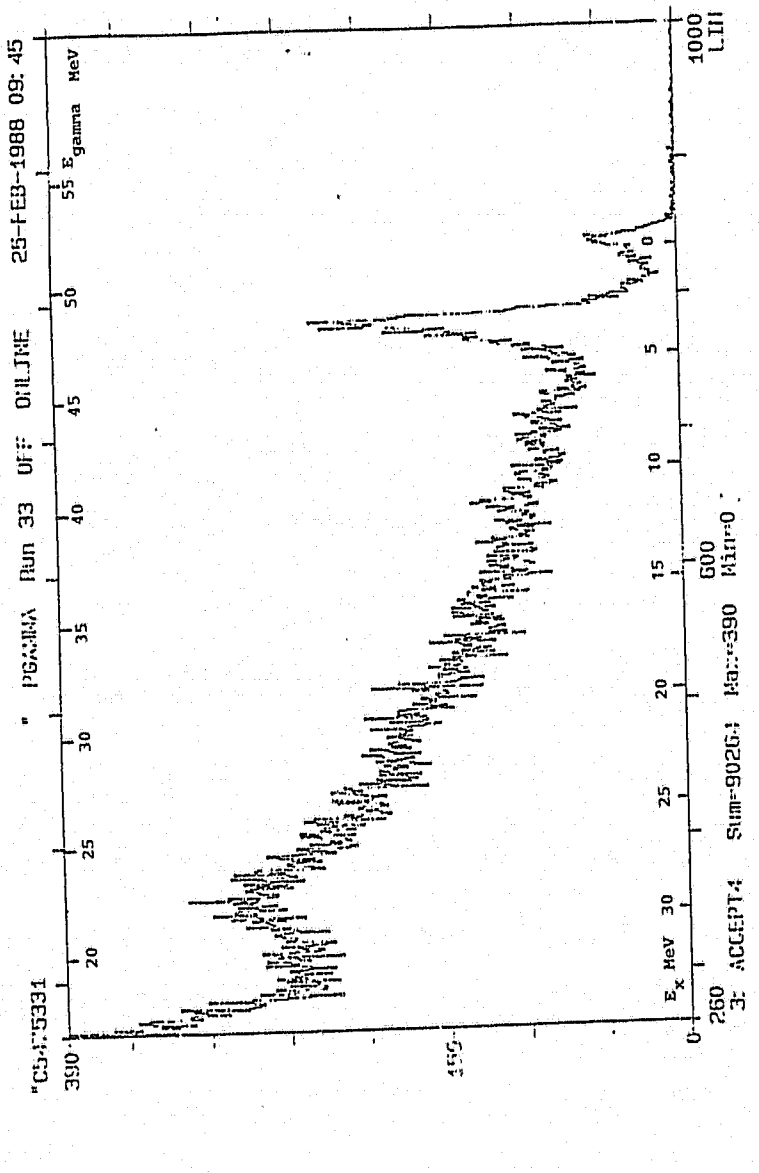

FIGURE 7 A ^{13}N photon energy spectrum from radiative proton capture at $E_p = 54$ MeV and $\theta_\gamma = 75$ deg. Shown are gamma energy and excitation energy scales.

27 MeV, this last being more evident at $E_p = 50$ and $E_p = 54$ MeV. The intensity of the 19.5 MeV peak (marked P in figure 3) shows appreciable variation with the beam current in comparison with that of all other peaks (see figure 8). Furthermore its energy is very close to the sum of the energies of the two more intense peaks in the spectrum: the 4.43 and the 15.11 MeV lines coming from $(p, p'\gamma)$ inelastic scattering for ^{12}C. We therefore attribute this peak to the residual pile up of these two gammas in close occurence (time difference below 40 ns), that the LO-HI pile up rejection circuitry cannot separate. The other fixed energy gamma peaks suggest convincing correspondence with (p, p') peaks observed at $E_p = 45$ and $E_p = 150$ MeV in inelastic scattering off ^{12}C. Buenerd et al. [19] identify $1^-; T = 1$ states in the continuum of ^{12}C at energies of 22.6, 23.5, 23.92 25.8 and 27 MeV. The $L = 1$ assignment is made from the comparison with Distorted Wave Born Approximation (DWBA) calculations while the isovector nature is deduced from the absence of these states in inelastic scattering of alphas off ^{12}C.

d) The region between $E_{\gamma_a} = 27.5$ MeV and $E_{\gamma_b} = E_{\gamma_0} - 12$ MeV is rather complex. Let us make some considerations for $E_{\gamma_a} < E_{\gamma_b}$ as in the cases where $E_p = 48$, 50 and 54 MeV (figures 5,6 and 7). Firstly (p, γ) transitions are seen to a group of states that are identified as the 13.96($\frac{3}{2}^+$) MeV, the 15.97($\frac{7}{2}^+$ MeV) and the 17.2 MeV state in ^{13}N. It also appears that some strength builds up at excitation energies from 19 MeV to about 23 MeV. Structures related to these (p, γ) transitions are only evident at $E_p = 52$ and $E_p = 54$ MeV, as a broad shoulder. We have attributed the gamma transitions observed at $E_p = 52$ MeV, to final states in ^{13}N at 18.42 MeV($\frac{3}{2}^-$), 19.88 MeV($\frac{3}{2}^+$) and 20.90 MeV($\frac{5}{2}^+$). Since the states involved are ^{13}N states located around 22 MeV they should be the 2p-1h component states of the ^{13}N g.s. GDR. The structure seen at 52 and 54 MeV proton energy is therefore the effect of the decay of the second harmonic collective excitation of the compound nucleus, decaying to states in the GDR region of the same nucleus, ^{13}N.

e) One would expect a maximum in the excitation function of the (p, γ) transitions to states relative to the g.s. GDR of ^{13}N at about twice the GDR centroid energy, i.e. at about $E_x = 44 - 46$ MeV, corresponding to proton energies around 45-47 MeV.

In this case the $2\hbar\omega$ transition in ^{13}N is unfortunately superimposed on the $(p,p'\gamma)$ transitions to the set of $1^-;T=1$ states already identified and no clean separation of the two contributions is possible. Only at one energy did we see the $2\hbar\omega$ fairly clearly. Also to some extent problematic is the extraction of information for the (p,γ) transitions to the three states at 13.96, 15.97 and 17.20 MeV, for $E_p < 46$ MeV, where for some E_x the $E_{\gamma_a} = 27.5$ MeV value can exceed the $E_{\gamma_b} = E_{\gamma_0} - E_x$ value.

4-5 Evaluation of Cross Sections

The gamma spectra were subdivided into five regions for the fitting procedure: the first included excitation energies from 0 to 5.5 MeV, the second covered from 5.5 to 12.5 MeV; the third extended from 12.5 to 18.5 MeV, the fourth and fifth covered respectively the $2\hbar\omega$ and the $(p,p'\gamma)$ structures. Of course when some of the structures could not be separated (as at the lowest proton energies) the number of regions was reduced accordingly. As an example of fitted spectra we present figure 8 which concerns the radiative capture of 43.2 MeV protons at two photon laboratory collection angles.

The cross sections extracted from the various gamma spectra have been grouped into angular distribution functions for the transitions g.s., 2.37, 3.51, 6.88+7.90, 10.78+11.87 and 13.96+15.97+17.20, whenever possible. At $E_p = 40$ MeV the (p,γ) to the states around 16 MeV and the $(p,p'\gamma)$ in ^{12}C are not distinguishable. Equally merged are the $(p,p'\gamma)$ structure and the second harmonic deexcitation at proton energies below 50 MeV. At $E_p = 52$ MeV one can extract cross section values for (p,γ) transition to states at about 18.42, 19.88 and 20.90 while it is only at $E_p = 54$ MeV that transitions can be seen to states up to 23 MeV, but as already reminded, further information is necessary about the response function before trial data are extracted from spectra at 48, 50 and 54 MeV. Table 4 gives a comprehensive summary of the data extracted at various beam energies. The errors reported are statistical only but the errors introduced by the uncertainty in the background slope have also been estimated and transferred to the angular distribution points, before analysis with the code DISANG [20]. This is based on the MINUIT routine, reduces the experimental points to the center of mass system [21] and fits the angular

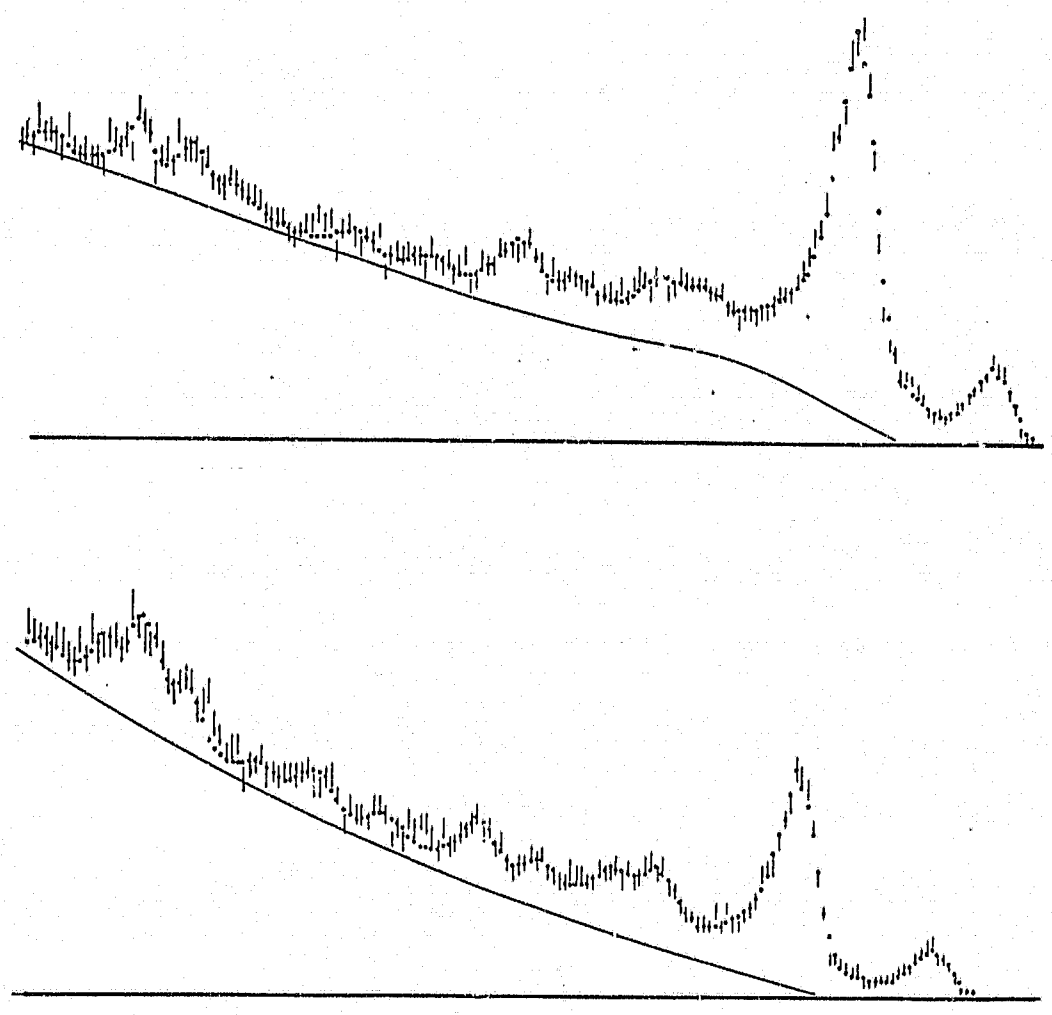

FIGURE 8 An example of complete spectrum fitting for proton radiative capture to ^{13}N at $E_p = 43.2$ MeV and two different photon collection angles (60 deg upper part; 120 deg lower part). Shown are the total fit (dots) and the subtracted background (full line).

TABLE 4

Summary of Extracted Cross Sections

Proton Energy 40 MeV

Angle	X-Sec [nb/sr]	+/-	X-Sec [nb/sr]	+/-	X-Sec [nb/sr]	+/-	X-Sec [nb/sr]	+/-	X-Sec [nb/sr]	+/-	X-Sec [nb/sr]	+/-
30	182	7	64	2	776	13	163	7	111	4	78	3
45	224	8	114	4	961	33	204	7	126	5	120	5
60	228	8	98	4	995	34	186	7	129	5	125	5
75	196	7	93	10	955	99	199	7	119	4	166	6
90	175	6	78	3	737	25	170	6	124	5	122	7
105	118	4	44	2	524	40	153	5	89	3	138	6
120	71	3	11	1	350	12	136	5	82	3	114	4
148	17	1	2	0	134	5	103	4	109	4	189	7
	(p,g0)		(p,g1)		(p,g2+3)		Ex=7.5		Ex=11		(p,p')	

Proton Energy 43 MeV

Angle	X-Sec [nb/sr]	+/-	X-Sec [nb/sr]	+/-	X-Sec [nb/sr]	+/-	X-Sec [nb/sr]	+/-	X-Sec [nb/sr]	+/-	X-Sec [nb/sr]	+/-
30	170	6	92	4	737	25	62	3	123	5	11	4	115	3
45	212	8	122	5	926	32	152	7	178	7	27	4	171	6
60	294	11	123	5	1136	39	173	8	182	8	35	5	225	8
75	252	10	109	5	1018	35	178	8	205	9	43	7	252	8
90	200	7	135	5	682	23	117	5	154	6	31	5	238	7
105	126	5	50	2	493	17	117	5	102	5	32	4	201	7
120	94	4	24	1	330	12	128	6	90	4	22	4	187	6
136	52	2	21	1	160	6	103	5	95	4	22	4	141	4
148	29	2	2	0	104	4	101	4	86	4	19	3	96	4
	(p,g0)		(p,g1)		(p,g2+3)		Ex=7.5		Ex=11		Ex=13.96		(p,p')	

TABLE 4 (continued)

Proton Energy 46 MeV

Angle	X-Sec [nb/sr]	+/-	X-Sec [nb/sr]	+/-	X-Sec [nb/sr]	+/-	X-Sec [nb/sr]	+/-	X-Sec [nb/sr]	+/-	X-Sec [nb/sr]	+/-	X-Sec [nb/sr]	+/-
30	310	11	101	4	1295	44	289	10	166	6	132	5	314	11
45	283	10	82	3	1348	39	250	9	187	7	135	5	294	11
60	407	14	148	5	1830	55	346	12	222	8	145	5	439	15
75	358	13	125	5	1632	46	284	10	183	7	154	6	370	13
90	258	9	81	3	1143	34	278	10	172	6	71	3	304	11
105	127	4	9	1	498	15	166	6	125	5	67	3	183	7
120	123	4	21	1	497	14	166	6	115	4	69	3	217	8
135	62	3	2	0	226	8	150	6	119	5	124	5	201	8
148	31	1	0	0	24	5	114	5	106	4	88	4	169	7
	(p,g0)		(p,g1)		(p,g2+3)		Ex=7.5		Ex=11		Ex=15		(p,p')	

Proton Energy 49 MeV

Angle	X-Sec [nb/sr]	+/-	X-Sec [nb/sr]	+/-	X-Sec [nb/sr]	+/-	X-Sec [nb/sr]	+/-	X-Sec [nb/sr]	+/-	X-Sec [nb/sr]	+/-	X-Sec [nb/sr]	+/-
30	283	10	88	4	1218	42	295	11	171	7	59	3	176	8
45	380	14	68	3	1477	51	302	11	299	11	175	7	445	18
60	309	16	129	5	1565	54	267	11	291	11	187	8	645	26
90	303	11	76	3	1032	35	267	10	180	7	99	4	365	14
100	137	5	30	1	397	14	148	6	95	4	63	3	355	13
135	51	3	3	0	213	8	128	6	113	5	58	4	331	15
	(p,g0)		(p,g1)		(p,g2+3)		Ex=7.5		Ex=11		Ex=15		(p,p')	

TABLE 4 (continued)

Proton Energy 52 MeV

Angle	X-Sec [nb/sr]	+/-	X-Sec [nb/sr]	+/-	X-Sec [nb/sr]	+/-	X-Sec [nb/sr]	+/-	X-Sec [nb/sr]	+/-	X-Sec [nb/sr]	+/-	X-Sec [nb/sr]	+/-	X-Sec [nb/sr]	+/-
30	257	11	175	7	1018	36	100	5	139	50	100	6	128	6	208	10
45	377	18	129	5	2191	76	401	15	290	11	259	11	262	11	443	17
50	357	15	112	5	2064	71	435	16	290	11	252	10	299	12	558	21
75	277	11	101	5	1551	54	286	11	291	11	346	14	318	13	654	25
90	199	9	34	2	1070	38	272	12	239	10	181	9	90	5	488	20
100	90	5	8	1	391	15	226	10	260	11	224	11	106	6	246	12
136	61	3			213	8	135	6	101	5	129	7	107	5	285	12
148	27	2			138	6	143	6	140	6	131	6	88	5	259	11
	(p,g0)		(p,g1)		(p,g2+3)		Ex=7.5		Ex=11		Ex=15		Ex=20		(p,p')	

Proton Energy 66 MeV

Angle	X-Sec [nb/sr]	+/-	X-Sec [nb/sr]	+/-
42	159	16	640	64
60	165	7	609	22
75	164	7	487	18
90	104	10	251	25
105	87	4	184	8
147	39	20	32	16
	(p,g0)		(p,g2+3)	

distributions to the Legendre polynomial expansion

$$\frac{d\sigma}{d\Omega} = A_0\left(1 + \sum_{i=1}^{4} a_i P_i(\cos\theta)\right) \qquad [4-1]$$

The inclusion of a fifth term was never justified by any marked improvement in the χ^2 value. Since the number of experimental points $(\sigma_1, \sigma_2, \cdots, \sigma_n)$ is normally higher than five, it is possible to select amongst them the five that have the lowest errors and invert the functions

$$\sigma(\cos\theta_1) = F(A0, a_1, a_2, a_3, a_4)$$

$$\sigma(\cos\theta_5) = F(A0, a_1, a_2, a_3, a_4)$$

to extract the values of the Legendre coefficients as

$$A_0 = f(\sigma_1, \sigma_2, \sigma_3, \sigma_4, \sigma_5)$$

$$a_4 = f(\sigma_1, \sigma_2, \sigma_3, \sigma_4, \sigma_5)$$

At this point the code computes the standard deviation for the Legendre coefficient A_0 or a_i $(i = 1, 2, 3, 4)$ from the relation

$$\sigma^2_{a_i} = \sum_i \frac{df}{dx_i}\sigma^2_{x_i} \qquad [4-2]$$

where x_i is any of the $\frac{d\sigma}{d\Omega}$ values considered. Figures 9 to 18 give a complete review of all the angular distributions and their fits. Values normalized to the A_0 coefficients are reported and errors are statistical plus errors induced by the uncertainty in the fitted background slope.

4-6 Discussion

The sparsity of experimental data in our energy region has already been stressed. Comparison with other results is therefore extremely difficult and when performed leads to rather striking results as for example in figure 19, where data from ours and previous experiments [5] [6] [7] [22] show disagreements by even a factor of 4 in the absolute cross section, well outside the experimental errors. Our absolute cross sections are lower than

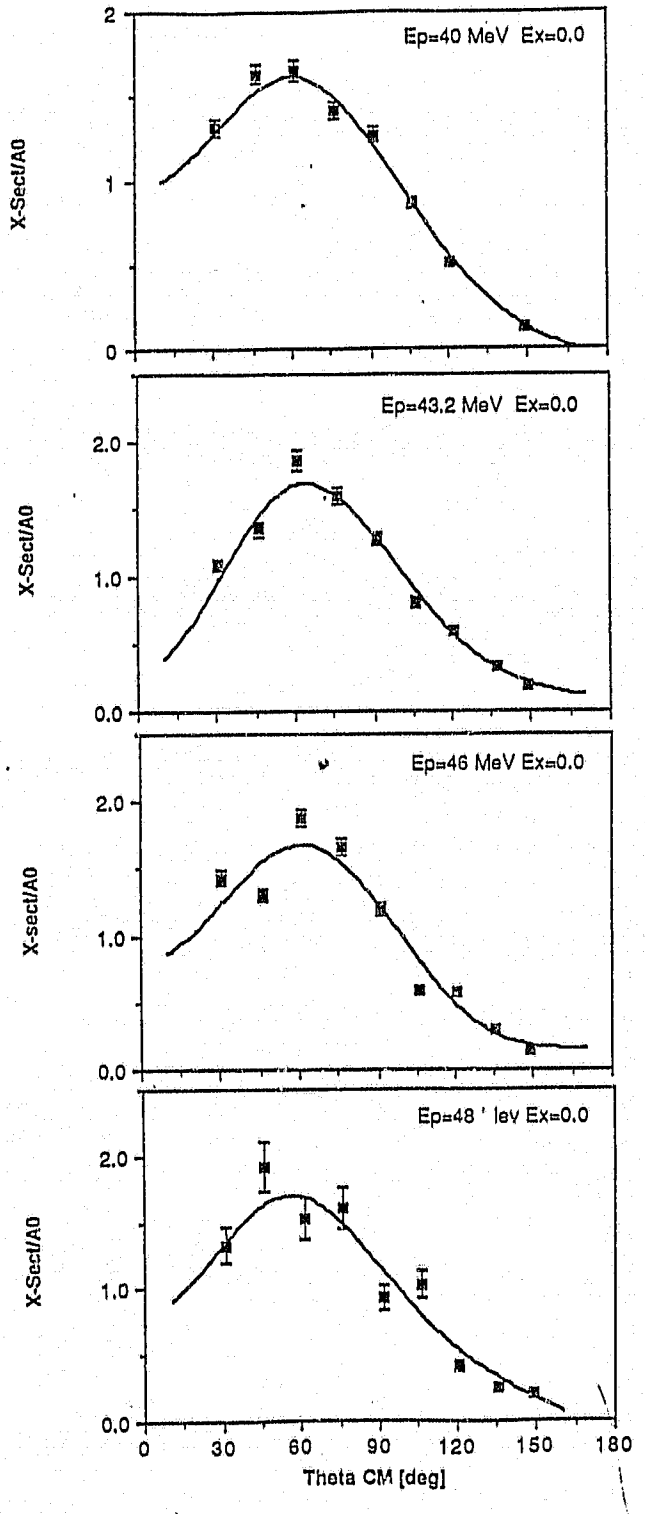

FIGURE 9 Angular distributions for the reaction $^{12}C(p,\gamma_x)^{13}N^*[E_x = 0.0\,\text{MeV}]$ at E_p from 40 to 48 MeV. The full curves are Legendre polynomial fits to the experimental points.